DPhil Thesis

Computational Modelling of Post-stroke Brain Injuries

Xi Chen

St. Hilda's College

Supervisor: Prof. Stephen J. Payne

Cerebral Haemodynamics Group

Department of Engineering Science

University of Oxford

Trinity Term 2024

Computational Modelling of Post-stroke Brain Injuries

Xi Chen

St. Hilda's College, University of Oxford

The healthy functioning of the human brain depends on continuous and sufficient blood flow and metabolism. Severe interruptions in blood and oxygen supply can lead to energy impairment, and result in irreversible brain damage. In ischaemic stroke, a large reduction in blood supply leads to the breakdown of the blood-brain barrier (BBB) and reperfusion injury after reperfusion therapy. The increased BBB permeability disrupts the homeostasis of solutes between blood and interstitial fluid and therefore gives rise to fluid leakage from blood vessels into the interstitial space. As a result, brain injuries such as brain oedema and haemorrhagic transformation can occur.

The simulation of the full brain has previously been performed based on mechanical and poroelastic models to study brain mechanics. In these studies, however, the modelling of post-stroke brain damage has not been considered and it is therefore necessary to propose new models for further investigations. This thesis further develops the simulation tools in the In Silico Clinical Trials for the Treatment of Acute Ischaemic Stroke (INSIST) project.

I first propose a model for the simulation of osmotherapy, which is a common practice to relieve intracranial pressure (ICP) in brain oedema. The model is directly compared with clinical data for model validation. Furthermore, parameter sensitivity analysis is conducted to investigate the impact of various parameters, including shear modulus, tissue hydraulic permeability, and capillary vessel wall permeability, and to determine the effects of these physiological parameters on oedema development. Finally, different administration protocols are studied using the model and a near-optimal strategy for oedema treatment is proposed.

Secondly, haemorrhagic transformation after stroke commonly occurs alongside oedema. Therefore, the model is further developed to include the growth of haematomas by simulating the flow of blood through the interstitial space. The simulation results are compared with clinical imaging to obtain the blood perfusion data and then utilised to investigate the effects of high blood glucose, blood pressure, etc.

Thirdly, a study for the modelling of the contact mechanics of oedema in the brain is conducted. As the brain swells, the cerebrospinal fluid in the ventricle is compressed and drained to release pressure. A complex contact mechanics problem thus emerges which has not been previously solved. This model provides the first computational tool for the simulation of ventricle collapse and large brain deformation. Meanwhile, this study also focuses on the midline shift caused by brain swelling as it is a crucial criterion to determine the severity of oedema. Prediction curves of MLS-ICP relationships are proposed and compared with the clinical data.

Finally, an AI-assisted model for the optimisation of osmotherapy is proposed. The data produced from the in-silico model are utilised to train a deep neural network for the generation of virtual patient groups with different blood-brain barrier damage levels and age. This provides an approach for the optimisation of treatment strategy for patient stratifications.

Contents

Acknowledgements

Completing this DPhil thesis has been a journey filled with challenges, growth, and immense support from numerous individuals and institutions. It is with heartfelt gratitude that I acknowledge their contributions to this work.

First and foremost, I extend my deepest appreciation to my supervisor, Stephen Payne, whose guidance, wisdom, and unwavering support have been instrumental throughout this entire research endeavour. Your invaluable feedback, encouragement, and patience have been indispensable in shaping the direction and quality of this thesis. I am profoundly grateful for the opportunity to learn from your expertise and to benefit from your mentorship.

I am also indebted to the members of my examiners Prof MacMinn and Prof. Watton, for their insightful feedback, constructive criticism, and scholarly guidance at various stages of this project. Your expertise and encouragement have enriched the quality of my research and broadened my intellectual horizons.

I extend my sincere gratitude to the University of Oxford for providing the resources, facilities, and academic environment essential for conducting this research. The stimulating intellectual atmosphere of the Engineering Science Department has fostered my growth as a scholar and provided me with invaluable opportunities for collaboration and exchange of ideas.

I am deeply grateful to the participants of this study, Tamas Józsa, Lei Lu and Jiayu Wang, whose willingness to share their experiences and insights made this research possible. I also extend my gratitude to Yidan Xue, who provided me help and advice on my research and academic career. Your contributions have enriched the depth and relevance of this thesis, and I am profoundly thankful for your time and cooperation.

I owe a debt of gratitude to my colleagues and peers for their camaraderie, encouragement, and intellectual companionship throughout this journey. Your support and friendship have provided solace during challenging times and made the pursuit of this degree a rewarding and fulfilling experience.

To my friends, words cannot express the depth of my gratitude for your encouragement and belief in my abilities. Your patience, understanding, and unwavering support have been a source of strength and inspiration, sustaining me through the highs and lows of this academic pursuit. I appreciate Shiyang Wang, my architect and designer friend, who offered a lot of advice on designing nice figures for my papers.

Lastly, I dedicate this thesis to my family, whose unwavering love, support, and belief in my potential have been the driving force behind my academic endeavours. Your encouragement, sacrifices, and faith in me have been my greatest motivation, and I am forever grateful for your presence in my life.

In conclusion, I express my sincere appreciation to all those who have contributed to this thesis in ways both seen and unseen. Your support, encouragement, and guidance have been invaluable, and I am deeply grateful for the opportunity to undertake this scholarly journey.

Publications

Journal papers:

Chen, X., Józsa, T. I., & Payne, S. J. (2022). Computational modelling of cerebral oedema and osmotherapy following ischaemic stroke. Computers in Biology and Medicine, 151, 106226.

Chen, X., Wang, J., van Kranendonk, K. R., Józsa, T. I., El-Bouri, W. K., Kappelhof, M., van der Sluijs, P. M., Dippel, D. W., Roos, Y. B., Marquering, H. A., Majoie, C. B. & Payne, S. J. (2023). Mathematical modelling of haemorrhagic transformation in the human brain. Applied Mathematical Modelling, 121, 96-110.

Chen, X., Józsa, T. I., Cardim, D., Robba, C., Czosnyka, M., Payne, S. J. (2024). Modelling midline shift and ventricle collapse in cerebral oedema following acute ischaemic stroke. PLOS Computational Biology, 20(5), e1012145.

Chen, X., Lu, L., Józsa, T. I., Clifton, D. A., & Payne, S. J. (2024). AI-assisted In-silico Trial for the Optimization of Osmotherapy following Ischaemic Stroke. (under review)

Conference abstracts as presenter:

Chen, X., Józsa, T. I. and Payne, S. J. 2022. Modelling human cerebral tissue damage caused by acute ischaemic stroke. 9th World Congress of Biomechanics, Taipei. Presentation.

Chen, X., Józsa, T. I. and Payne, S. J. 2023. Modelling Midline Shift and Ventricle Collapse in Cerebral Oedema Following Acute Ischaemic Stroke. European Society of Biomechanics, Maastricht, The Netherlands. Presentation

Chapter 1

Introduction

The human brain, an extremely complex organ comprising hundreds of billions of brain cells, gives us intellectual abilities and other basic body functions such as thermoregulation, emotions, and body movement. Given the importance of the human brain, diseases such as Alzheimer's disease, stroke and brain haemorrhage can lead to high death rates and morbidity rates (Wells, 1978). Specifically, stroke is one of the major clinical concerns. Around 15 million people suffer either an ischaemic or a haemorrhagic stroke around the world every year. Of these, approximately 5 million die and another 5 million are left permanently disabled, placing a heavy burden on their families and society (Boot et al., 2020). In this study, I will focus on one type of stroke, ischaemic stroke, as it is by far the most common, and reperfusion injury after its treatment.

1.1 Ischaemic Stroke

Ischaemic stroke refers to the reduction in blood flow and oxygen supply that is caused by occlusion of brain vessels. Blood occlusions typically appear in the region where the blood vessels are narrowed or blocked over time by fatty deposits known as plaques, which are formed in a process called atherosclerosis. The formation of plaques is partly related to unhealthy habits such as smoking, dietary habits, and alcohol intake (Alamowitch et al., 2001). To control the damage caused by

reduced cerebral blood flow (CBF) to infarct cerebral tissue (tissue with occluded blood perfusion), reperfusion treatments such as thrombolysis and thrombectomy are used to remove the occlusion and hence restore CBF and oxygen supply within a short timescale.

1.2 Post-stroke Injuries

Blood-brain barrier (BBB) is a highly selective and semipermeable system that controls the fluid and substance exchange between brain tissue and brain blood vessels. However, ischaemic stroke leads to blood vessel blockage and reduction in blood and oxygen supply, which gives rise to BBB breakdown. In reperfusion therapy, the occlusion is removed and blood perfusion is restored and this can lead to fluid leakage into the interstitial space through damaged BBB (Fig.1.1). As a result, the accumulation of fluid in the interstitial space gives rise to intracranial pressure (ICP) increase and the water content rise that can lead to tissue swelling and brain oedema.

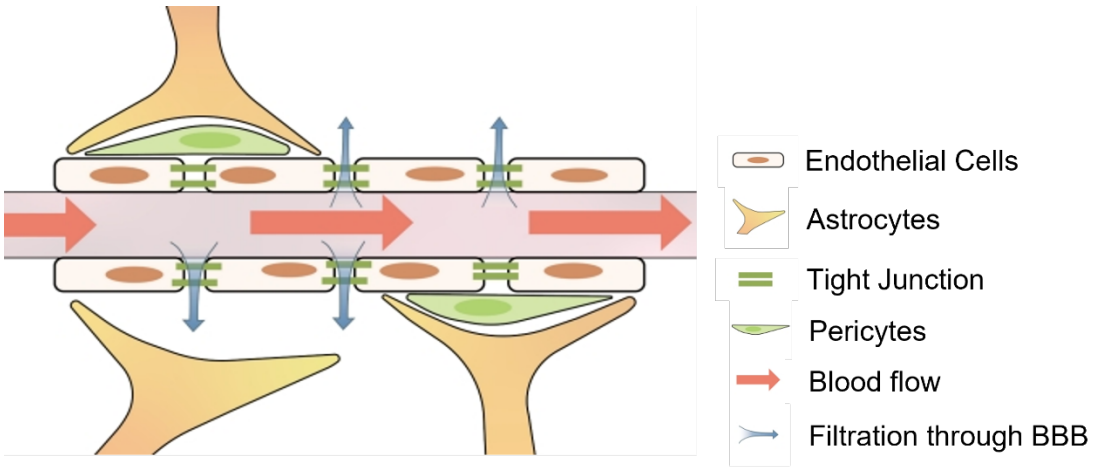

Figure 1.1: Fluid filtration from the lumen to the interstitial space through the blood brain barrier (BBB) of a single capillary vessel (with mean diameter of 5 μm), where the BBB consists of endothelial cells, astrocytes, tight junction, and pericytes. The tight junctions seals the space between endothelial cells.

The tissue swelling can lead to high tissue stress, vessel collapse and secondary ischaemia (Ames et al., 1968) (Fig.1.2). In severe cases, the leakage of fluid in the BBB causes the rupture of the blood vessel and consequently haemorrhagic transformation. These phenomena are collectively termed reperfusion injury (Zimmerman & Granger, 1992). Among ischaemic stroke patients, around 50% of patients have brain oedema and more than 10% develop haemorrhagic transformation (HT). Reperfusion injury following the onset of acute ischemic stroke often occurs without noticeable symptoms (Álvarez-Sabín et al., 2013) but can significantly affect the patient outcome. Therefore, reperfusion injury is a major concern in ischaemic stroke treatment (Mokhtarudin, 2016).

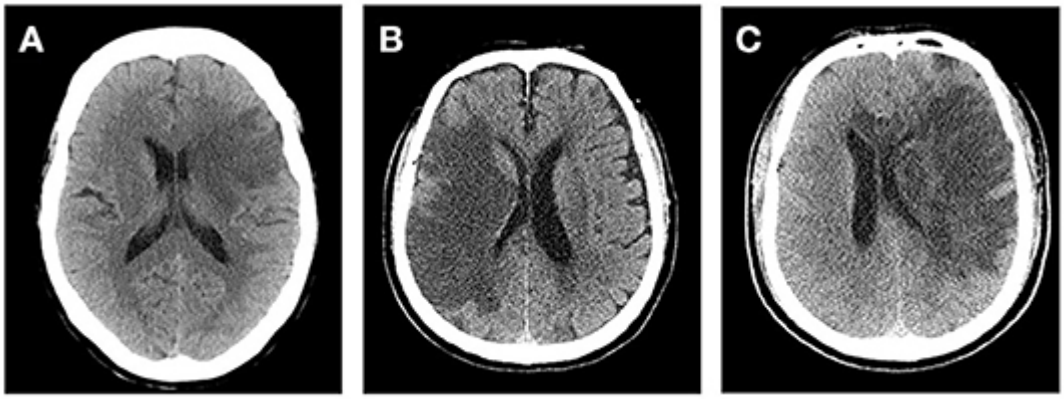

Figure 1.2: Increased ICP and tissue stress in brain oedema, reproduced from Xiao et al., 2022 under CCBY 4.0 license, without change. The shaded region is the oedema and the oedema swells and compresses the surrounding tissue.

1.2.1 Post-stroke Brain Oedema

Brain oedema occurs within a few hours after stroke reperfusion and has been shown to continue worsening up to the first 5 days or even weeks after the stroke onset (Chen-Mei et al., 1959). Therefore, evaluating the severity of brain oedema is of great importance for decision-making for the choice of the type and timing of the treatments. Several early experimental studies showed that

oedema formation depends on the duration (Wu et al., 2018) of ischaemia and also on whether or not the reperfusion therapy is successful (Kimberly et al., 2018). Meanwhile, the severity of oedema is also related to age, blood pressure, medical history, and a number of other patient characteristics. All of these factors, however, can be different between individuals and it is still poorly understood how they affect clinical outcomes (Post et al., 2003). Although these factors (such as the ischaemia duration and age) are observable and straightforward to measure in clinical settings, they are not direct indicators of oedema severity. In clinical trials, ICP rise is the most common indicator of brain oedema severity as it is related to tissue deformation, stress and strain. However, most reliable ICP measurements remain invasive.

Although brain oedema has a mortality rate of around 80%, the treatments of oedema are limited and can induce various side effects. To date, treatments for brain oedema available in clinical settings include osmotherapy and decompressive surgery (DS). In decompressive surgery, part of the skull is removed to allow the swelling brain tissue to expand and therefore it effectively reduces ICP (as shown in Fig.1.3), prevents tissue squeezing and maintains cerebral perfusion pressure (CPP) (Cushing, 1905). Although effective in saving life and reducing mortality rate, DS is related to a number of post-surgical complications such as subdural and subgaleal collections (Amorim et al., 2014; Naugebauer & Jüttler, 2014; Soinne et al., 2014), intraparenchymal haemorrhage (Aarabi et al., 2006; Yang et al., 2008), hydrocephalus, and Syndrome of the Trephined (Fodstad et al., 1984; Joseph et al., 2009; Yamaura et al., 1977).

In decompressive surgery, the most important factors to consider are the size and location of the skull opening. It has been shown in previous studies that patients with a larger size of skull removed are more prone to infection and a larger volume of brain herniation (Simard, 2015), which means a larger volume of tissue protruding through the skull opening (Lambride et al., 2020). Meanwhile,

some studies show that the location of skull removal has different effects on patients and decompressive surgery on the non-injured side compared to the injured side is favourable to relieving tissue stress. However, the results shown in previous studies are sometimes contradictory (Pallesen et al., 2019) and either a guideline or a prediction tool to optimize the size and location of craniectomy is still lacking.

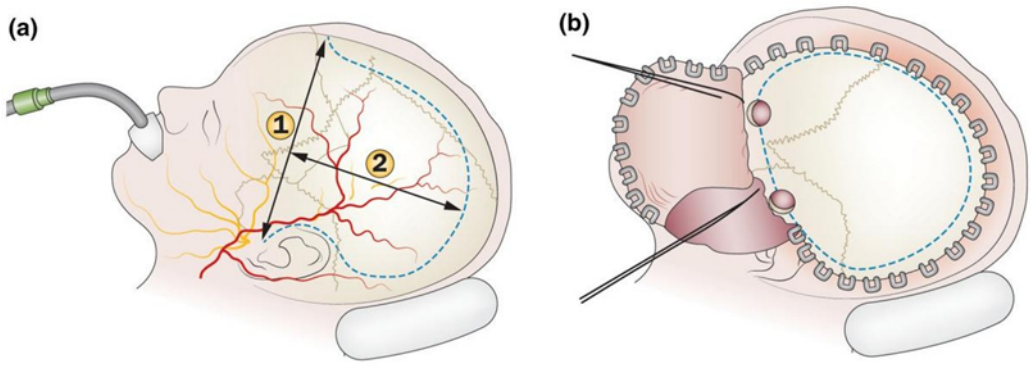

Figure 1.3: Illustration of decompressive craniectomy, reproduced from Fletcher et al. 2016 under CCBY 4.0 license, without change. (a) the choice of the location of decompressive surgery. (b) The opening of the skull to relieve ICP in oedema.

Another treatment, termed osmotherapy, aims to reduce the brain tissue volume by injecting osmotically active substances such as mannitol, glycerol, sorbitol, and hypertonic saline (Nau, 2000). This increases the osmotic pressure in the blood vessels and increases the difference in osmotic pressure between the interstitial fluid and vessel blood (Zornow, 1996). Consequently, this creates a pressure gradient that drives interstitial fluid back into the brain vessels, thereby reducing the volume of the brain tissue herniation and hence controls the ICP rise. The rate of ICP reduction relies on the concentration of the substances used in therapy, the permeability of the damaged blood-brain barrier, the time interval of injection and also the volume of swollen tissue (Steiner & Andrews., 2006). Mannitol is the most commonly used osmotherapeutic agent in controlling elevated ICP after

reperfusion therapy (Adams et al., 1994; Hacke et al., 2000).

Despite osmotherapy having been used widely since the 1960s, the outcome of this therapy is still questioned and there are a number of side effects including renal and pulmonary failure, electrolyte disturbances, and a rebound increase in ICP (Grände & Romner, 2012). For now, osmotherapy has thus not yet been proven clinically because there are insufficient randomized trials to support its usage (Bereczki et al., 2000).

Although many efforts are being made to develop treatments for ischaemic stroke and to prevent the occurrence of oedema, there is still lacking an understanding of the mechanism of the formation of ischaemic stroke, how the infarct develops and how the recovery process happens. In order to study the mechanism, large numbers of experiments involving both animals and humans will likely be required, which are expensive and time-consuming (Araujo et al., 2004). Thus, mathematical models can be very helpful in examining hypotheses of a particular aspect of a biological process in ischaemic stroke. It is proposed here that a mathematical model will be very useful in providing (1) an understanding of the role of biomechanical factors, such as tissue conductivity, in oedema development; (2) a model can be utilised to produce clinical data, such as stress and ICP, and to understand clinical measurement of ICP, stress and MLS; (3) suggestions and optimized strategies for clinical treatments such as osmotherapy and compressive surgery. In this thesis, we will present models for the investigation of oedema treatment, diagnosis and clinical decision-making. Various mechanical factors and how they can affect oedema development will be discussed and optimal treatment strategies will be investigated.

1.2.2 Post-stroke Haemorrhagic Transformation

Haemorrhagic transformation (HT) arises from the disruption of the blood–brain barrier (BBB),

leading to significant damage in brain tissue. In HT, the blood instead of blood components leaks into the interstitial space through damaged BBB and is therefore considered a medical condition severer than oedema. It can occur as a complication of stroke treatment with thrombolytic therapy, particularly when there is a breakdown of the BBB due to the combination of severe ischemic stroke and thrombolytic therapy. The functional outcome for patients with HT varies, with those having large hematomas more likely to experience a poor functional outcome.

The HT can be divided into two types, spontaneous HT and secondary HT. Spontaneous HT is the HT that occurs without thrombolytic treatments and is caused by BBB damage during ischaemic stroke and vessel rupture after reperfusion, whilst the secondary HT occurs after thrombolysis. This classification has thus been helpful for the understanding of the side effects of thrombolysis drug to trigger HT. Both two types of HT are due to the disruption of the blood-brain barrier (BBB) and leakage of blood into brain tissue. The secondary HT is usually caused by the thrombolytic therapy that uses recombinant tissue-plasminogen activator (rt-PA). This drug can change the BBB permeability that causes the leakage of blood flow to the brain tissue. The spontaneous HT occurs in smaller proportion of cases than the secondary HT (Tan et al., 2014).

A pivotal question in this context is whether it is possible to predict HT following an ischemic stroke. Specifically, can we predict the risk of a patients developing HT based on clinical imaging data and other measured imaging parameters. Due to the challenge in studying HT in clinical settings, in-silico models can play a key role in modelling blood flow in HT and improve our understanding of the development of HT. In HT modelling, we aim to establish reliable biophysical models to understand how various mechanical factors can affect the haemorrhage development.

1.3 Outline of the Thesis

This DPhil project aims to provide computational tools for the investigation of post-stroke brain injuries. The models will be validated with clinical data throughout the research to establish reliable computational tools. Once the models are obtained, they can be utilised to sharpen our understanding of oedema and haemorrhagic transformation from biomechanical perspective. Furthermore, treatment strategies can be simulated and optimised for an improved treatment outcome and diagnosis criteria can be better understood to improve the precision of clinical decision-making.

In this thesis, ischaemic stroke and reperfusion injury will be reviewed from both physiological and modelling perspectives in Chapter 2. Applications of previous models will be introduced, and the clinical problems investigated in the models will be summarized. In Chapter 3, (Chen et al., 2022, published work on the Computers in Biology and Medicine), I utilised the mathematical model (Mokhtarudin, 2016) and the perfusion model (Józsa et al., 2021a) from the INISIST project to develop novel models. The model is first utilised to investigate osmotherapy which aims to reduce ICP in brain oedema by injecting hypertonic saline/mannitol. In the study, a mathematical model is utilised to study the effects of various physiological parameters and injection protocol parameters. Near-optimal therapeutic strategies for different cases are suggested. Chapter 4 (Chen et al., 2023, the published work in Applied Mathematical Modelling) develops the model to include haemorrhagic transformation during oedema, as they usually develop spontaneously and can both cause damage to the brain. The growth of the haematoma is simulated and compared with clinical data for model validation and further investigation. Chapter 5 (Chen et al., 2024, published work in PLoS Computational Biology) tackles the deformation issues in brain oedema. In previous Chapters, displacement is not included in the oedema and haemorrhagic transformation models. The deformation is challenging to simulate as large deformation introduces a contact problem. In this

Chapter, the Augmented Lagrangian Method is incorporated into the brain model to solve the contact mechanics and the large deformation in severe brain oedema. The relationship between ICP and midline shift (MLS) is thoroughly discussed. Chapter 6 is publishable work currently under review. In this Chapter, a deep neural network (DNN) is utilised to assist the investigation of osmotherapy in virtual patient groups and to obtain the optimal therapeutic strategy for different patient stratifications. This chapter aims to tackle the problem which I was unable to solve in Chapter 3. As the patients can have various physiological parameters, the optimisation of osmotherapy can be challenging. In this Chapter we investigated the osmotherapy in patient groups of different BBB damage levels and ages. Finally, this DPhil research is summarised, and potential future work is proposed in Chapter 7.

Chapter 2

Literature Review

The human brain is a highly complex organ and is still poorly understood. It receives information from the environment, processes and stores this information, and responds to it. The human brain consumes around 20 % of the total energy supply in the human body while only taking up 2 % of human body weight (Engl & Attwell, 2015). The high energy consumption and the limited energy storage capacity of the human brain make it vulnerable to a reduction in blood or nutrient supply caused by the occlusion of a blood vessel in ischaemic stroke. A reduction in CBF leads to blood-brain barrier breakdown during ischaemia and thus disrupts the homeostasis of fluid between blood and interstitial fluid. As a result, brain oedema and haemorrhage occur and can lead to a high death rate and post-treatment complications after reperfusion therapy. In this chapter, reperfusion injuries will be reviewed from the perspectives of both physiology and computational models.

2.1 Physiology of the Brain-blood Barrier

The neurovascular unit (NVU) is a relatively recent concept in neuroscience that describes the relationship between blood vessels and brain cells such as astrocytes, pericytes, endothelial cells (EC) etc. (Bell et al., 2020) (Fig.2.1). The astrocyte is a star-shaped cell in contact with endothelial cells and neuron cells via astrocyte foot processes. It provides the most complete coverage of blood

vessels such as arterioles and capillaries and is believed to play a key role in the integrity of the blood-brain barrier (Brown et al., 2019; Abbott et al., 2010). Astrocytes not only initiate the formation of the blood-brain barrier but also contribute to homeostatic regulation and provide structural support for the maintenance of the vessel wall (Brown et al., 2019; Bell et al., 2020). Meanwhile, pericytes are embedded in the basement membrane (a thin, extracellular protein matrix), sit along the surfaces of blood vessels and directly contact the underlying endothelial cells. Pericytes can modulate and maintain the BBB by releasing signalling factors to determine the number of EC tight junctions and direct the polarization of the astrocyte end feet (Armulik et al., 2010). A neuron is an electrically excitable cell that communicates with other cells via specialized connections termed synapses (Brown et al., 2019). Lastly, endothelial cells are the major component that forms the blood vessel wall and the passage of substances is tightly controlled at this blood-to-brain interface.

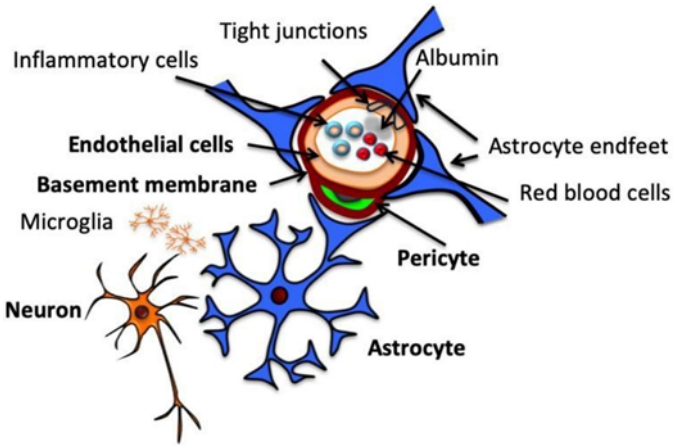

Figure 2.1: The structure of the BBB and the presence of the associated cells, which makes the brain capillary vessels different from the capillaries of other peripheral organs, reproduce from Bell et al., 2020 under CCBY 4.0 license, without change. The figure illustrates a capillary vessel cross section (with mean diameter of 5 μm), where the BBB consists of endothelial cells, astrocytes, tight junction, and pericytes.

In the brain, endothelial cells differ from endothelial cells in other organs by lacking fenestration and by the fact that the walls of the brain microvessels function as a selective permeable barrier. In addition, endothelial cells form complex and continuous junctions termed tight junctions (TJ) which seal off the paracellular space (Stamatovic et al., 2008) and therefore pose a strict control of the movement of metabolites, as shown in Fig.2.2.

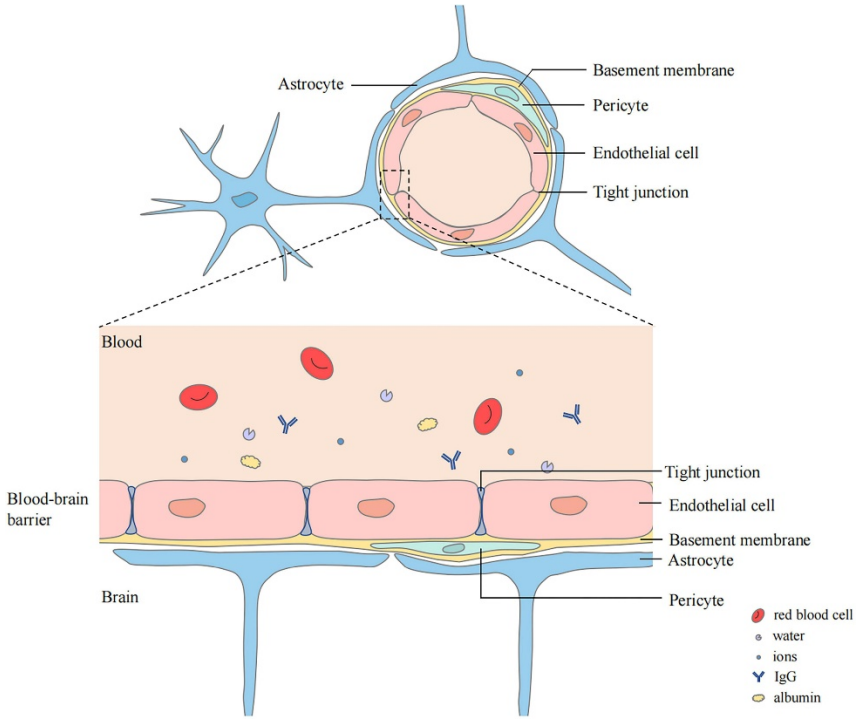

Figure 2.2: The endothelial cells and tight junctions that bridge the cells and form the BBB, reproduced from Gu et al., 2022 under CCBY 4.0 license, without changes.

The BBB is a dynamic system regulated to match its function to the local requirements of the brain tissue. Apart from the brain cells and tight junctions, the structures that also form the BBB are the basal lamina and microglia. The basal lamina is a 30 - 40 nm thick membrane which serves as a macromolecule filter, microvessel support, and cell migration controller (Perlmutter & Chui, 1990). Meanwhile, the microglia near the BBB are involved in the immune response of the brain (Krueger et al., 2010). A study performed by Li et al. (2010) showed that the hydraulic permeability of cerebral capillary vessel wall is very small, around 10^{-11} m/s.cmH_2O, compared with other capillary vessels,

for which it is around 10^{-9} m/s.cmH_2O (Levick et al., 2010). However, various pathological conditions may increase the permeability of the BBB through a number of different mechanisms that remain poorly understood (Greenwood, 1991).

2.2 Blood-Brain Barrier Breakdown

In the human brain, regulation of the cerebral environment and homeostasis between the central nervous system (CNS) and fluids is achieved by three functional barriers, namely the blood-brain barrier, the blood-cerebrospinal fluid barrier, and the arachnoid barrier. Among them, the blood-brain barrier is the main site across which substances exchange. The blood vessel wall selectively filters the fluid flowing through it and allows certain substances into the extracellular space. This barrier ensures that only oxygen, carbon dioxide, glucose and amino acids pass through while it is impermeable to large molecules and toxic substances that can damage the brain. Breakdown of the BBB can be caused by several brain diseases such as stroke, infection, multiple sclerosis, Alzheimer's disease, traumatic brain injury, epilepsy, brain tumours, and other brain injuries. In the case of ischaemic stroke, there is a reduction in cerebral blood flow (CBF) that causes oxygen deprivation to the brain tissue. This triggers a series of molecular reactions that produce toxic proteases and free radicals, which contribute to the damage of the NVU and the opening of the BBB (Nag, 2003). This change in the microenvironment leads to BBB degrading processes including the disruption of tight junctions, alteration of transport proteins and inflammatory process (Yang & Rosenburg, 2011).

The breakdown of the BBB is a complicated process that remains poorly understood (Greenwood, 1991; Hamann et al., 2002). Among the precursors of BBB breakdown, the most significant one is the activation of proteinases such as matrix metalloproteinases (MMPs) (Payne, 2018). MMPs include MMP2 whose activation is triggered by hypoxia-inducible factor-1α (HIF-1α)-dependent

mechanisms while others such as MMP-3 and MMP-9 are activated by cytokines (i.e., TNF-α, IL-1β). In the family of MMPs the best understood ones are MMP-2 and MMP-9, which directly damage the BBB by degrading tight junction constituent proteins (Yang & Rosenburg, 2011). In addition, these two proteinases are also found to play a role in neuroinflammation and neurotoxicity.

2.3 Reperfusion therapy and Occurrence of Oedema

The major aim of reperfusion therapy is to restore CBF to the infarct; available treatments to remove the clot can be either medication or mechanical revascularization. For clots in small vessels, blood thinners such as plasminogen activator (rtPA) are usually used to dissolve the clot (Haley et al., 1993). For clots in large blood vessels, blood thinning agents are less effective, therefore thrombolysis and thrombectomy are more commonly utilized to remove the obstruction (Smith et al., 2005). For example, in the Mechanical Embolus Removal in Cerebral Ischemia (MERCI) treatment, a balloon catheter is inserted into the occluded vessel and the balloon is inflated to prevent blood flow from interrupting the removal process. Then, the retriever is moved through the catheter, wrapped around the clot, and removed together with the catheter (Smith et al., 2008). The process steps are shown in Fig.2.3.

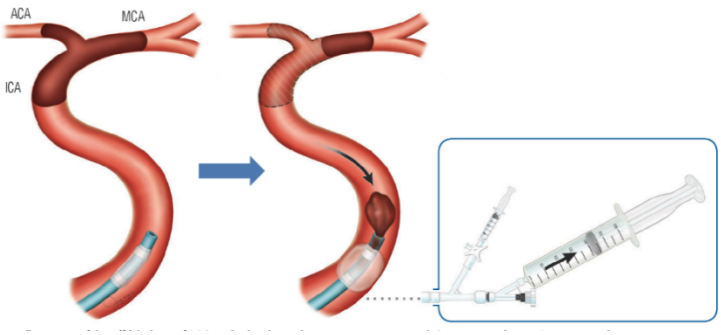

Figure 2.3: Thrombectomy, reproduced from Cheuh et al. 2020 under CCBY 4.0 license, without change. From left to right, a catheter is inserted into the target location; blood clot is captured by the catheter and a balloon is inflated to prevent blood flow from interrupting the process.

As the BBB breaks down, protein plasma filters through the capillary vessel wall into the interstitial space (Kimelberg, 2004; Unterberg et al., 2004). As the blood pressure is higher than interstitial pressure, this creates a pressure gradient that leads to excessive water accumulation in the interstitial space, giving rise to vasogenic oedema. Brain tissue oedema may cause compression of the microvascular bed, which can lead to focal ischemic stroke (del Zoppo et al., 2003), which is also termed secondary stroke. While the oedema grows over time, vasogenic oedema clearance occurs in three possible mechanisms, including: (1) bulk flow driven by pressure gradients from interstitial space to the CSF system (Reulen et al., 1978); (2) oedema fluid protein re-uptake by the astrocytes and breakdown through lysosomal digestion (Fotheringham et al., 2000; Wolman et al., 1981); and (3) reverse vesicular transport of oedematous fluid protein through the endothelium, although this is found only in some cerebral microvasculature (Vorbrodt et al., 1985).

Meanwhile, another type of oedema is known as cytotoxic oedema. Cytotoxic oedema can occur at early stage of oedema development (Liang et al., 2007) and coexist with vasogenic oedema. Instead of being caused by the damage to blood vessels, cytotoxic oedema results from energy failure. This involves the accumulation of water in the astrocyte and neuron cells (Unterberg et al., 2004) but is mostly seen to occur in the astrocytes (Kimelberg, 2004). Three mechanisms are proposed to play a role in the process, which are: (1) increased permeability of neuronal and glial cell towards sodium (Na+) and potassium (K+) ions; (2) failure of ion-pumps after energy depletion during ischaemia; and (3) continuous uptake of osmotically active solutes by neuronal and glial cells (Unterberg et al., 2004). These mechanisms lead to an imbalance in ionic concentrations between the astrocyte and the extracellular space, which results in the disruption of water homeostasis of the astrocyte. Furthermore, the occurrence of astrocyte swelling is usually regarded as an early signal in many cerebral diseases, particularly in ischaemic stroke (Papadopoulos & Verkman, 2007).

2.4 Intracranial Pressure and Monitoring in Brain Oedema

Intracranial pressure (ICP) refers to the pressure exerted by fluids inside the skull on the brain tissue. In a clinical setting, ICP rise leads to increased tissue stress and hence problems such as headache, vomiting and high death rate. The value of normal ICP varies with age (Czosnyka, et al., 2005), CBF (Steiner & Andrews, 2006), body posture, and many other factors. Usually, the ICP value of a healthy adult in a supine posture ranges from 7 to 15 mmHg. In clinical settings, an ICP value between 20mmHg to 30 mmHg indicates mild intracranial hypertension while medical treatments are normally required for patients with ICP values greater than 20 mmHg to 25 mmHg.

Due to the fact that the brain is enclosed in the skull, any increase in the volume of the brain tissue or accumulation of fluid in the skull either leads to a rise in ICP value or is compensated for by a decrease in the volume of another compartment so that the total volume remains constant. The relationship between the volume of cerebrospinal fluid (CSF), the volume of blood and the volume of the brain tissue with ICP can be described by the Monro-Kellie doctrine (Mokri, 2001). This compensatory mechanism can be used to describe how ICP is maintained within the brain. Elevation of ICP can lead to serious damage to the brain by reducing CBF (Aries et al., 2012). ICP and CBF are related by Equation 2.1 below:

$$\mathrm{CPP} = \mathrm{MAP} - \mathrm{ICP} = \mathrm{CBF} \cdot \mathrm{CVR}, \tag{2.1}$$

CPP denotes cerebral perfusion pressure and MAP represents the mean arterial pressure while CPP is the pressure difference that drives perfusion through the brain. CVR, meanwhile, is the cerebrovascular resistance which is highly sensitive to blood gas levels and hence the partial pressure of carbon dioxide in arterial blood (White & Venkatesh, 2008). CVR is also affected by the fraction

of the arterioles remaining open, where it has been shown that cerebral ischaemia may give rise to the occlusion of the vessels, thus increasing the CVR (Siemkowicz, 1980). From Equation 2.1, an increment in ICP will cause a reduction in CBF into the arteries and may also initiate microvessel collapse due to the resulting increase in brain tissue pressure (Steiner & Andrews., 2006). Maintaining BBB function is important to sustain normal ICP and cerebral homeostasis (Unterberg et al., 2004). An increase in BBB permeability may cause brain oedema, which in turn may affect brain tissue pressure and blood pressure change according to the Monro-Kellie doctrine. The healthy BBB is often governed by small pores that only allow small molecules to pass through (Rippe & Haraldsson, 1994), thus increasing its permeability and allowing plasma proteins to pass through will eventually cause brain oedema and lead to an increase in ICP.

Although ICP is of great clinical significance in predicting outcomes and protocols of treatments, the measurement of ICP has been a challenge over the past 60 years. Methods for the measurement of ICP can be either invasive or non-invasive (Schmidt et al., 1999; Rangel-Castillo et al., 2008). The most typical invasive method measures ICP from a ventriculostomy in which pressure is read through a catheter inserted into a lateral ventricle. This method is the gold standard for ICP measurement and has been widely used for comparison and validation of other methods (Robba et al., 2016). Meanwhile, another invasive method, the implantable ICP sensor method, monitors the pressure value in the parenchyma using optical fibres and its validity has been thoroughly documented and presented in previous studies (Raboel et al., 2012).

Although invasive measurements guarantee a more direct and more reliable ICP value, they require the opening of the skull and hence bring a higher risk of bleeding and infection. To find a substitute for invasive methods, efforts have been made to develop non-invasive methods such as transcranial Doppler, which estimates ICP from cerebral blood flow velocity, and the optic nerve sheath diameter

method, which obtains ICP by measuring the diameter of the optic nerve sheath through patients' eye. The traditional and most commonly used methods, however, are image-based methods which utilize various radiological techniques to measure the displacement and deformation of brain tissue, ventricles, and basal cisterns (Fig.2.4). Although potentially useful as a screening tool for very high ICP, brain imaging techniques alone have been proved to be neither statistically significant nor clinically relevant (Miller et al., 2004) thus far. Therefore, it is currently not reliable for clinical management and has been used with multiple other criteria, such as patient age, sex and medical history in clinical settings (Kimberly et al., 2018).

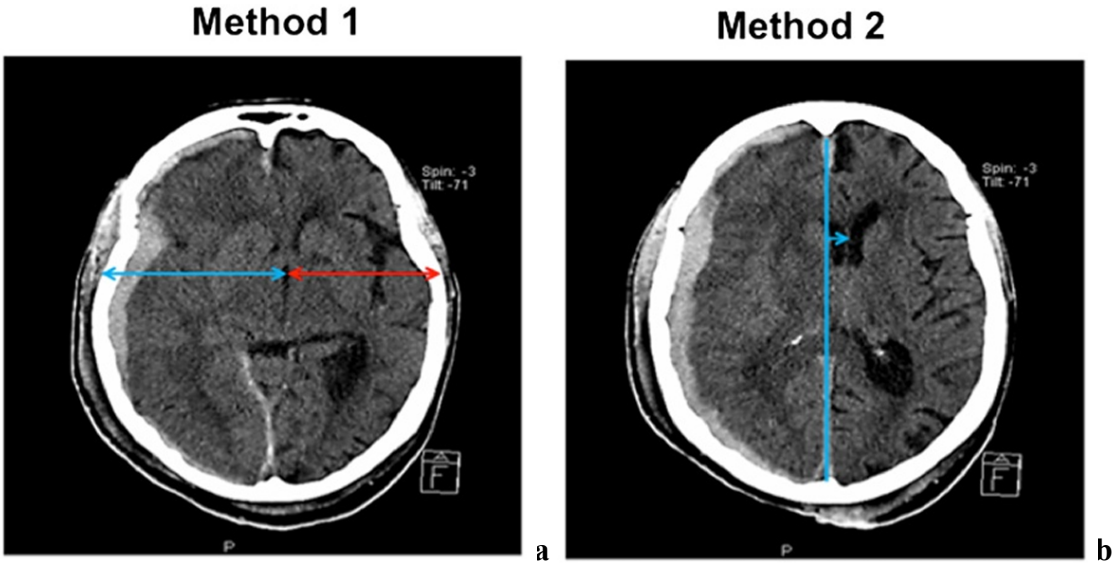

Figure 2.4: Measurement of midline shift (MLS) and radiological imaging-based estimation of ICP, reproduced from Motuel et al. 2014 under CCBY 4.0 license, without change. (a) The midline shift can then be calculated as: (a/2) – b. (b) The ideal midline (IML) is determined as the connection line between the anterior-most point of anterior falx and the posterior-most point of posterior falx. Another parallel line passing through the septum pellucidum is plotted (dotted line), the midline shift can then be measured as the distance between these two lines ("c").

2.5 Reperfusion therapy and Occurrence of Haemorrhagic Transformation

Haemorrhagic transformation (HT) emerges as a complication of ischemic stroke, posing a significant concern for clinical treatment and clinicians. HT is categorized into two types depending on whether thrombolytic therapy is involved, namely the spontaneous and secondary HT. Although the proportion of patients developing this complication is considerable, there is only a limited number of studies focusing on it. Tan et al. (x`2014) reported that the incidence of spontaneous HT was observed in 50 out of 407 patients (12.3%). Lindley et al. mentioned that the overall frequency of spontaneous HT in untreated acute ischemic patients is 8.5% (Lindley et al., 2004). Nevertheless, it remains valuable to understand the physiology and predictors of spontaneous HT to assist clinicians in identifying suitable candidates for thrombolytic therapy. Regarding the secondary haemorrhagic transformation, previous research focus on the physiology, the frequency, the severity, the factor, the predictor, and the treatment of secondary HT after the thrombolytic therapy. The study of the secondary HT is considered as a key for determining the outcome of the thrombolytic therapy (Hornig et al., 1986; Bozzao et al., 1991). Furthermore, the risk of symptomatic secondary HT rises significantly as a result of the side-effects of the therapy (Donnan et al., 1996).

European and North American tissue-plasminogen activator (rt-PA) trials provided the evidence that the rt-PA is the only efficient drug to treat acute ischaemic stroke. Recent studies suggested that the side effects of rt-PA are due to its actions in the neurovascular unit (Wang et al., 2004). rt-PA may enlarge potentially excitotoxic calcium current by interacting with the NMDA-type glutamate receptor. At certain concertations, rt-PA may be vasoactive. By increasing matrix metalloproteinase (MMP) dysregulation after stroke, rt-PA degrades extracellular matrix integrity and increase risks of neurovascular cell dysfunction, blood-brain barrier disruption and oedema. Other studies have hypothesised that the HT is due to the absence of the endothelial basal lamina. HT can also be

classified into HI1, HI2, PH1 and PH2 by the severity of haemorrhage, from microcapillary bleeding to extensive haemorrhage (Fiorelli et al., 1999).

2.6 Cerebral Blood in Haemorrhagic Transformation

The cerebral blood flow (CBF) is a valuable parameter in simulation studies of HT. Accumulating studies have compared quantitatively between non-invasive measurements and minimally invasive measurements for CBF. Flow velocity instruments are applied to determine the flowrate of blood as a type of invasive measurement method. Transcranial doppler ultrasound (TCD) uses ultrasound to calculate the flowrate of blood and is the most common methods to date. Two probes are placed in a vessel and the velocity is determined by the difference between emitted and reflected frequencies (Haywood et al., 1981; Bishop et al., 1986). Regarding imaging methods to measure the cerebral blood flow, positron emission tomography (PET), single-photon emission computed tomography (SPECT), computed tomography (CT) and magnetic resonance imaging (MRI), are commonly used. All imaging measurement theories are based on the movement of a tracer, which is transported around the brain in the vasculature (Payne, 2018).

Meanwhile, the cerebral blood volume (CBV) is also one of the most essential factors that associate with the cerebrum and a key clinical intraoperative monitor during the surgery (Barker, 1998; Haruna et al., 1998). Nowadays, studies show patients with aneurysmal subarachnoid haemorrhage (SAH) are at risk for circulatory volume depletion, which is a risk factor for delayed cerebral ischemia (DCI). Correspondingly, Hoff et al. (2008) suggested the fluid management guided by daily measurements of blood volume could reduce the risk of severe hypovolemia (Hoff et al., 2008). Imaging instruments are utilised to measure cerebral blood volume. PET and MRI(DSC) are commonly used nowadays. The advantage of these imaging instruments is having the ability to detect cerebral blood volume and cerebral blood flow simultaneously (Martin et al., 1987). As I discussed the theory of these imaging techniques, by applying the tracers in the vasculature, both CBV and

CBF can be detected and calculated. All these methods rely on using a model of CBF and CBV to fit the experimental data. Recent studies suggested a non-invasive method, called pulse oximetry to measure the blood volume by monitoring arterial blood oxygen saturation (Severinghaus & Honda, 1987; Haruna et al., 1998). Furthermore, another advanced method modified by pulse oximetry, named pulse spectrophotometry or pulse dye densitometry (PDD), can allow clinicians to measure the ratio of the arterial haemoglobin concentrations to ICG continuously (Iijima et al., 1997; Hoff et al., 2008).

2.7 Mathematical and FEM Models for Brain

Mathematical and Finite Element Method (FEM) models have been utilised to investigate biological and biomechanical problems for decades (Nagashima et al., 1990; Tada et al., 1994; Guo et al., 2020). In this section, brain oedema models are categorized based on the theories used in the modelling, namely poroelastic theory and solid mechanical theory. Poroelastic theory is a mathematical theory that is widely used in the fields of geomechanics, hydrology and biomechanics to describe the interaction between fluid flow and tissue deformation. Meanwhile, the solid mechanical models simulate the brain using solid mechanics theories where each part of the brain such as the skull, subarachnoid space and ventricles are described by certain constitutive relationships and mechanical parameters.

2.7.1 Solid Mechanical Models for Cerebral Oedema

In radiological imaging-based estimation of stress, the most important factor is the midline shift (MLS), which represents the shift of brain past its centre line. Compared to stress, MLS is relatively straightforward to obtain on images such as CT and MRI and can be used to estimate stress. To study the relationships between MLS and tissue stress, in-silico modelling has been used to study MLS

and stress distributions in various brain diseases such as traumatic brain injury and stroke.

In the paper by Bing et al. (2020), the full brain is modelled to analyse the correlation between stress and MLS. Two biologically informed finite element head models, human and rat, were constructed. In the model, components such as grey matter, white matter, cerebrospinal fluid, skull and falx were constructed as subdomains with different mechanical properties for both human and rat models, with oedema modelled as growing volumes over time. MLS data from the rat head model were first validated against clinical data from a rat brain and to justify the material properties used in the model. Stroke and oedema were then simulated at three locations in the human brain: basal ganglia, fronto-opercular/anterior insula and temporo-parietal. It is shown that with the same growth rate of oedema, the MLS value is significantly affected by the location of oedema at a given time (Fig.2.5).

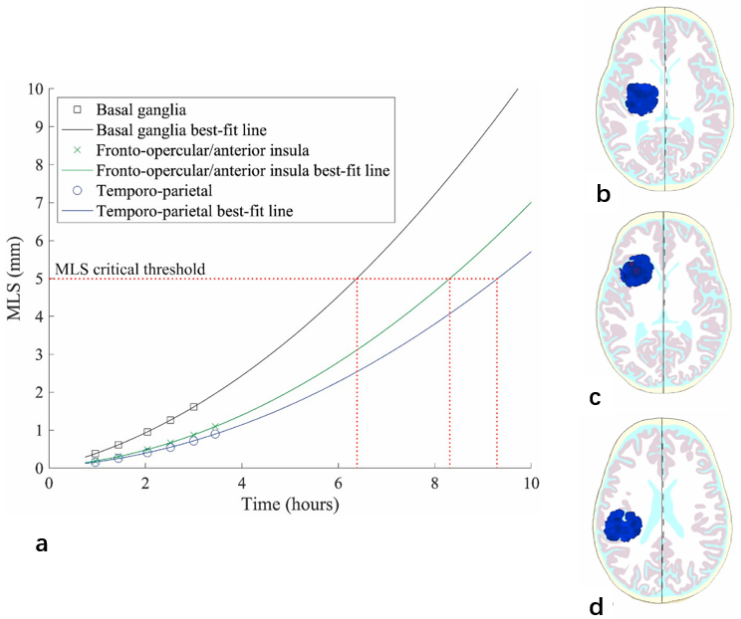

Figure 2.5: (a) The three locations are simulated to obtain the MLS-time curve for the prediction of intracranial stress, adjusted from Bing et al. 2020. (b) basal ganglia. (c) anterior insula. (d) temporal parietal. The basal ganglia shows the largest MLS, reproduced without change from Bing et al. (2020) under CCBY 4.0 license.

Similarly, Fletcher et al. (2016) constructed an Ogden hyper-elastic Finite Element model to study decompressive surgery related issues. In this model, the potential damage of brain tissue is estimated by critical stress, values over which might lead to high axonal stretch. Results from the idealized model showed how the potentially damaged volume of brain tissue increased with an increasing volume of brain tissue herniating from the skull cavity and with a reduction in the craniectomy area. The damaged tissue volume can be limited to zero if the craniectomy size is chosen properly (Fig.2.6). In addition, the craniectomy edge, either a fillet or a chamfer on the bone margin, only has a slight effect on the tissue strain.

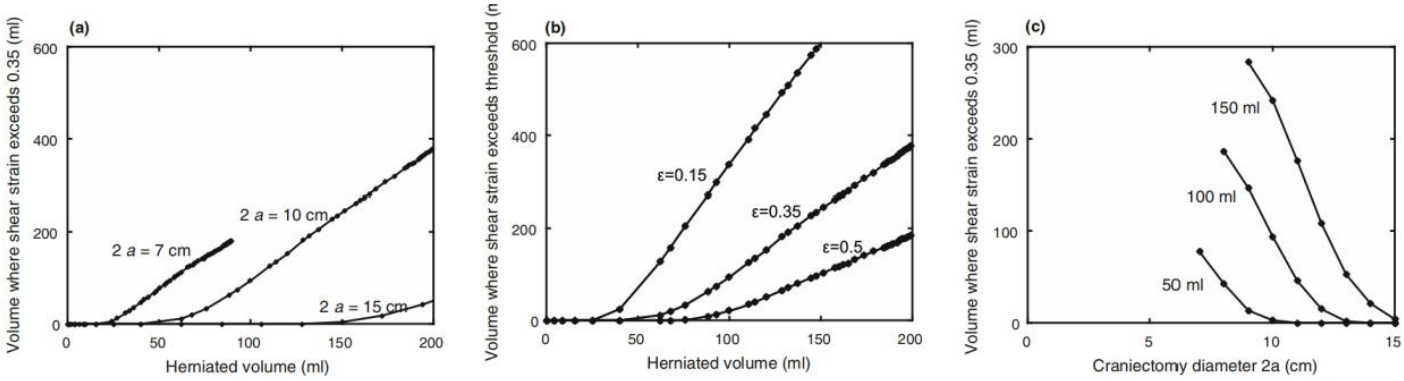

Figure 2.6: Simulation results showing that when craniectomy diameter is sufficiently large, the volume of tissue in risk of shear damage reduces to zero, reproduced under CCBY4.0 license from Fletcher et al. 2016, without change. (a) The relationship between herniated volume and high shear strain volume under different craniectomy diameters. (b) The relationship between herniated volume and volume experiencing shear strain over thresholds when craniectomy diameter is 10 cm. (c) the volume with higher strain than 0.35 with various craniectomy diameters.

Meanwhile, solid mechanical models have been widely applied to study decompressive surgery since in-silico models provide a prediction of stress in the brain tissue after surgery and can be used as

guidance for the optimization of the craniectomy strategy. In 2017, a personalized model for craniectomy was developed by Weickenmeier et al. to predict post-surgical strain field. The models were obtained from MRI imaging and three mechanisms that potentially lead to the post-operation complications were proposed, which are: axonal stretch in the centre of the bulge; axonal compression at the edge of the craniectomy; and axonal shear around the opening. Results from simulations suggest that collateral craniectomy with the skull opening at the side of swelling is preferable over contralateral craniectomy with the skull opening at the opposite side since it induces less deformation, less rotation, smaller strains, and a markedly smaller MLS.

In these models, useful information on brain tissue swelling can provide a guideline for decompressive surgeries to effectively reduce tissue stress. However, solid mechanical models do not simulate pressure fields and are limited by the fact that they cannot provide pressure distribution within the brain tissue. In addition, the swollen volume of oedema is usually given as an input in these models. As a result, these models are not able to present the interaction between brain tissue and fluid compartments such as blood and interstitial fluid, which play an important role in the development of oedema. Furthermore, the constitutive law of the brain tissue can be complex. According to the review by Budday et al. (2020), the mechanical behaviours of the brain tissue can be only described by certain constitutive laws, such as neo-Hookean, Mooney-Rivlin and Ogden under different types of loads (compression, tension and simple shear). Therefore, the mechanical properties used in these models can be inaccurate in terms of representing brain tissue deformation, stress and strain.

2.7.2 Poroelastic Models for Cerebral Oedema

Poroelastic theory models the brain as a porous, deformable and permeable medium (Biot, 1956; Biot, 1962a; Biot, 1962b). In 2011, Tully & Ventikos, for the first time, used a multi-compartment

poroelastic model to study fluid transfer between different fluid compartments (capillary blood, interstitial fluid and cerebrospinal fluid, arteriolar blood, venular blood and brain tissue) during hydrocephalus, as shown in Fig.2.7. In this model, each fluid compartment is modelled using poroelastic theory and the various flow parameters are used for the compartments. Using this model, Tully & Ventikos (2011) tested parameter sensitivity to obtain estimates of parameter values under healthy state and explored normal pressure hydrocephalus (NPH), a form of chronic hydrocephalus whose pathophysiology remains unknown.

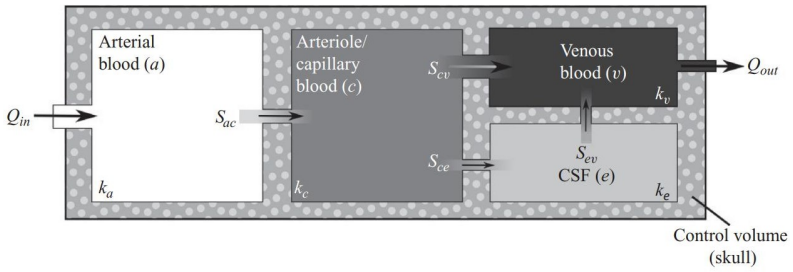

Figure 2.7: A schematic of the multicompartment model formulation for the brain. The model is 0D and the brain consists of arterial, arteriole/capillary, venous and CSF fluid compartments. The arrows show the direction of flow and fluid exchange between these brain compartments, reproduced from Tully & Ventikos 2011 with permission, without change.

The model was then further developed for various applications. Patient specific data such as arterial blood flow, tissue hydraulic permeability and patient-specific brain geometry obtained using diffusion weighted imaging (DWI) have been employed to study CSF clearance in a smoker and a non-smoker's brain (Fig.2.8). However, due to the lack of patient specific data, the reliability of results is limited by the fact that there are only two patients included in this study (Guo et al., 2020).

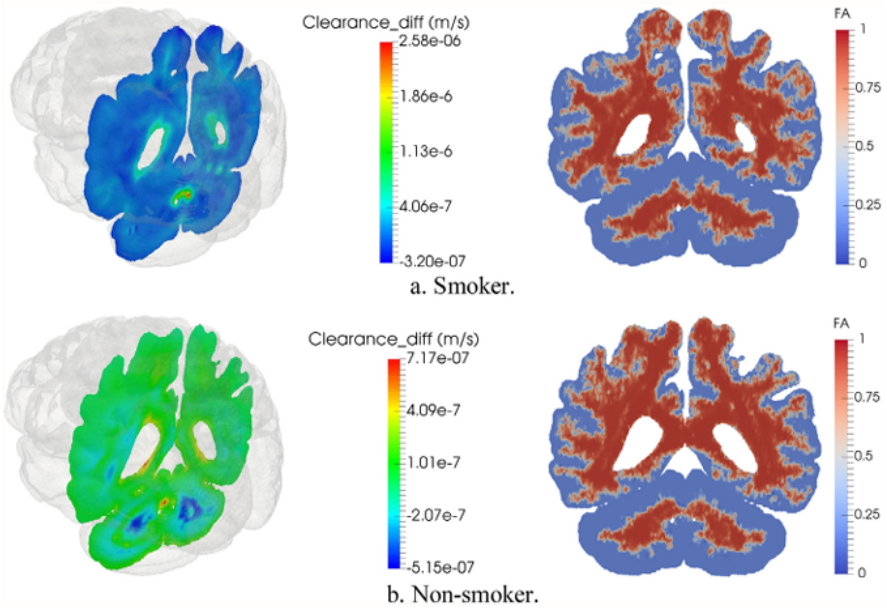

Figure 2.8: The left column presents clearance rate of interstitial fluid of smoker and non-smoker. The right column shows the fractional anisotropy in hydraulic conductivity of brain tissue measured with DWI, reproduced from Guo et al. 2020 under CC BY license, without change. The model is an 3D model that extends the work of Tully & Ventikos (2011)

In addition, the same group studied brain oedema and hydrocephalus using the same model (Vardakis et al., 2016). However, partly due to the difficulty of validation, most of these results presented in these studies are not validated and thus these results only provide a qualitative comparison between patients with brain disease and the control group. In this paper the model was validated with CBF imaging data, the results show a strong heterogeneity and the CBF shown in the simulation result was found to be several times smaller than the real value. This is partly because the brain tissue and the blood vessel distribution are assumed to be homogeneous and the imaging technique cannot distinguish CBF between the arterioles and arteries (Guo et al., 2019).

Meanwhile, Li et al. studied brain mechanical behaviour based in a single compartment poroelastic model which only takes interstitial fluid and brain tissue into consideration. In 2011, this model was

utilized to study the effect of head position on brain oedema in traumatic brain injury (TBI). The results show that gravitational forces have a significant impact on the pressure of the oedema zone in the brain tissue and ICP in the oedema region decreased by 15% in the prone position compared to the supine position.

A significant problem in poroelastic modelling is the number of parameters used in the model. While some of them can be measured or tested directly in experiments, many of them are not available on a patient-specific basis. In 2013, Li et al. compared their simulation results with constant-rate infusion data experimental results from Mann et al. (1978) who performed short-duration infusions of artificial CSF into the SAS for both animals and a human subject. Parameter values of tissue shear modulus, Poisson ratio, Biot's number and Skempton number were varied and optimized using an artificial neuron network (ANN) technique.

A poroelastic brain model has also been applied for the simulation of decompressive surgery. Although decompressive surgery has been recommended as a life-saving practice for the management of swollen brain and intracranial hypertension, the effect of size and location of craniectomy remain controversial and there is no guideline yet available. In a study conducted by Lambride et al. (2020), a biphasic, nonlinear poroelastic model was employed to study tissue swelling with a specific craniectomy size and location (unilateral, bifrontal and bifrontal with midline bar). Furthermore, prediction curves of herniation volume through the skull opening as a function of ICP were presented, which are relevant to craniectomy strategy and useful to reduce herniation volume and to prevent unnecessary risk of infection. While this study focuses on the volume of swollen tissue, another study done by Holst & Li. (2014) investigated the fluid accumulation in craniectomy and indicates that there is an increase in water content and tissue strain after surgery. Their results show that there is a strong correlation between the craniectomy strategy

and post-surgical strain and stress and clinical outcome.

2.7.3 Mathematical Models for Haemorrhagic Transformation

Wang and Payne (2021) first presented a mathematical model to describe the dynamics of haemorrhagic transformation (HT) within a 1D vasculature model. The model operated under the assumption of uniform geometries for vessels within the same generation. The study found that the haematoma radius can depend on the vessel radius and proposed that the capillary compression can have significant impact on blood leakage in venules. However, anatomical studies suggest that capillaries possess a more web-like structure rather than a tree-like one (Duvernoy et al., 1981). Importantly, the initial model did not consider the effects of HT on the neighbouring normal vessels and tissue.

In an extension of their work, Wang et al. (2022a) increased the scale of the vasculature model to better correspond with the human vasculature and incorporated the penetrating model developed by El-Bouri and Payne (2018). This enhanced model investigated the repercussions of haemorrhagic transformation (HT) on the surrounding tissue and vessels (Fig.2.9). The results indicated a decrease in perfusion by approximately 13-17% and a reduction in cerebral blood volume (CBV) by around 20-25% following the onset of HT. These effects were attributed to capillary compression caused by increased interstitial pressure. However, it is crucial to highlight that this model primarily focuses on a length scale of around 1 mm, making it challenging to directly compare the simulation results with imaging data.

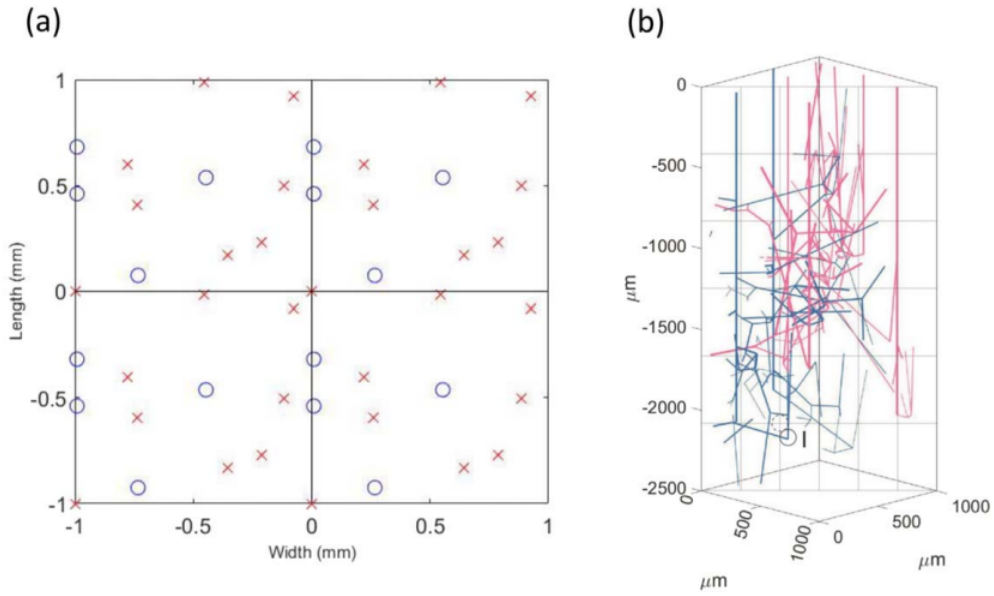

Figure 2.9: Cross-section of brain at different positions and the effects on ICP, reproduced from Wang & Payne et al. (2021) under CC BY 4.0 license, without change.

2.8 In Silico Clinical Trials for the Treatment of Acute Ischaemic Stroke (INSIST) Project

Brain oedema and blood perfusion models are developed in the INSIST project and this thesis will base on these previous models to investigate brain injuries. In the work by Mokhtarudin & Payne (2015), a 0-dimension mathematical model for the brain oedema is developed for the investigation of how mechanical factors can affect the oedema growth. The detail of the work is introduced in Appendix A and have been used and modified for the modelling of brain oedema and haemorrhagic transformation throughout this thesis.

Furthermore, a perfusion model has been provided by Józsa et al. (2021a), the model considers the brain as multi-continuum medium with three compartments (arteriole, capillary and venule) governed by 3 fluid transfer equations for the simulation of blood perfusion. In the model, the brain pial surface is subdivided into perfusion regions for the simulation of occlusion in different blood vessels. The model constitutes the technical basis of this thesis as blood perfusion can be used to generate brain stroke and brain damage area in stroke. Thus, it provides the geometry of oedema and

haemorrhage in the models presented in the thesis. The governing equations of perfusion model is introduced in the perfusion model section in Chapter 3 and details of the model are thus neglected here.

2.9 Conclusion

In this chapter, a brief overview of the physiology and models of the brain has been provided. There are three approaches used in modelling the human brain, namely mechanical modelling and poroelastic modelling for oedema and mathematical modelling of haemorrhagic transformation. While the mechanical modelling provides the distribution of tissue stress and strain, it is not able to present the interaction between fluid and solid tissue. Meanwhile, poroelastic models can describe such interactions and show the distribution of ICP, which is an important factor to consider in clinical settings. However, many parameters are involved in these modelling approaches. Therefore, the accuracy of simulation results is affected by the choice of parameter values used in the model and the results are likely to be highly sensitive to the variation of these parameters between individuals.

Chapter 3

Cerebral Oedema and Osmotherapy*

In this Chapter, we first simulate the brain oedema based on our previous work from INSIST project (Mokhtarudin & Payne, 2017; Józsa et al., 2021a). A simplified oedema model without the deformation is considered here to focus on only the ICP evolution during osmotherapy episodes. This helps establish an oedema model for the investigation of osmotherapy, which has been widely used but controversial therapy. Here, the impact of different physiological parameters and administration protocols are investigated. This Chapter also constitutes the technical basis for further development of haemorrhagic model and oedema model with deformation.

3.1 Introduction to osmotherapy

The healthy functioning of the human brain depends on a continuous and sufficient blood flow to cerebral blood flow (CBF) can lead to blood brain barrier (BBB) breakdown and hence increase the

* The contents of this chapter are reproduced without change from (Chen et al., 2022). The work is based on the perfusion model (Józsa et al., 2021a) and mathematical oedema model (Mokhtarudin & Payne, 2015) from INSIST repository. Technical work on FEniCS code is implemented to combine the two models and improve model coupling and performance. The mathematical model for oedema (Mokhtarudin & Payne, 2015) is modified to create a model with four compartments and to include osmotic pressure for osmotherapy investigations. The mathematical oedema model code was implemented in a different software by Mokhtarudin and is reimplemented in FEniCS by Chen, whereas the perfusion model code was implemented in FEniCS by Józsa et al. (2021a) but renewed for a better model performance by Chen in this Chapter.

permeability of the BBB (Yang & Rosenberg., 2011; Lee et al., 2017). When reperfusion therapy is utilised to restore CBF to the infarct region, the increase in blood pressure can then lead to excessive fluid leakage into the interstitial space (Fig.3.1). As a result, the accumulation of fluid in the interstitial space can give rise to brain oedema and increase intracranial pressure (ICP) and brain tissue stress (Donkin et al., 2010). Elevated ICP can cause symptoms such as headache, nausea, vomiting, and loss of consciousness. Usually, a value of ICP over 25 mmHg (Leinonen et al., 2018) is considered life-threatening, requiring immediate treatment. Thus, ICP is a crucial factor in clinical decision-making and therapeutic strategies. To restore a normal ICP value in the range 5 to 15 mmHg (Leinonen et al., 2018), a number of strategies such as osmotherapy, ventilation, and decompressive surgery can be used (Ayata & Ropper, 2004).

Osmotherapy has been widely used since 1962 when it was first reported to be effective in controlling ICP (Wise & Chater, 1962). To date, four types of osmotic agents have become available for the treatment (mannitol, hypertonic saline, sorbitol, and glycerol). Hypertonic saline has become increasingly popular (Larive et al., 2004; Hays et al., 2011) and therefore the present study focuses on this agent. Hypertonic saline restores ICP by osmotic mobilisation of water from the brain to the intravascular space and therefore reduces the volume of the accumulated interstitial fluid. In addition, due to the mobilisation of interstitial fluid, the rheological characteristics of blood are changed, and this thus facilitates the recovery of cerebral perfusion pressure (CPP) and mean arterial pressure (MAP).

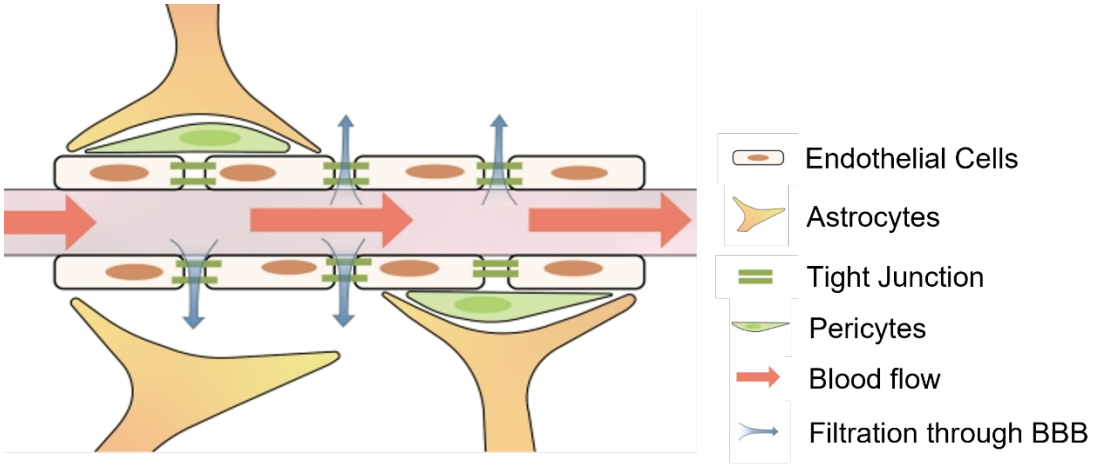

Figure 3.1: Fluid filtration from the lumen to the interstitial space through the blood brain barrier (BBB) of a single capillary vessel.

Despite its various benefits, the side effects of hypertonic saline can lead to a range of problems (Grände & Romner, 2012). One problem is that the increase in Cl^- induces hyperchloraemic acidosis (Kølsen-Petersen et al., 2005). A high concentration of NaCl (over 160 mmol/L) is also reported to worsen outcome and to damage the BBB further (Himmelseher, 2007; Qureshi & Suarez, 2000). Therefore, it is important to choose the concentration and administration protocol properly. In clinical settings, two types of hypertonic saline injection commonly suggested are a bolus injection of 3%-5.6% NaCl over 10-20 minutes and a continuous injection at a concentration of 1.6%-7.5%. During the injection, electrolytes are monitored, and plasma sodium is proposed to be maintained in the range of 145-155 mmol/L (Kølsen-Petersen, 2020). However, even though comparisons of osmotherapy outcomes have been conducted previously (Tyagi et al., 2007; Carney et al., 2017; Mangat, 2018; Gu et al., 2019), there is yet no optimised concentration or administration protocol for hypertonic saline infusion.

To address this problem, the present study sets out to extend stimulation tools developed in the In Silico Clinical Trials for the Treatment of Acute Ischaemic Stroke (INSIST) project (Konduri et al.,

2020; Miller et al., 2021) and thus capture osmotherapy and explore near-optimal treatment protocols. The proposed model bridges the gap between the measured ICP values and unknown physiological parameters, such as blood pressure, capillary wall permeability, etc. Once a reliable model is established, it will help to sharpen the focus of resource-intensive clinical studies, and thus lower the associated (often very high) costs. Inspired by recent studies on biofluid transport in the brain (Li et al, 2009; Sweetman et al., 2011; Tully et al., 2011; Yuan et al., 2013; Mokhtarudin & Payne, 2015; Guo et al., 2018; Vardakis et al., 2019; Józsa et al., 2021a; Miller et al., 2021; Józsa et al., 2022), a multi-compartment porous Finite Element model will be utilised to investigate the impact of osmotherapy on ICP.

In this model, we will present the evolution of ICP during osmotherapy episodes. The study consists of the following parts: (1) the governing equations will be presented and parameter sensitivity analysis will be conducted to identify the crucial parameters; (2) results of the Finite Element model will be compared with clinical data from 8 patients who underwent 22 episodes of osmotherapy; (3) the effects of protocol parameters including doses, infusion time and retention time will be investigated; (4) two possible cases of treatment failure will be presented and the corresponding strategies will be suggested. The model proposed here can be further developed in the future to provide a test bed for alternative strategies.

3.2 Methods

The brain is assumed to consist of four compartments, i.e., tissue, arteriole, capillary, and venule network and can thus be considered as a multi-continuum system. The modelling pipeline consists of three 3D models for the simulation of blood perfusion, oedema, and osmotherapy, respectively. The models are presented individually before being coupled together.

3.2.1 Perfusion Model*

3.2.1.1 Governing Equations

In the perfusion component, the brain is assumed to be a steady-state three-compartment porous medium including arteriole, venule, and capillary blood compartments (Józsa et al., 2021a). The governing equations describing three porous compartments are taken directly from this previous study to simulate blood flow in the 3D brain mesh:

$$\nabla \cdot (\boldsymbol{K}_a \nabla p_a) = -\omega_{ac} \cdot (p_a - p_c), \tag{3.1}$$

$$\nabla \cdot (\boldsymbol{K_c} \nabla p_c) = \omega_{ac} \cdot (p_a - p_c) - \omega_{cv} \cdot (p_c - p_v), \tag{3.2}$$

$$\nabla \cdot (\boldsymbol{K}_v \nabla p_v) = \omega_{cv} \cdot (p_c - p_v), \tag{3.3}$$

where p_a, p_c and p_v are the Darcy pressures in the arteriole, capillary, and venule compartments respectively. $\boldsymbol{K_i}$ is the permeability tensor of compartment i, whereas ω_{ij} represents the fluid transfer coefficient between compartments i and j. Note that the transfer coefficients are different in grey matter and white matter and can thus be further defined by ω_{ac}^{w}, ω_{ac}^{g} and ω_{cv}^{w}, ω_{cv}^{g}, respectively. In the equations, the LHS terms represent the blood flow within each compartment and the RHS terms describe the blood flow between compartments.

According to previous studies (El-Bouri & Payne, 2016; Józsa et al., 2021a), the arterioles and venules are assumed to comprise penetrating vessels perpendicular to the pial surface, and arteriole and venule compartments are therefore modelled as anisotropic and inhomogeneous porous media. Meanwhile, the capillary vessels form an interconnected network, and this compartment is thus considered a porous medium with isotropic and homogeneous permeability (El-Bouri & Payne, 2015). Therefore, the $\boldsymbol{K_c}$ tensor field is replaced with the K_c scalar field.

* Perfusion model is the contribution of Jozsa et al. (2021a), and the model is reimplemented by Chen for better performance in this Chapter.

3.2.1.2 Boundary Conditions

Blood feeds the brain through penetrating arterioles and flows back into the veins through penetrating venules at the pial surface. Therefore, blood flow through pial surface and ventricle surface in the capillary compartment is set to be zero. Meanwhile, the flow through the ventricle surface is zero for arteriole and venule compartments. According to a vascular territory atlas (Tatu et al., 1998), each artery feeds one sub-territory at the pial surface, as shown in Fig.3.2. In this model, the blood pressure in the venular compartment on the cortical surface is assumed to be 15 mmHg, while the pressure in the arterioles at the pial surface is around 90mmHg (Stromberg & Fox, 1972; Tamaki & Heistad,1986; El-Bouri & Payne, 2018). To account for artery occlusion scenarios, blood flow through the perfusion territory of an occluded vessel is set to zero whereas pressure on the pial surface is assumed to remain constant in other regions. Boundary conditions of the perfusion model are summarised in Table3.1.

	Cortical Surface	**Ventricle Surface**
Arteriole Blood	$p_a = 90$ mmHg (non-occluded regions); $\boldsymbol{K}_a \nabla p_a = 0$ (occluded regions);	$\boldsymbol{K}_a \nabla p_a = 0$
Capillary Blood	$K_c \nabla p_c = 0$	$K_c \nabla p_c = 0$
Venule Blood	$p_v = 15$ mmHg	$\boldsymbol{K}_v \nabla p_v = 0$

Table 3.1: Boundary conditions for the perfusion model

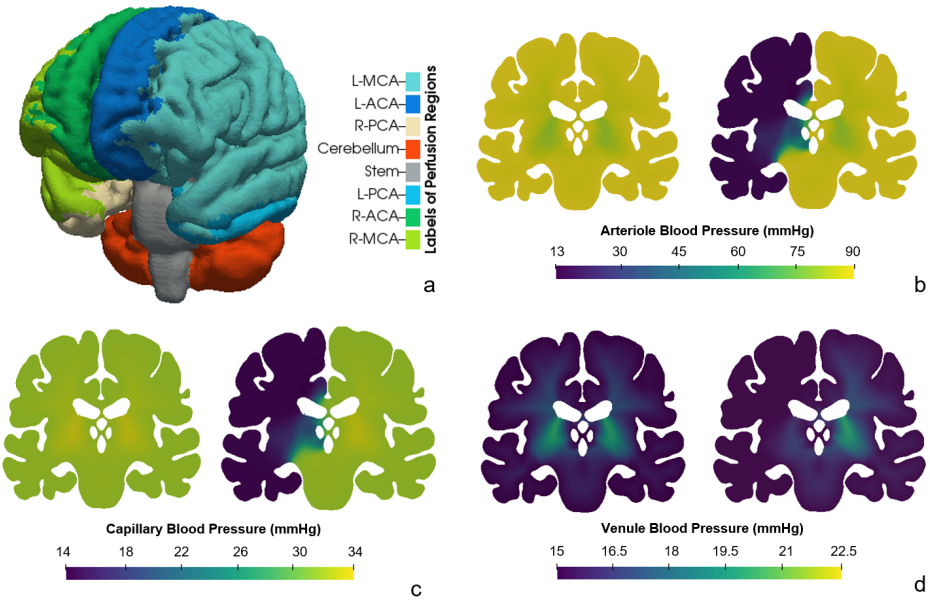

Figure 3.2: Superficial perfusion territories corresponding to large arteries, where L-PCA, L-MCA, L-ACA and R-PCA, R-MCA, R-ACA represent the posterior, middle and anterior cerebral arteries on the left and right hemisphere, respectively (a); arteriole blood pressure distribution along the coronal plane and the pressure drop due to occlusion in left hemisphere (b); capillary blood pressure distribution along the coronal plane and the pressure drop due to the occlusion (c); venule blood pressure distribution along the coronal plane and the pressure drop due to the occlusion (d).

3.2.2 Oedema and Osmotherapy Model

3.2.2.1 Governing Equations

The brain is modelled as a three-compartment porous medium in the perfusion model since the flow exchange between the capillary network and the interstitial space is negligible in a heathy brain. In contrast, an additional compartment for interstitial fluid is required for the oedema and osmotherapy models in a damaged brain. Compared to the perfusion model, which estimates steady-state blood flow in the microcirculation, modelling oedema and osmotherapy require time-dependent effects to reflect the ICP evolution over an episode. The corresponding governing equations are

$$c_w \frac{\partial p_w}{\partial t} = \nabla \cdot (K_w \nabla p_w) + S_{cw} \tag{3.4}$$

$$c_b \frac{\partial p_a}{\partial t} = \nabla \cdot (\boldsymbol{K_a} \nabla p_a) - \omega_{ac} \cdot (p_a - p_c)\,, \tag{3.5}$$

$$c_b \frac{\partial p_c}{\partial t} = \nabla \cdot (K_c \nabla p_c) + \omega_{ac} \cdot (p_a - p_c) - \omega_{cv} \cdot (p_c - p_v) \; - \; S_{cw} \;\;, \tag{3.6}$$

$$c_b \frac{\partial p_v}{\partial t} = \nabla \cdot (\boldsymbol{K_v} \nabla p_v) + \omega_{cv} \cdot (p_c - p_v) \;\;, \tag{3.7}$$

where c_w and c_b are the storage factors of the interstitial fluid and blood in the brain tissue. The parameters p_w and K_w are the pressure and hydraulic conductivity of interstitial fluid in the interstitial space. The term S_{cw} is the fluid transport from the vasculature into the interstitial space. The value of the S_{cw} term in the normal BBB has been estimated by Fraser et al. (1990) and this value can increase by more than 100 times the normal value (Hakamata et al., 1995). Due to the large difference between the BBB permeability in the damaged region and the healthy region, the flow from capillary blood to the interstitial space and the flow of interstitial fluid in healthy tissue is thus neglected. Note that in the equations above, any terms related to displacement of the tissue are neglected; this is done as the time scale for pressure variations is much longer than that for displacement variations (Mokhtarudin, 2016). Hence, the temporal derivatives of the displacement terms can be neglected at the time scale which I am considering here. The term representing fluid transfer between the capillary and the interstitial fluid compartments (S_{cw}) is derived in Appendix A and given in Table3.2. L_p is the hydraulic permeability of the capillary wall, Π_c is the osmotic pressure for the plasma components in the blood before osmotherapy, σ is the reflection coefficient of the original plasma composition, n_b is the volume fraction of blood vessels in a unit volume of brain tissue, and R_c is the mean vessel radius. In osmotherapy, the osmotic pressure rise induced by the hypertonic saline is described by an additional term $\sigma_{NaCl}\Pi_{NaCl}$, where σ_{NaCl} is the reflection coefficient of hypertonic saline and the Π_{NaCl} is the osmotic pressure of the saline. Similarly, due to the large difference in the BBB permeability between damaged and healthy tissue, the fluid transfer through the capillary wall can be neglected in healthy tissue.

	Oedema	Healthy Tissue
Oedema Model	$S_{cw} = 2n_b \frac{L_p}{R_c}[(p_c - p_w) - \sigma \Pi_c]$	$S_{cw} = 0$
Osmotherapy Model	$S_{cw} = 2n_b \frac{L_p}{R_c}[(p_c - p_w) - \sigma \Pi_c - \sigma_{NaCl}\Pi_{NaCl}]$	$S_{cw} = 0$

Table 3.2: Fluid transfer through the capillary wall in the oedema and osmotherapy model. The derivation of these terms is shown in Appendix A*.

3.2.2.2 Boundary conditions and Initial Conditions

In the oedema model, it is assumed that there is no occlusion and therefore blood perfusion is restored. Since normal ICP is around 5-15 mmHg, the baseline value of the interstitial fluid pressure is taken here to be 10 mmHg and the boundary conditions are as given in Table3.3.

	Cortical Surface	Ventricle Surface
Arteriole Blood	$p_a = 90$ mmHg	$\boldsymbol{K}_a \nabla p_a = 0$
Capillary Blood	$K_c \nabla p_c = 0$	$K_c \nabla p_c = 0$
Venule Blood	$p_v = 15$ mmHg	$\boldsymbol{K}_v \nabla p_v = 0$
Interstitial Fluid	$p_w = 10$ mmHg	$p_w = 10$ mmHg

Table 3.3: Boundary conditions for the oedema and osmotherapy model.

Meanwhile, the pressure fields in the occluded perfusion model are used as the initial conditions for the simulation of oedema and the pressure fields at the final step in the oedema model used as the

* Appendix A is the contribution of Mokhtarudin & Payne (2015), where the Equations and models are modified and improved by Chen here for osmotherapy simulations.

initial condition for the osmotherapy model.

3.2.3 Model Coupling

The geometry of the tissue with leaking vessels is obtained from the perfusion model and is then used within the oedema model. The perfusion in brain tissue of the healthy and stroke scenarios can thus be compared. The perfusion (F) and perfusion change (ΔF) are given as

$$F = \omega_{ac}^{\square} \cdot (p_a - p_c) \ , \tag{3.8}$$

$$\Delta F = \frac{F_{\text{healthy}} - F_{\text{occluded}}}{F_{\text{healthy}}} \times 100\% \, , \tag{3.9}$$

A threshold of 70% or greater reduction in blood perfusion (Campbell et al., 2015; Payne, 2016; Jovin et al., 2017) is used to define the location of leaking vessels. Thereafter, the pressure field in the oedema is simulated until the ICP (defined to be the same as p_w) reaches equilibrium. Finally, the osmotherapy is assumed to be performed after the ICP reaches equilibrium and thus the pressures at the final step in oedema model are used as the initial pressures in the osmotherapy model, as shown in Fig.3.3.

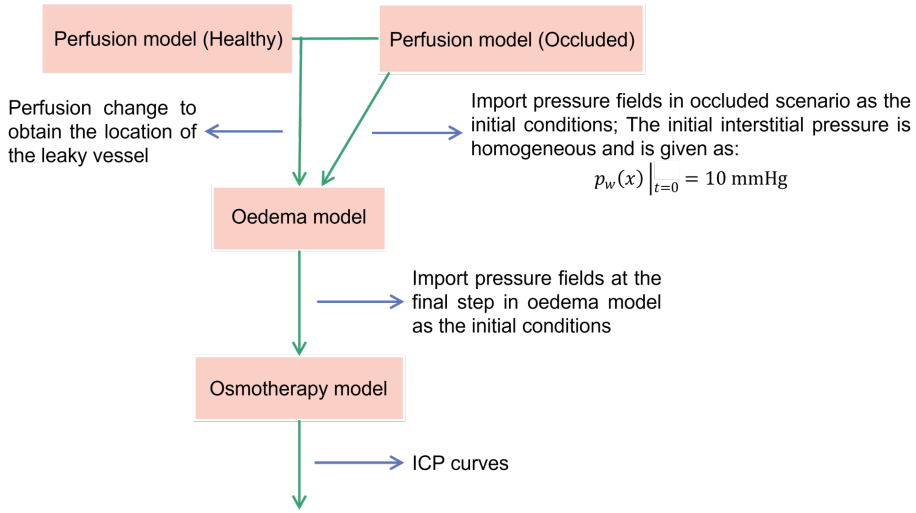

Figure 3.3: Flowchart demonstrating how the Finite Element models are coupled.

Perfusion, oedema and osmotherapy models all assume that the brain is homogeneous (within the white and grey matter) and isotropic in the interstitial space compartment. Parameters used in the models are listed in Table3.4. Although most of the values are taken from experimental studies, some of them are not readily available and thus are associated with relatively high uncertainty. Since the values of these parameters can vary significantly among previous publications, a parameter sensitivity analysis will be conducted in Section 3.3.2.

Parameter	Value	Reference(s)	Parameter	Value	Reference(s)
c_b	1.59×10^{-3} Pa^{-1}	(Su, 2011)	p_v at cortical surface	2000 Pa = 15 mmHg	(Józsa et al, 2021a)
c_w	3.08×10^{-4} Pa^{-1}	Derived from (Bai, 1993; Zienkiewicz et al., 1990; Zienkiewicz et al., 1984)	R_c	5×10^{-6} m	(Cassot et al., 2006)
$\boldsymbol{K_a}$	1.234 mm^{3}s kg^{-1}	Estimated by 0-order arteriole diameters and vessel density (Józsa et al, 2021a)	σ	0.35	Estimated from the initial ICP in oedema at the start of treatment
K_c	4.28×10^{-3} mm^{3}s kg^{-1}	(1.0×10^{-15} m², El-Bouri et al, 2016) (1.0×10^{-10} m², Tully & Ventikos, 2011)	σ_{NaCl}	0.062	Estimated from osmotic pressure of 28.9 kPa of 11.2 mmol/L of NaCl
$\boldsymbol{K_v}$	2.468 mm^{3}s kg^{-1}	Estimated by pressure and blood perfusion rate (Józsa et al, 2021a)	Π_c	2445 Pa	(Su, 2011)
K_w	3.6×10^{-3} mm^{3}s kg^{-1}	(Su, 2011)	ω_{ac}^{g}	1.326×10^{-6} Pa^{-1}s^{-1}	Derived from perfusion in grey and white matter (Józsa et al, 2021a, b)
L_p	3.0×10^{-11} m/s.Pa	(Su, 2011)	ω_{ac}^{w}	5.22×10^{-7} Pa^{-1}s^{-1}	
n_b	0.03	(Ito et al., 2001)	ω_{cv}^{w}	4.641×10^{-6} Pa^{-1}s^{-1}	
p_a at cortical surface	12000 Pa = 90 mmHg	(Józsa et al, 2021a)	ω_{cv}^{g}	1.828×10^{-6} Pa^{-1}s^{-1}	

Table 3.4: Values of model parameters used in the perfusion, oedema and osmotherapy models and their sources.

In the model, the governing equations are solved numerically using Python with a high-performance open-source Finite Element library, FEniCS (Logg & Wells, 2010; Logg et al., 2012). The highly coupled equations in the Finite Element model are solved in a mixed function space describing the multi-compartment dynamic system. The pressure in each compartment (p_i) is discretised with piecewise linear Lagrange (P1) elements. Meanwhile, the permeabilities ($\boldsymbol{K_i}$) and the other coefficients (ω_{ij}, L_p, etc) used in the model are represented in piecewise constant (dP0) tensor and scalar function spaces, respectively. The flow fields and the blood perfusion are computed in dP0 elements and are solved using the BiCojungate Gradient STABilised method (BiCGSTAB) with an Algebraic MultiGrid (AMG) preconditioner. The time steps are discretized using backward Euler scheme throughout the model. The mesh used in this study has 1.4 million tetrahedral elements and the grid convergence study in the model has been conducted in our previous research paper by Józsa et al (2021b).

3.3 Results

3.3.1 Model Validation

The concentration curve is fitted with data points measured during clinical treatment (Schwarz et al., 2002). In a previous clinical study (Schwarz et al., 2002), patients who suffered from hemispheric stroke underwent osmotherapy. Therefore, hemispheric stroke is simulated in the perfusion model to obtain the location of leaking vessels (shown in Fig.3.4). Since the location of the ICP probe is unknown, the maximum simulated ICP at different time instants is used to compare the modelled and the clinically measured ICP curves.

Meanwhile, the duration of infusion T_{in} is 15 minute, and the concentration of hypertonic saline reaches a value of 11.2 mmol/L and gradually decreases to 5.9 mmol/L 45 minute after the infusion ends (Schwarz et al., 2002). To obtain the experimental concentration curve, the

increase of concentration during the injection phase is assumed to be a sigmoid function rising from 0 to 11.2 mmol/L. After that, the additional hypertonic saline is excreted from the human body and an exponential decay with a decay rate $\dot{D} = 0.01424$ min^{-1} is thus assumed to describe the concentration drop after infusion ends.

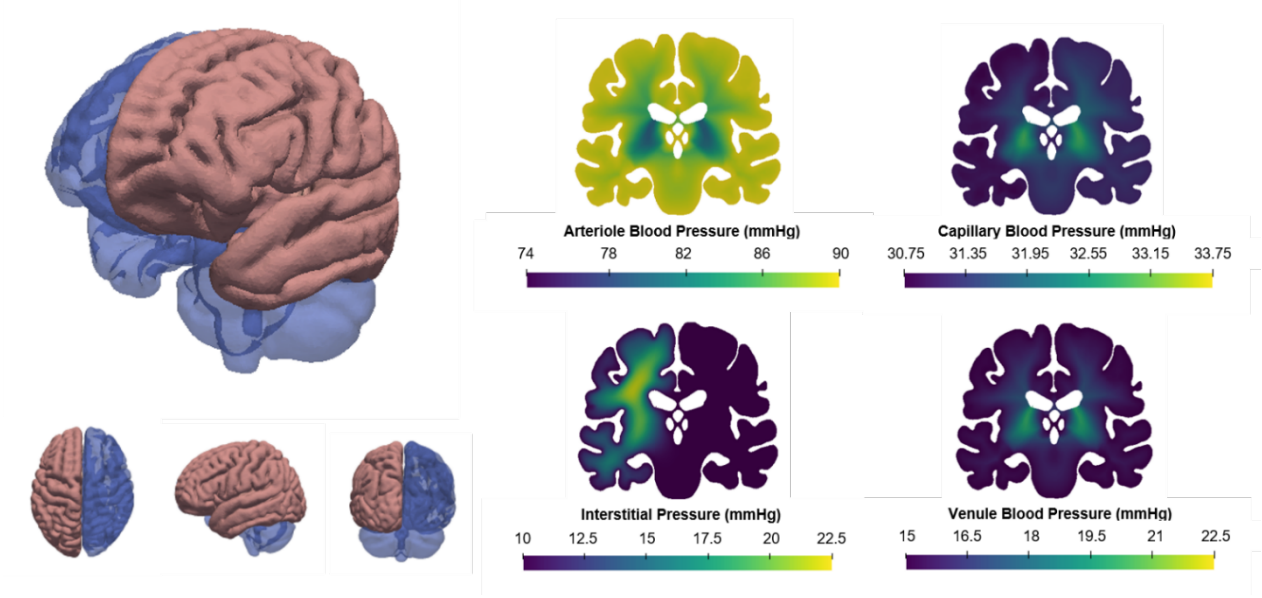

Figure 3.4: The hemispheric oedema and pressure distribution along the coronal planes in the four compartments.

The concentration obtained from the curve can then be used to derive the rise in blood osmotic pressure. The time series for NaCl osmolarity is shown in Fig.3.5a. The maximum effective osmotic pressure Π_{Max} of NaCl induced by the increase in NaCl osmolarity is 1800 Pa. Note that here, I define Π_{NaCl} as the osmotic pressure and $\sigma_{NaCl}\Pi_{NaCl}$ as the effective osmotic pressure. Based on the above, the expression for the effective osmotic pressure can be given as

$$\sigma_{NaCl}\Pi_{NaCl} = \begin{cases} \frac{\Pi_{Max}}{1+e^{15(0.5T_{in}-t)/T_{in}}}, & 0 \le t \le T_{in} \\ \Pi_{Max}e^{-\dot{D}(t-15)}, & T_{in} < t \le 240 \text{ min.} \end{cases} \tag{3.10}$$

By substituting the effective osmotic pressure $\sigma_{NaCl}\Pi_{NaCl}$ into the governing equations, I

obtain the simulation results of the dynamic ICP during an episode of osmotherapy (Fig.3.5b).

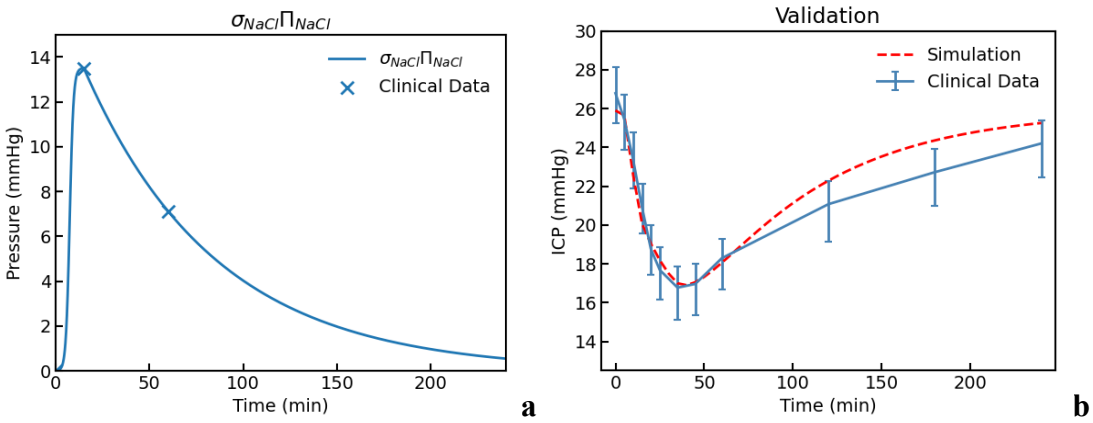

Figure 3.5: The effective osmotic pressure of hypertonic saline with clinical data points (left) and the validation curve of the ICP. The clinical data obtained from 22 osmotherapy episodes are presented as mean±SE (right), where SE is the square error. The initial ICP is much higher than normal value due to the oedema and drops to a nadir value due to the injection of osmotic agent. Due to the excretion of the agent, the ICP rises back to the peak value gradually after 35 minutes. The clinical data points are collected from (Schwarz et al., 2002)

3.3.2 Sensitivity Analysis of Physiological Parameters and Treatment Effectiveness

Parameter variability leads to uncertainties in treatment effectiveness, which makes it important to study the effects of changes in various physiological parameters. By examining Equation 3.4 which governs the interstitial fluid pressure, the parameters that can influence the simulation results are the hydraulic conductivity, capillary wall permeability, capillary blood pressure, blood osmotic pressure and baseline ICP. In addition, the size of malignant stroke (L-MCA, hemispheric etc.) is also of clinical significance.

The initial ICP should lie within the range of [20; 25] mmHg since only then will osmotherapy be necessary. Accordingly, the parameter values are varied within reasonable ranges (Appendix B, TableB1). In this parameter sensitivity analysis, the parameter values from Table3.4 are used

as baseline values.

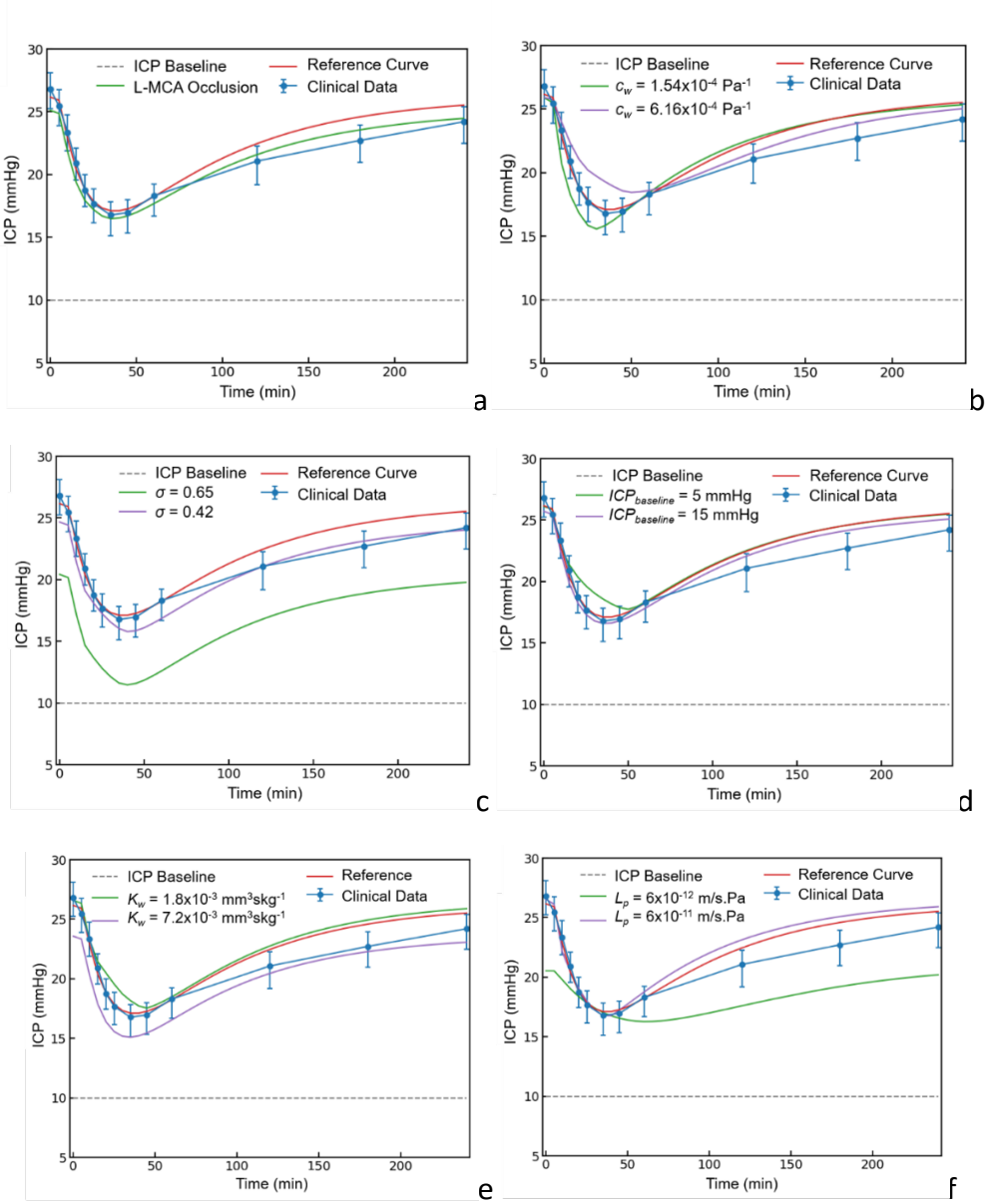

Figure 3.6: The evolution of ICP in osmotherapy under varying physiological parameters. (a) Varying oedema size. (b) Varying storage factor. (c) Varying reflection coefficient of the original plasma composition. (d) Varying ICP baseline. (e) Varying tissue hydraulic conductivity. (f) Varying capillary wall permeability. The reference curve corresponds to the validation case shown in Figure 3.5b.

Fig.3.6 summarises the results of the sensitivity analysis. The effectiveness of osmotherapy is of great clinical significance since it is a major clinical concern to achieve a trade-off between

lowering ICP and controlling the side effects. To discuss the effectiveness of the osmotherapy E_{Mean} is introduced as is the ratio of the mean ICP drop over 240 minutes (same as the time frame of the clinical data) and the mean increased effective osmotic pressure induced by the hypertonic saline infusion:

$$E_{Mean} = \frac{\int_0^{240} (ICP_{t=0} - ICP)\, dt}{\int_0^{240} \sigma_{NaCl} \Pi_{NaCl}\, dt}. \quad (3.11)$$

Parameter sensitivity in terms of E_{Mean} is listed in Table3.5.

E_{Mean}(%)			
Reference Value	93.17	c_w = 6.16×10^{-4} Pa^{-1}	93.80
L-MCA Occlusion	90.71	c_w = 1.54×10^{-4}Pa^{-1}	95.63
$ICP_{baseline}$ = 5 mmHg	94.55	K_w = 1.8×10^{-3} mm^{3}s kg^{-1}	94.87
$ICP_{baseline}$ =15 mmHg	88.68	K_w = 7.2×10^{-3} mm^{3}s kg^{-1}	84.34
σ = 0.42	92.28	L_p= 6.0×10^{-12}m/s.Pa	55.10
σ = 0.65	92.83	L_p= 6.0×10^{-11}m/s.Pa	101.62

Table 3.5: Values of E_{Mean} under various physiological parameters.

It can be seen that changing oedema size from hemispheric (93.17%) to L-MCA (90.71%) leads to a difference of -2.46% in E_{Mean}. Similarly, baseline ICP (1.38%, -4.49%), σ (-0.89%, -0.34%), storage factor of interstitial fluid tissue (0.63%, 2.46%) show only slight effects on E_{Mean}, while the effects of capillary wall permeability and tissue conductivity are much more significant. Particularly, the treatment effectiveness varies from 55.10% to 101.62%, depending on the value of capillary wall permeability.

3.3.3 Retention Time and Injection Doses are the Major Factors Affecting Effectiveness

Next, I investigate the impact of infusion time, retention time and injection dose (measured by

the osmotic pressure of saline in blood) on effectiveness defined by E_{Mean}. These parameters can be studied by varying Π_{Max}, T_{in} and $\dot{D}$ in Equation 3.10. The doses are the Π_{Max}, maximum effective osmotic pressure of saline in the blood during injections. Meanwhile, the infusion time T_{in} is the duration of injection, which usually varies from 10-30 minutes in clinical treatments. The retention time describes the half-life of injected saline in the human body, and it usually varies from 30 to 60 minutes (Paczynski, 1997).

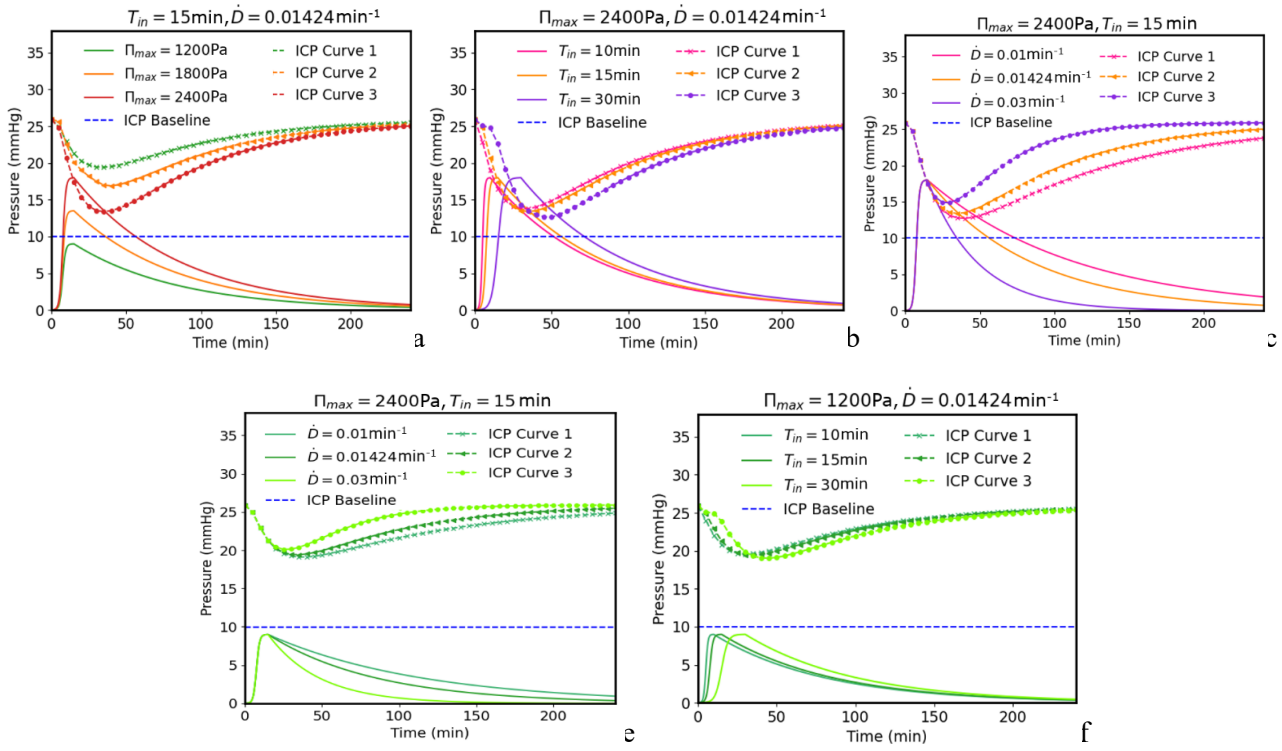

Figure 3.7: The evolution of ICP and effective osmotic pressure in osmotherapy under various administration protocols. (a) Varying maximum effective NaCl osmotic pressure from 1200 to 2400 Pa. (b) Varying infusion time with maximum effective NaCl osmotic pressure of 2400 Pa. (c) Varying decay rate with maximum effective NaCl osmotic pressure of 2400 Pa. (d) Varying infusion time with maximum effective NaCl osmotic pressure of 1200 Pa. (e) Varying decay rate with maximum effective NaCl osmotic pressure of 1200 Pa.

In the simulations presented here, hypertonic saline is administered at various infusion times (10, 15, 30 minutes), doses (1200, 1800, 2400 Pa) and the decay rates $\dot{D}$ of NaCl are also varied so that NaCl half-life ranges from 30 minutes to 1 hour. In Fig.3.7, it is shown that only retention

time and dose have a significant effect on the ICP evolution while the effects of infusion time are essentially negligible. Meanwhile, it is also worth noting that an increase in NaCl retention time can lead to a lower ICP nadir value without a higher osmolarity of NaCl.

3.3.4 Two Possible Scenarios of Osmotherapy Failure

Changes in physiological parameters are shown to play an important role in osmotherapy and hence to influence the effectiveness of treatment. It should be noted that parameters such as baseline ICP, tissue conductivity and storage factors are the parameters that are essentially irrelevant to the severity of BBB damage and thus can be assumed for modelling purposes to be similar among individuals. In contrast, the capillary wall permeability and reflection coefficients (σ and σ_{NaCl}) are determined by the severity of BBB damage and therefore can lead to uncertainties in the outcome of clinical treatment. Here, simulation results of two scenarios where osmotherapy could fail to lower the ICP to 15 mmHg are presented: $L_p = 3 \times 10^{-11}\mathrm{m/s.Pa}$, $\sigma = 0.35$, $\sigma_{NaCl} = 0.0325$; $L_p = 6 \times 10^{-12}\mathrm{m/s.Pa}$, $\sigma = 0.05$, $\sigma_{NaCl} = 0.0625$. In the first scenario, the low reflection coefficient of saline leads to reduced $\sigma_{\mathrm{NaCl}}\Pi_{\mathrm{NaCl}}$ under the same osmolarity and thus impairs the effectiveness of osmotherapy. In scenario two, the effectiveness of osmotherapy is affected by the low L_p which hampers the flow of oedematous fluid back into the vasculature.

In Fig.3.8, scenario 0 represents a successful treatment when the physiological parameters are chosen to be the reference values and the maximum effective osmotic pressure of NaCl is 2400 Pa. In contrast, both scenario1 and 2 show an insufficient ICP drop during the osmotherapy as the ICP curve is continuously above 15 mmHg. Since the goal of osmotherapy is to achieve an ICP below 15 mmHg and therefore the ICP drop is insufficient in scenario 1 and 2.

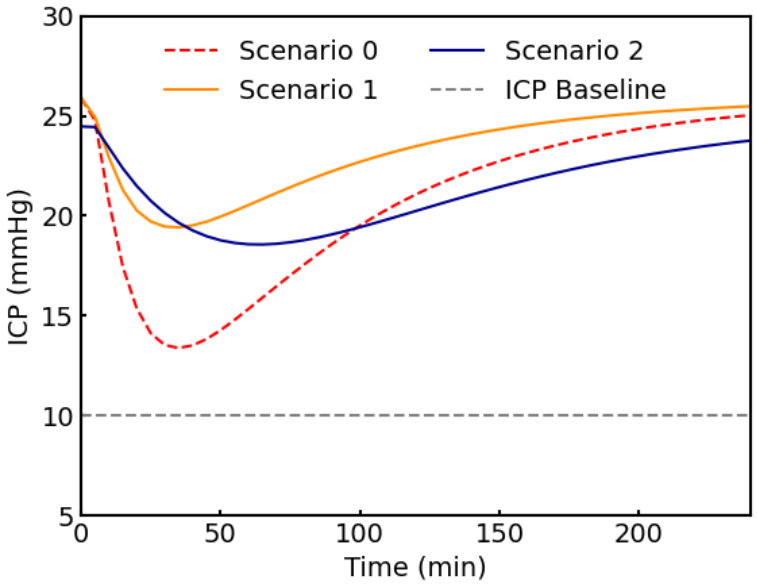

Figure 3.8: The evolution of ICP in scenarios 1 and 2.

In Fig.3.9, the mean ICP drop over 240 minutes is plotted versus the mean increased effective NaCl osmotic pressure to show the effectiveness of osmotherapy under various administration protocols. The red line shows the reference line showing the effectiveness of bolus injection with the maximum dose and the blue line shows the effectiveness of bolus injection with the minimum dose. When L_p is high and σ_{NaCl} is low, the effect of NaCl is not significantly affected by the mean NaCl effective osmotic pressure and the continuous injections show similar effectiveness. Furthermore, a rise in the mean NaCl effective osmotic pressure leads to not just an increase in mean ICP drop, but also increases effectiveness in the low L_p case. In contrast, the rise in mean osmotic pressure leads to a slight drop in effectiveness when the L_p value is high.

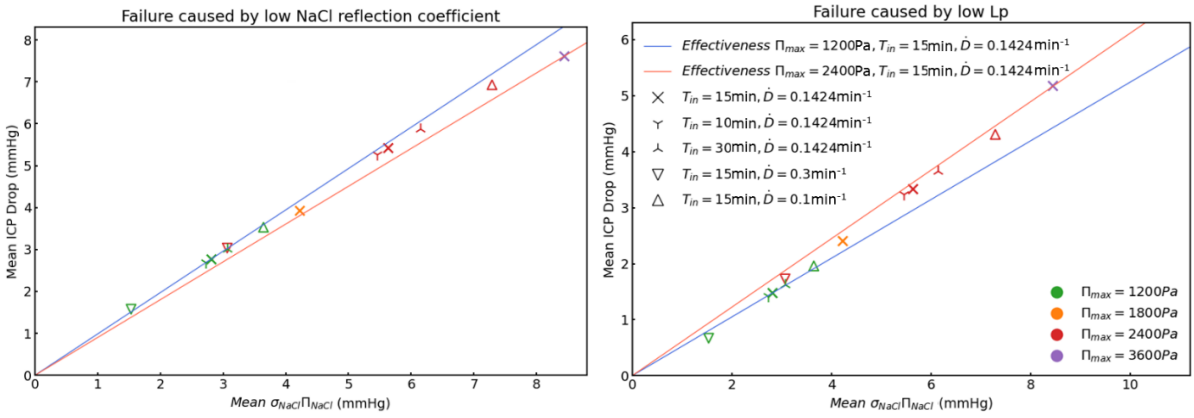

Figure 3.9: The mean ICP drop over 240 minutes versus the mean increased effective osmotic pressure induced by the hypertonic saline infusion.

3.4 Discussion

The validation results presented here show that the simulation results match well with clinical data collected from 8 patients who underwent 22 episodes of osmotherapy. As shown in Fig.3.5b, there is generally an excellent agreement between the simulation result and the clinical data, with most of the data points lying within the error bar. Although the infusion ends at 15 minutes, it takes time for the brain to respond and the minimum ICP is reached at around 35 minutes after the onset. Furthermore, compared to the good match during the first 60 minutes, there appears to be a slightly larger discrepancy between the simulation result and the clinical data after this time. This can be partly explained by the fact that influencing factors such as further medication and nursing care are not considered after 60 minutes in the clinical study. The infusion is only 60 minutes long and thus the clinicians could hence only monitor the patients during the first 60 minutes. Overall, the validation thus shows a very good match between clinical data and simulation results.

In this study, the baseline ICP is varied to 5 mmHg and 15 mmHg, i.e., to the minimum and maximum normal ICP values respectively. Due to the lower ICP baseline, the difference

between blood pressure is larger and this thus increases the rise in ICP. As a result, the net effects of ICP baseline on osmotherapy are negligible. Meanwhile, when the tissue storage is small, the drop and rebound of ICP is faster and the ICP reaches a lower bottom value. However, the tissue storage only slightly affects the ICP when it is varied within 50% to 200% of baseline. Larger tissue conductivity leads to a lower initial ICP and slower ICP response and varying the value from 50% to 200% does not affect the ICP significantly. In contrast, the reflection coefficient of the original blood plasma composition shows a strong effect on the curve. This is mainly because of the change in initial oedema pressure. The curves follow a similar pattern to the reference curve and reach the bottom ICP value at around 35 minutes while the maximum ICP drop over 240 minutes remains almost the same. Meanwhile, an increased L_p is found to affect the overall response of ICP to osmotherapy since it affects the fluid transfer between vasculature and interstitial space.

The osmotherapy in oedema after L-MCA occlusion has been compared with the reference curve (hemispheric oedema) and no significant difference is shown in the simulation results. This is because the interstitial pressure is determined by the pressure difference between the capillary blood and interstitial space. Although osmotherapy and its side effects have been extensively reviewed in meta-analysis studies, how the patient-specific physiological parameters affect the ICP remains unclear. In this study, the effects of the varying physiological parameters have thus been studied quantitatively for the first time. It is shown that the L_p tissue conductivity and reflection coefficients are the most important parameters to consider in osmotherapy.

This study also finds that the doses of the injection and the retention time of ICP are the most important factors affecting the ICP evolution, whereas the infusion time does not show any significant effects. In contrast, a long retention time maintains the osmotic pressure after the

infusion ends and therefore leads to a lower ICP bottom value. A longer retention time can also be achieved by injecting osmotic agents at a certain rate following the bolus injection (Biestro et al., 1997). This suggests that maintaining the osmotic pressure by combining the bolus with a continuous injection can potentially help to lower and to maintain ICP at a lower value.

Two scenarios that lead to osmotherapy failure have also been presented (Fig.3.8). Although there are other parameters, including tissue conductivity, that can affect the response of ICP, it is shown here that a failure of osmotherapy caused by a low NaCl reflection coefficient shows a fast response, but insufficient ICP drop. Meanwhile, failure caused by a low capillary wall permeability usually demonstrates a slower response of ICP. Accordingly, strategies to deal with ineffective treatment can be categorised into two types. In the scenario where an insufficient ICP drop is caused by a low NaCl reflection coefficient, the ICP response is fast while the ICP drop is small. In this case, although the rise in NaCl osmolarity can lead to a larger ICP drop it also indicates that it is worth trying other types of osmotic agents such as mannitol and glycerol whose reflection coefficient could be larger (Nau, 2000; Ziai et al., 2007). In scenario 2, the response in ICP is slow when the L_p is low. Effectiveness is not likely to rise when using other types of osmotic agents since the effectiveness is limited by the low capillary wall permeability. Therefore, it is suggested that larger doses and longer retention time be used to achieve a lower bottom ICP value. Once a lower ICP nadir value is achieved, it takes a long time for the ICP to rebound in low capillary wall permeability and thus the effectiveness can be improved. In clinical settings, the fast and slow response ICP curves do not require any accurate measurement of ICP, and it is therefore not necessary to take the risk of employing invasive ICP monitoring (Robba et al., 2016). Instead, non-invasive methods (such as MLS, optic nerve sheath diameter method) can be used to obtain the ICP curve and help to determine the cause for insufficient ICP during osmotherapy (Raboel et al., 2012; Ragauskas et al., 2012).

3.4.1 Limitations

It should be noted that there are several limitations to this study. Firstly, many parameters have been used in the multi-compartment models and it is always difficult to determine some of the parameters from existing experimental data. Due to the various experimental methods adopted in the previous studies, the parameters shown in experimental studies vary significantly, even though the real physiological values usually do not vary beyond the 50%-200% range (see for example, Sack et al., 2009; Montagne et al., 2015; Budday et al., 2020). Additionally, some of the parameters are not yet available in the human brain and data from animals were thus used as necessary (Harper & Bohlen, 1984; Józsa et al., 2021a). Secondly, the multi-compartment porous model relies on multiple scale separation and homogenisation of the brain. It has been pointed out that the vessel diameter in the vasculature changes continuously, therefore the applicability of scale separation is questionable (Peyrounette et al., 2018). Meanwhile, the homogenisation of the brain behaviour neglects the differences in the properties of tissue in different regions and only the differences between white and grey matter are considered. The properties of different brain regions remain unclear, and the experimental data are not sufficient for a brain model with more anatomical details. Thirdly, the following features are not considered in the model: the temporal changes in the parameters; cerebral autoregulation; the effects of brain tissue mechanics on the interstitial fluid pressure; and the (highly complicated) biochemical reactions during the injection of hypertonic saline. Specifically, cerebral autoregulation is restored after infusion (Zipfel et al., 2021) and this might thus be a crucial factor that can lead to a slower rebound in the clinical data compared to the simulation results.

In conclusion, the first model for osmotherapy is presented and the simulation results are found to be in good agreement with the clinical data. Different types of injection and osmotherapy under different parameters are simulated to help predict optimised therapeutic strategies for patients having different types of unsuccessful treatment. This model can hopefully be further

developed to achieve better accuracy and to provide more detailed guidelines for the clinical treatment of oedema.

Author Contributions

Xi Chen: Conceptualisation, Methodology, Investigation, Validation, Visualisation, Writing - Original Draft, Software, Data Curation.

Dr. Tamas. I. Józsa: Software, Writing - Review & Editing.

Prof. Stephen J Payne: Supervision, Writing - Review & Editing.

Chapter 4

Mathematical Modelling of Haemorrhagic Transformation in the Human Brain*

In this Chapter, the osmotherapy model is further developed by including haemorrhagic transformation. In severe BBB damage, vessel wall ruptures, and blood components and blood usually flow into the interstitial space spontaneously. However, the role of biomechanical factors in haemorrhagic transformation remains unclear. Here, the model is validated with clinical imaging data and utilised for the investigation of the impact of blood glucose, BBB damage severity, blood pressure on haemorrhage development.

* The contents of this chapter are reproduced without change from (Chen et al., 2023). This Chapter is the collaborative work of Xi Chen and Jiayu Wang. During the collaboration, Xi Chen worked on the modelling of brain haematoma and contributed the FEniCS code for haematoma simulation. Wang worked on the MATLAB clinical data processing code. Both Chen and Wang contributed to the conceptualisation, clinical data acquisition and data analysis of the results. The paper writing is done by both Chen and Wang. The Introduction, Results and Discussion are completed by both of Chen and Wang. Meanwhile, section 4.2.1- 4.2.2 of Methods is completed by Chen and section 4.2.3 of Methods is completed by Wang. Author contribution is listed at the end and the work by Wang will be labelled in footnote throughout this Chapter.

4.1 Introduction*

Stroke is one of the most important causes of damage to the brain and was ranked as the second leading cause of death across the world in 2018 (Katan & Luft., 2018). The incidence of stroke is predicted to continue to increase in ageing populations. Haemorrhagic transformation (HT) is one of the most common complications after ischaemic stroke, caused by damage to the blood–brain barrier (BBB) that can be the result of stroke progression or a complication of stroke treatment with reperfusion therapy. HT is a frequent, often asymptomatic, complication (Álvarez-Sabín et al., 2013) that has the potential to lead to long-term morbidity and mortality (Marsh et al., 2013).

The Heidelberg Bleeding classification which incorporates the European Cooperative Acute Stroke Study (ECASS) classification, classifies HT based on its radiological appearance on follow-up computed tomography (CT) or magnetic resonance imaging (MRI) (von Kummer et al., 2015): haemorrhagic infarction type 1 (HI1), which is defined as small petechiae (tiny spots of bleeding) along the peripheral margins of infarct; haemorrhagic infarction type 2 (HI2) as confluent petechiae within the infarcted area but without mass effect; parenchymal haematoma type 1 (PH1), defined as blood clots in ≤ 30% of the infarcted area with some slight mass effect; and parenchymal haematoma type 2 (PH2) as blood clots in > 30% of the infarcted area with substantial mass effect. HT can also be quantified by measuring its volume and large volumes were associated with poor functional outcomes (Van Kranendonk et al., 2020). HT is often located in the internal regions of the brain: putaminal (occurrence: 46.2%), thalamic (occurrence: 19.4%) and pontine (occurrence: 14%) (Nah et al., 2012).

---

* Wang contributed to the medical background of haemorrhagic transformation and Chen contributed to the literature review of computational modelling in the Introduction section.

The severity of HT is highly variable and a key question is whether the occurrence and severity of HT can be predicted accurately after ischaemic stroke, based on available imaging data and clinical parameters. Wang and Payne (2021) first proposed a mathematical model that describes the behaviour of HT within a 2D vasculature model. In this vasculature model, the geometries of vessels in the same generation were the same. However, based on anatomical studies, capillaries have been shown to have a more web-like than tree-like structure (Duvernoy et al., 1981). In addition, the effects of HT on surrounding normal vessels and tissue were not considered in this initial model.

Wang et al. (2022a), extended the previous model to an enlarged vasculature length scale in order to compare the model predictions more accurately with the human vasculature. The penetrating model they used was that of El-Bouri and Payne (2018) and they investigated the effects of HT on the surrounding tissue and vessels. It was found that perfusion reduces by approximately $13-17\,\%$ and cerebral blood volume (CBV) reduces by around $20-25\,\%$ after HT onset due to the effect of capillary compression caused by increased interstitial pressure. However, this model focuses on a length scale of around $1\,\mathrm{mm}$, which remains difficult to compare with imaging data.

Therefore, it is necessary to extend the HT model to a full brain length scale ($100\,\mathrm{mm}$) and validate this model with real imaging data, as shown in Fig.4.1. Various full brain models have been developed, for example, to investigate the correlation between stress and midline shift (MLS) (Bing et al., 2020), to study the importance of different constitutive relationships and material properties (Weickenmeier et al., 2017), to explore the risk factors associated with the early stages of Alzheimer's disease (Guo et al., 2018) and to simulate tissue perfusion (Padmos et al., 2021). However, a full brain model that describes HT has not previously been developed.

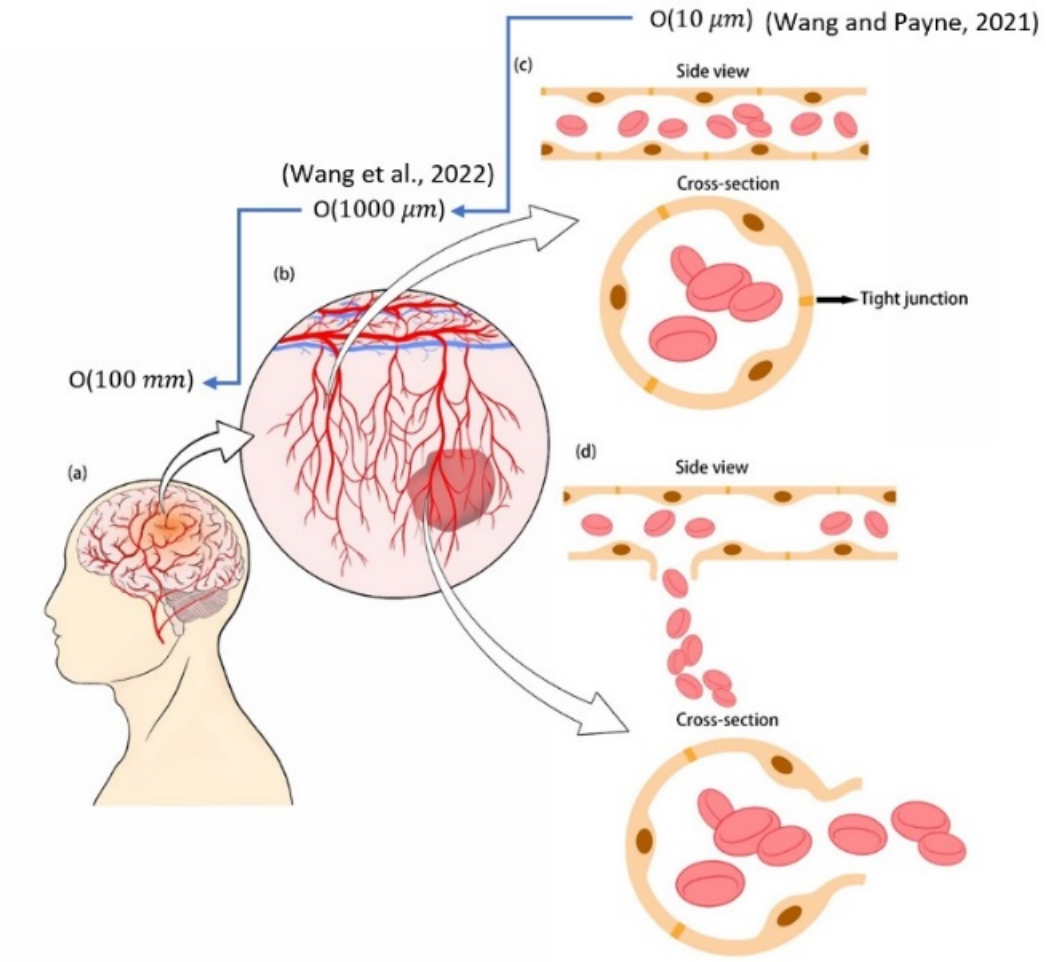

Figure 4.1: Macroscopic (a) and microscopic (b, c, d) configurations of haemorrhagic transformation (HT) simulation across different length: (a) HT model in the entire human brain (present study); (b) simulation of HT in penetrating vessel network; (c) healthy vessel; (d) BBB breakdown and haemorrhage modelling around a single vessel. Figure adapted from Wang & Panye (2021) with permission.

The aim of this study is thus to develop a model which can simulate the severity of haemorrhage in a full brain model. In addition, this model has the potential to be used to help clinicians to determine the bleeding region more accurately. We used the HT model developed by Wang and Payne (2021) and Wang et al. (2022a), which we further extended by inclusion of an oedema model developed by Mokhtarudin and Payne (2015) and Chen et al., (2022).

The developed HT model is applied to provide information in addition to a perfusion model described by Guo et al. (2018), Padmos et al. (2021) and Józsa et al. (2021a) . Then our results are compared with imaging data from the MR CLEAN-NO IV trial (LeCouffe et al., 2021). Properties such as haematoma volume are estimated and compared with neuroimaging measurements (Jain et al., 2013; LeCouffe et al., 2021). By comparing with the clinical data, the parameters used for our simulations, such as the definition of haematoma surface pressure, can be optimised. We then conclude by investigating the factors that may affect the severity of HT, including increased blood viscosity and blood pressure.

4.2 Materials and Methods*

The model consists of two components that simulate blood perfusion and individual haematomas respectively. Similarly, we use the perfusion model presented in Chapter 3 as the criteria to determine the brain damage region. An additional model for blood leakage will be introduced before being coupled with perfusion model. The methods to provide quantification of HT will then be introduced.

4.2.1 Leakage Model

4.2.1.1 Governing Equations

In this model, the blood is assumed to leak into the interstitial space and an additional compartment for the interstitial flow is thus required. Therefore, a porous circulation model with 4 compartments (arteriole, capillary network, venule, and interstitial space) is proposed here to predict the growth of a haematoma and the change in cerebral blood flow (CBF) and perfusion before and after HT. The blood leakage is modelled using the capillary wall filtration model and the flow rate can be written as (Starling, 1896; Mokhtarudin, 2016):

* Wang contributed to the MATLAB code for clinical image processing (4.2.3) and the Chen contributed to the computational model 4.2.1-4.2.2

$$S = \begin{cases} 2\bar{n}_b \frac{L_p}{R_c}(p_c - p_w) & \text{in bleeding tissue} \\ 0 & \text{in healthy tissue} \end{cases} \tag{4.1}$$

where $\bar{n}_b$ is the volume fraction of blood vessel in a unit volume of brain tissue, L_p denotes the vascular permeability, R_c denotes vessel radius, p denotes the hydrostatic pressure with subscripts that represent capillary blood pressure and interstitial fluid pressure respectively and S denotes the leakage flow rate.

Here, the compression of the capillary blood vessels is also considered using the tube law (Drzewiecki et al., 1997; Mokhtarudin, 2016), and the capillary compression function is assumed to be of the form:

$$f = \frac{1}{2}\left[1 + \tanh\left(1 + \frac{\bar{p} - p_w}{0.01E}\right)\right]) \tag{4.2}$$

where f denotes the fraction of vessels remaining open, $\bar{p}$ is the baseline value of interstitial pressure, and E is the bulk modulus representing the capillary wall stiffness. Since the blood flow into the haematoma compresses the tissue, it acts to squeeze the interstitial fluid in the brain. Therefore, the blood flow and the interstitial flow driven by the growing haematoma both need to be considered. There are no current experimental data available to define the surface of a haematoma. Hence, in these simulations, in order to obtain reasonable values of haematoma volume, we set the threshold of haematoma surface pressure, $p^* = 3.5$ mmHg above the baseline tissue pressure. The value is chosen following simulations (results not shown) that show that this value appears to be the optimal one to obtain haematoma volumes that match clinical imaging data reasonably well. The

sensitivity analysis for this haematoma surface pressure will, however, be presented and discussed later.

Based on our knowledge, there is currently no anatomical data of the bleeding proportion in different types of vessels in HT. In this model, we assumed that only the capillaries are leaky when HT occurs. Gliem et al. (2012) found that bleeding frequently occurred around thin-walled vessel in the infarct border zone and the capillary wall thickness is around $2\ \mathrm{um}$ (Lucas, 2013; Payne & Lucas, 2018). In addition, based on morphological measurements of the frequency distribution of vessels diameter, majority of vessels are found to be capillary vessels (Lauwers et al., 2008). Furthermore, Wang, et al. (2022a) found that the larger leaky vessel led to larger haematoma volume and in this simulation, the PH2 type of HT is excluded. Therefore, in terms of to determine the bleeding regions in different compartments (arteries, capillaries and veins), we assume the leakage only occurs in the capillary compartment. The governing equations for the leakage model can be written as the following:

$$\nabla \cdot (\frac{K}{\mu} \nabla p_w) = -f \cdot S \tag{4.3}$$

$$\nabla \cdot (\frac{\boldsymbol{K_a}}{\mu_b} \nabla p_a) = \ f \cdot \omega_{ac} \cdot (p_a - p_c) \tag{4.4}$$

$$\nabla \cdot (\frac{K_c}{\mu_b} \nabla p_c) = \ -f \cdot \omega_{ac} \cdot (p_a - p_c) + f \cdot \omega_{cv} \cdot (p_c - p_v) \ + \ f \cdot S \tag{4.5}$$

$$\nabla \cdot (\frac{\boldsymbol{K_v}}{\mu_b} \nabla p_v) = \ -f \cdot \omega_{cv} \cdot (p_c - p_v) \tag{4.6}$$

where μ denotes fluid viscosity in the interstitial space. The permeability of fluid in the interstitial space depends on whether the space is occupied by blood or interstitial fluid. Since the fluid component is assumed to be determined by a pressure threshold $p^* = 3.5\ \mathrm{mmHg}$, the tissue permeability of fluid in the interstitial space depends on pressure values and it is thus assumed to be of the form:

$$\frac{K}{\mu} = \frac{K_w}{\mu} + \frac{1}{2}(\frac{K_b}{\mu} - \frac{K_w}{\mu}) \cdot (1 + \tanh(\ 1 + \frac{\bar{p} - p_w}{0.1\ \mathrm{mmHg}})) \tag{4.7}$$

where K_w and K_b denote the conductivities of water and blood in the interstitial space, respectively. By implementing a tissue conductivity that varies with pressure, we can simulate both the flow of oedema fluid and blood.

4.2.1.2 Boundary Conditions

In the haematoma model, following removal of the occlusion, the blood perfusion is assumed to be fully restored. Although this is a strong assumption imposed for simplicity, it will be possible in future to examine the effect of incomplete restoration. The perfusion then leads to an increased blood pressure on the blood vessel wall and causes vessel rupture and the formation of a haematoma. Constant pressure boundary conditions are imposed on the pial surface for all subregions. The interstitial space boundaries are the interface between interstitial fluid and cerebrospinal fluid and the pressure is assumed to be constant due to the high compliance of the cerebrospinal fluid (CSF) (Mokhtarudin & Payne, 2017). The boundary conditions for the haematoma model are given in Table4.1.

	Cortical Surface	Ventricle Surface
Arteriole Blood	$p_a = 90$ mmHg	$\boldsymbol{K}_a \nabla p_a = 0$
Capillary Blood	$\nabla p_c = 0$	$\nabla p_c = 0$
Venule Blood	$p_v = 15$ mmHg	$\boldsymbol{K}_v \nabla p_v = 0$
Interstitial Fluid	$p_w = 10$ mmHg	$p_w = 10$ mmHg

Table 4.1: Boundary conditions for the haematoma model.

4.2.2 Model Coupling

In the perfusion model, it is assumed that the locations with higher values of capillary blood pressure are prone to vessel disruption, BBB breakdown, and consequently HT. Since

haematoma is likely only to occur in the infarcted region, a 70% perfusion reduction is used as the primary threshold for the tissue bleeding (Campbell et al., 2015; Payne, 2016; Jovin et al., 2017). Furthermore, although subcortical HT has been found to appear more frequently than cortical HT, it should be noted that the prediction of the precise spatial location of the haematoma is highly challenging. To obtain the haematoma locations that match the clinical images, capillary pressure ranges were varied and used as the secondary threshold for vessel rupture and tissue bleeding. The geometry of the bleeding tissue obtained from the perfusion model was then included within the leakage model to simulate the growth of the haematoma and the resulting perfusion reduction.

1. The heathy perfusion is simulated to obtain the healthy blood flow (Fig.4.2a).

2. The occluded subregions are chosen (Fig.4.2b) to obtain the stroke blood perfusion (Fig.4.2c).

3. Patient-specific capillary pressure ranges are chosen manually. Regions with 70% perfusion reduction (Fig.4.2d) and over where the capillary blood pressure lie in the ranges are defined as bleeding tissue for each patient.

4. The regions chosen as bleeding tissue are imported into the leakage model for haematoma simulation (Fig.4.2e).

5. The haematomas are defined as regions with interstitial pressure rise over 3.5 mmHg. Comparison in the pairs of haematoma centre locations (x_i, y_i,z_i) and volumes, which are obtained from the computational model and clinical images is performed (Fig.4.2f). If the differences do not lie in a reasonable range (the differences in pairs of x values, y values and z values from the computational model and imaging data are < 5%), then go back to step 2 until a reasonable hematoma is obtained.

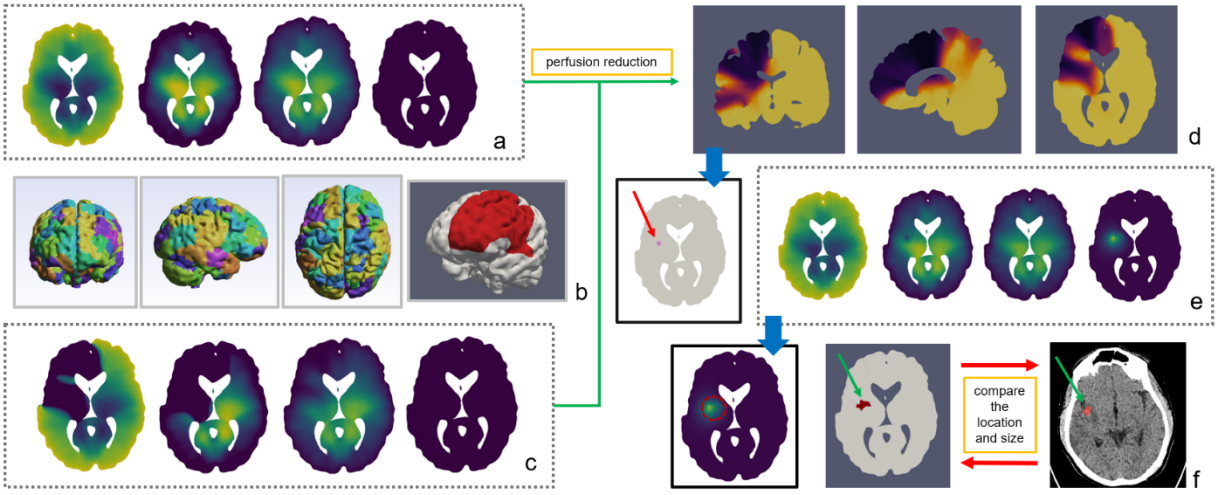

Figure 4.2 (a) Simulation of blood pressures in healthy blood flow in the arteriole, capillary, venule and interstitial space, respectively. (b) Subregions on the cortical surface and selection of the occluded regions (red). (c) Simulation of brain blood pressures in infarction. A reduction in blood pressures in the occluded region is shown as the colour darkens. (d) Blood perfusion reduction obtained from the healthy and stroke cases. (e) Bleeding tissue is assumed to occur in the regions where perfusion reduction is over 70% and is chosen by varying the capillary blood pressure ranges. The bleeding tissue is then imported into the leakage model for the simulation of the growth of hematoma. (f) 3.5 mmHg of pressure rise is used as the threshold of hematoma boundary and the hematoma is compared with the CT images.

In the model, the governing equations are solved numerically using Python with a high-performance open-source Finite Element library, FEniCS (Logg & Wells, 2010; Logg et al., 2012). The highly coupled equations in the Finite Element model are solved in a mixed function space describing the multi-compartment dynamic system. The pressure in each compartment (p_i) is discretised with piecewise linear Lagrange (P1) elements. Meanwhile, the permeabilities ($\boldsymbol{K_i}$) and the other coefficients (ω_{ij}, L_p, etc) used in the model are represented in piecewise constant (dP0) tensor and scalar function spaces, respectively. The flow fields and the blood

perfusion are computed in dP0 elements and are solved using the BiCojungate Gradient STABilised method (BiCGSTAB) with an Algebraic MultiGrid (AMG) preconditioner.

All the parameters used in the models and their sources are given in full in Table4.2.

Parameter	Value	Reference(s)
$\boldsymbol{K_a}$	4.4424×10^{-12} m^2	Estimated by 0-order arteriole diameters and vessel density (Józsa et al., 2021a)
K_c	1.5408×10^{-14} m^2	1.0×10^{-15} m^2 (El-Bouri & Payne, 2016); 1.0×10^{-10} m^2 (Tully & Ventikos, 2011)
$\boldsymbol{K_v}$	8.8848×10^{-12} m^2	Estimated by pressure and blood perfusion rate (Józsa et al., 2021a)
K_w	3.6×10^{-15} m^2	(Su, 2012)
K_b	1.0×10^{-15} m^2	(Su, 2012)
ω_{ac}^{w}	1.326×10^{-6} Pa$^{-1} \cdot$ s^{-1}	Derived from perfusion rates in grey and white matter (Lüders et al., 2002; Józsa et al., 2021a)
ω_{ac}^{g}	5.22×10^{-7} Pa$^{-1} \cdot$ s^{-1}	
ω_{cv}^{w}	4.641×10^{-7} Pa$^{-1} \cdot$ s^{-1}	
ω_{cv}^{g}	1.828×10^{-6} Pa$^{-1} \cdot$ s^{-1}	
p_a at cortical surface	12000 $Pa = 90$ mmHg	(Józsa et al., 2021a)
$\bar{p}$	10 mmHg	(Payne, 2006)
p_v at cortical surface	2000 $Pa = 15$ mmHg	(Józsa et al., 2021a)
L_p	3.0×10^{-11} m $\cdot$ Pa$^{-1} \cdot$ s^{-1}	(Su, 2012)
R_c	5.0×10^{-6} m	(Cassot et al., 2006)
$\bar{n}_b$	0.03	(Ito et al., 2001)
μ_b	3.6×10^{-3}Pa $\cdot$ s	(Su, 2012)
μ	1.0×10^{-3}Pa $\cdot$ s	(Mokhtarudin & Payne, 2015)

Table4.2: Values of model parameters used in the perfusion, oedema and osmotherapy models and their sources.

4.2.3 Quantifications of CT Images

We included patients with HT from the MR CLEAN-NO IV trial (LeCouffe et al., 2021). The

MR CLEAN-NO IV trial was a multicentre randomized controlled trial that assessed the effect of EVT alone compared with IVT before EVT after acute ischaemic stroke due to large vessel occlusion. The study protocol of MR CLEAN-NO IV has previously been described by Treurniet, et al. (2021). HT was assessed on follow-up CT according to the Heidelberg bleeding classification acquired within 7 days after stroke onset (LeCouffe et al., 2021; Treurniet et al., 2021). We included 5 patients with HI1, 5 with HI2 and 5 with PH1. We did not include patients with PH2 because there were significant tissue displacements and large midline shifts (MLS) which are more difficult to simulate (and may require a non-linear constitutive model for the tissue). All 15 series of CT images were quantified by manually delineating the haemorrhage by a trained observer (KRK) using ITK-SNAP (version 3.4.0).

All CT images were imported into MATLAB R2022a to generate a pixel (2D) matrix, which was used to determine the centre of each haematoma. A coordinate was established to describe hematoma centres, as shown in Figs.4.3 and 4.4. The origin is set at the lower left of the cerebellum (left of bottom oblongata) for all patients and computational brain models. We found that it was challenging to determine the centre of the brain when there is a significant effect of MLS shown in the imaging data. Thus, setting the origin outside the brain based on the boundary of brain became our preferred choice. The centre of haematoma in the brain can thus be described in a three-dimensional co-ordinate of the form (x, y, z) where x, y and z lie in the range of $0 - 100\%$.

The determination of the haematoma location is based on the delineation of the haemorrhage. The haematoma could then be quantified in the pixel matrix. The pixels of the haematoma shown in the pixel matrix can be described as $(x_i,\ y_i,\ z_i)$. Then all the locations of haematoma pixels in three directions were used to obtain the centre of each haematoma. The flow diagram of the quantification of HT method is shown in Fig.4.3.

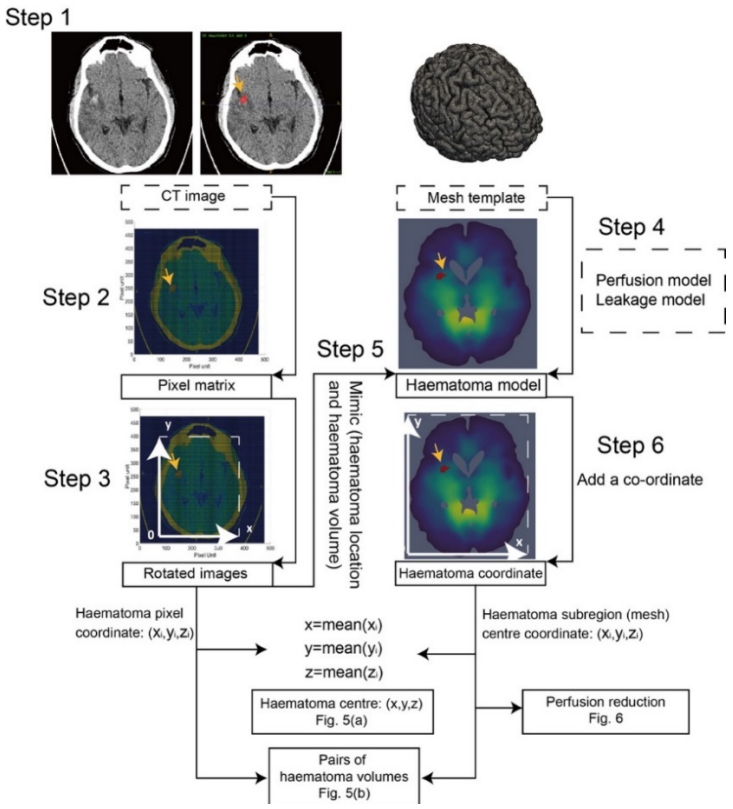

Figure 4.3: Schematic drawing of quantification method of HT for both CT images and the computational brain model. Dashed boxes: input. Yellow arrows: haematoma locations. The image was rotated after being imported into MATLAB using the function "imrotate" in MATLAB to ensure the same size (dimensions) of matrix.

4.3 Results

4.3.1 Haematoma Location and Volume Measurements

Using Eq. 4.1 - 4.7, the haematoma models can be computed for each patient with different sizes and locations of HT. An example of a HT simulation is given in Fig.4.4 for a type HI2 haematoma. The haematoma volume from CT images was calculated to be 0.72 ml and the result obtained from the simulation shows that the haematoma volume is close at 0.64 ml. The centre of haematoma obtained from the CT images is located at $(25.82\%, 60.60\%, 48.72\%)$

and that calculated from the simulation is located at $(29.48\%, 61.65\%, 47.17\%)$. As discussed above, the co-ordinates of each haematoma centre are given in percentage length (i.e., a dimensionless length) to mitigate the effects of brain geometry that may vary from one patient to another. Fig.4.5 shows the correlation of haematoma and bleeding region (note that the example shown in this figure is not the same as the example in Fig.4.4). It can be seen that the bleeding region (white) is located completely inside the haematoma (red).

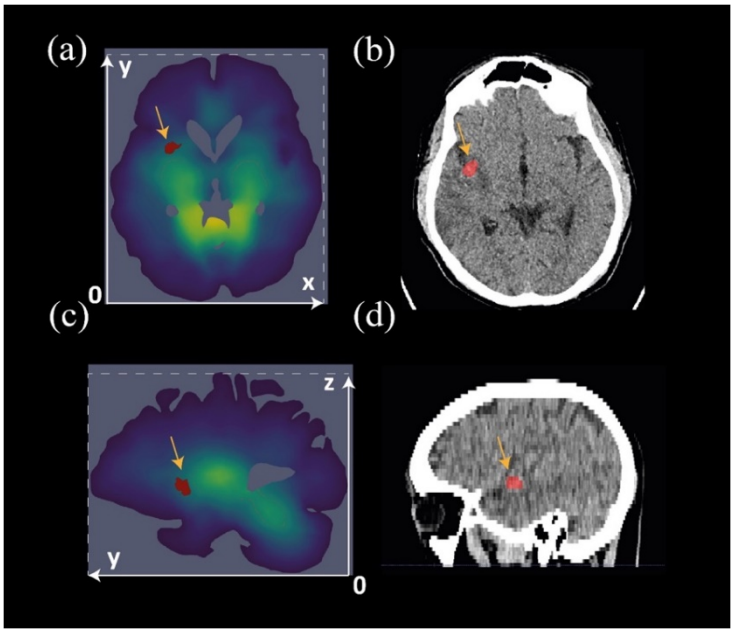

Figure 4.4: Example HT model showing a haematoma located in a full brain model obtained from the axial plane (a) and sagittal plane (c). This example is compared with an example of HT by showing the axial plane (b) and sagittal plane (d). The positive x-axis extends to the right, reaching the far-right side of the brain; the positive y-axis extends to the front, reaching the front side of the brain; and the positive z-axis extends to the top of the brain.

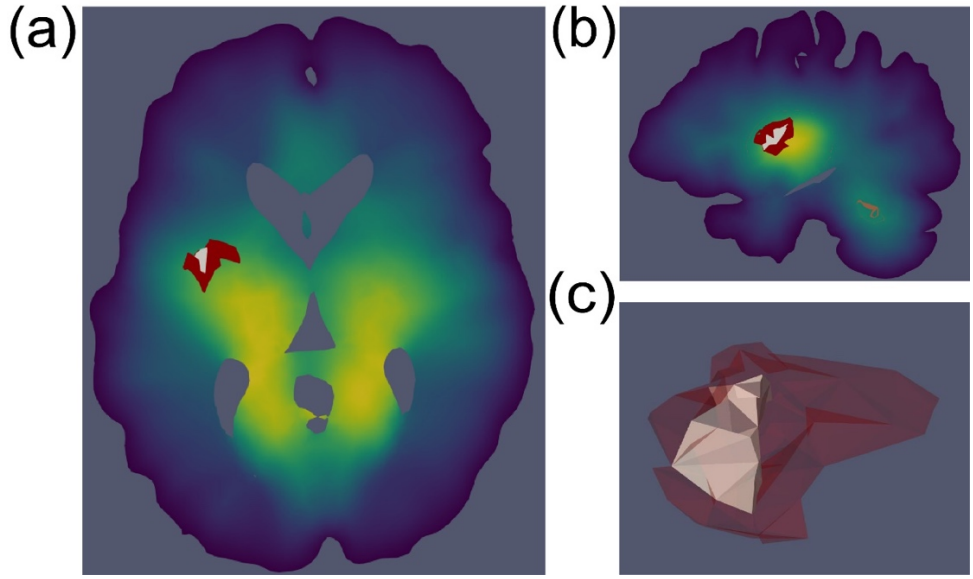

Figure 4.5: Example of haematoma and bleeding region. A haematoma (red substance) including bleeding region (white substance) from the axial plane (a). Slice view of the haematoma and bleeding region obtained from the simulation (b). The haematoma and bleeding region are shown overlaid in (c). The bleeding region is fully inside the haematoma.

These 15 HT imaging data were chosen because of their high image quality. As shown in Fig.4.6(a), 5 patients had HT in the left hemisphere (x value < 50%) and 10 patients had HT in the right hemisphere. The haematoma centres obtained from the image data and simulations are all close to each other (no significantly statistical differences are found using a t-test).

The co-ordinate differences from simulations and CT images occur because our model is limited in its location of the haematoma since the subregion size was pre-determined, i.e., the finite resolutions of both the CT images and the computational brain model leads to small differences in the haematoma centres (Józsa et al., 2021a). Comparisons of haematoma volumes (V) are also shown in Fig.4.6(b) and the p-value for the pair of volumes is > 0.05, indicating that there is again no statistically significant difference between the predicted and measured haematoma volumes.

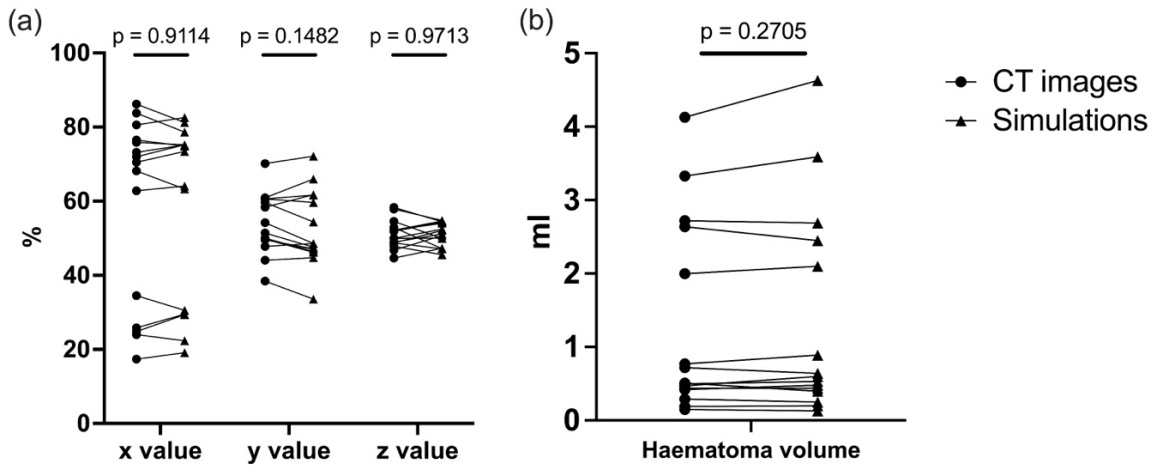

Figure 4.6: Comparison of HT between CT images and simulations. Quantification of haematoma centres in x, y and z axis (a). Comparison of haematoma volume between image data and simulations (b).

4.3.2 Perfusion Quantification

Fig.4.7 shows the comparison of perfusion reduction in the region of interest. In these simulations, we find that perfusion reduces by $5\% - 16\%$ after HT onset. The perfusion reduction (ΔF) (from the full brain model) is computed from data collected on the ipsilateral side compared with the contralateral (healthy) side. The right part of Fig.4.7 shows the perfusion reduction values computed in a penetrating network model, the values of which are taken from Wang et al. (2022a).

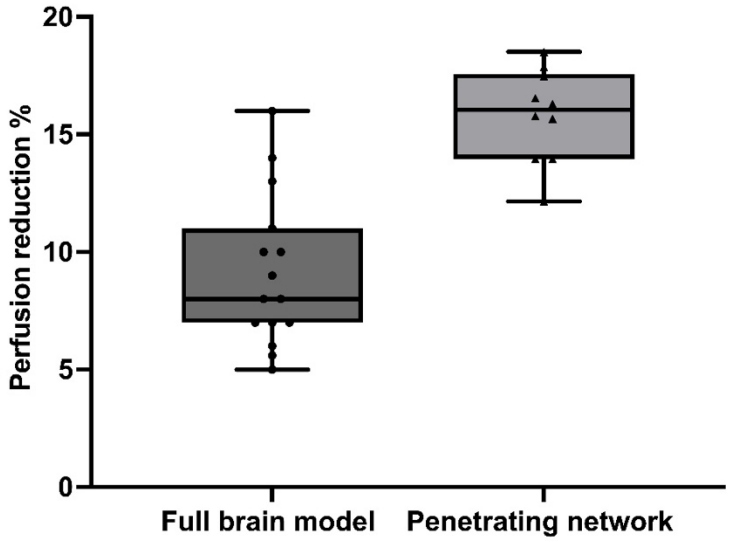

Figure 4.7: Comparison of perfusion reduction obtained from this full brain model and penetrating network model. The data for right boxplot are reproduced from Wang, et al. (2022a).

4.3.3 Sensitivity Analysis

We next used one example of HT to process the sensitivity analysis with various values of blood viscosity μ_b, the definition of haematoma surface pressure p^* and blood pressure p_a. This example of HT was set close to the lenticular nucleus, which is found to be a high occurrence location of HT (Horie et al., 2019). Correlations between haematoma volumes (V) and perfusion reduction (ΔF) with μ_b, p^* and p_a were tested, as shown in Fig.4.8. A critical phenomenon that was found when we adjusted the blood viscosity was that the haematoma volume increases with increased blood viscosity when the blood viscosity was in the range of $3.4 - 4.1$ cP. It is found that 1% increase of blood viscosity increases 10.35% of haematoma volume from the baseline (when $\mu_b = 3.6$ cP), as shown in Fig.4.8(b). In addition, we find that the perfusion reduces when the blood viscosity increases: 1% increase of blood viscosity reduces 0.04% of perfusion, Fig.4.8(b).

As shown in Fig.4.8(c), a higher definition of haematoma surface pressure leads to a larger haematoma volume and smaller perfusion reduction, as would be expected (note the logarithmic scale, which indicates the very high sensitivity). The haematoma volume changes significantly with the definition of haematoma surface pressure p^*. Haematoma volume is calculated to be 10.02 ml when we set p^* as the initial value at 1 mmHg. When the value of $p^*$is set at 5 mmHg, the haematoma volume is equal to 0.05 ml. When the value of p^* is thus set to be just 5 times larger than its original value, the haematoma volume will decrease by some four orders of magnitude. As shown in Fig.4.8(d), 1% change of p^* ($\pm p'$) leads to 0.0061% change of perfusion.

Higher blood pressure, as expected, results in larger perfusion reduction and haematoma volume. As shown in Fig.4.8(e), when the blood pressure p_a is set from 70 mmHg to 90 mmHg, the haematoma volume grows from 0.51 ml to 1.12 ml and perfusion reduction increases from 0.28% to 22.85%. The measure of importance is shown in Fig.4.8(f): 1% increase of blood pressure reduces 0.80% of perfusion and increases 4.73% of haematoma volume from the baseline.

Higher hydraulic permeability results in larger perfusion reduction and haematoma volume, as shown in Fig.4.8(g) and Fig.4.8(h). When the permeability increased by four orders of magnitude from 10^{-12} m/(Pa·S), the perfusion reduction increased from 7.89% to 16.7% and the haematoma volume increased from 0.017ml to 0.66ml.

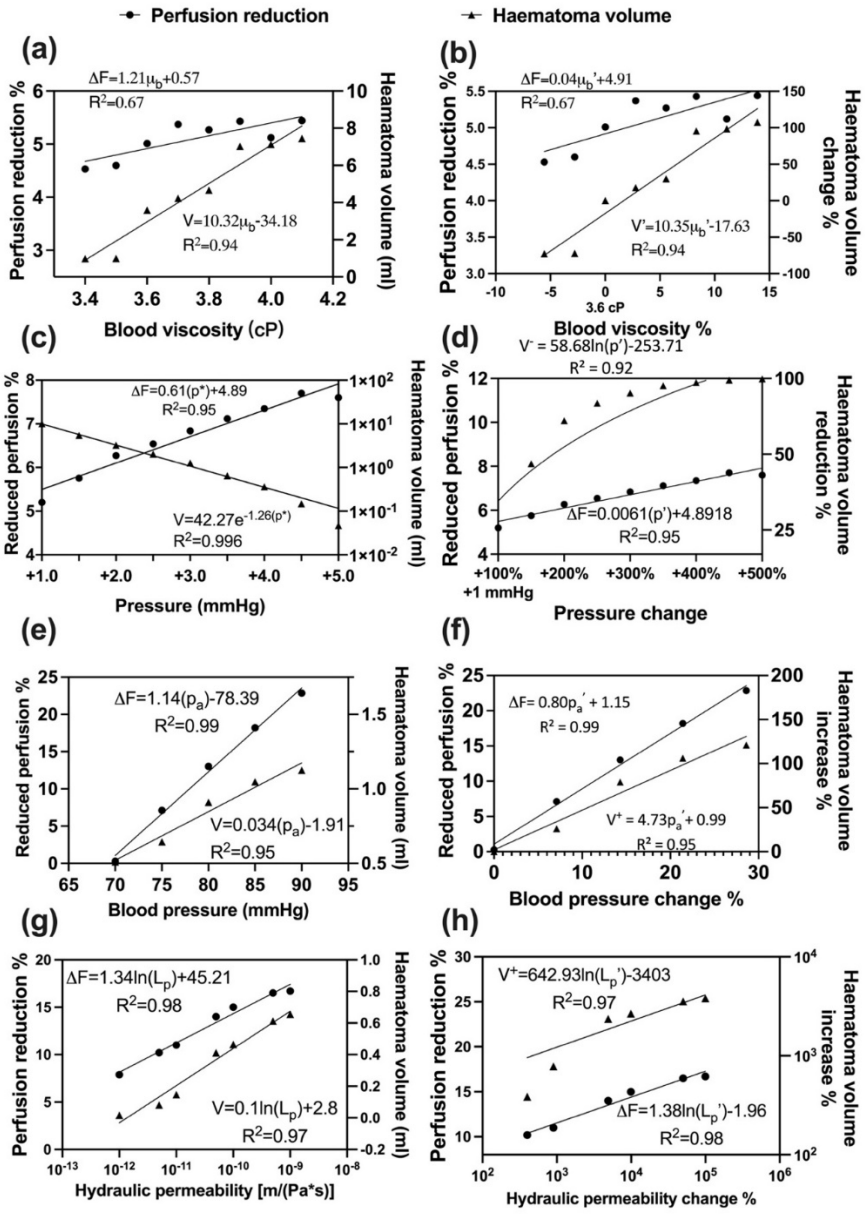

Figure 4.8: Variations in perfusion reduction and haematoma volume as functions of (a) blood viscosity, (c) the definition of haematoma surface pressure, (e) blood pressure (source pressure) and (g) hydraulic permeability. Measures of importance of perfusion reduction and haematoma volume change as functions of (b) viscosity change, (d) the definition of haematoma surface pressure change, (f) blood pressure change, (h) hydraulic permeability. ΔF denotes perfusion reduction. V denotes the haematoma volume, V' denotes the haematoma volume change. V^- denotes reduced haematoma volume and V^+ denotes increased haematoma volume. $\mu_b{}'$ denotes the blood viscosity change, p' denotes the definition of haematoma surface pressure change and $p_a{}'$ denotes the blood pressure change. Note that the right y axis in (c) is shown in logarithmic scale at a base of e.

4.4 Discussion

In this study, we have developed a model of HT in a full brain model to examine the relationship between the bleeding region with HT and to investigate how HT can be affected by various haemodynamic parameters. This simulation is based on the model proposed by Wang and Payne (2021), which presents a mathematical model of HT after ischaemic stroke. They investigated how changes in vascular geometry can affect the severity of HT. To develop further these simulations, Wang, et al. (2022a) simulated the HT in a penetrating network to determine how HT can affect healthy blood vessels and tissues. In this study, we have further developed this HT model into a computational whole brain model to investigate the correlation between bleeding region and haematoma. We quantified the HT and validated the results with a set of clinical images to simulate the bleeding region of haematomas. By using the optimised parameters, we established a HT scenario to investigate the haemodynamic factors that may affect HT.

In the quantification of HT for real clinical image data, we controlled the haematoma volumes and centres by adjusting the infarcted regions and capillary pressure manually to approach the haematoma volumes and centres obtained from CT images. The coordinate points of haematoma centres both from these models and CT images are compared in Fig.4.6(a) by t-test. All p-values of x, y and z values of haematoma centres are > 0.05. Aligning the coordinate values, however, proved to be relatively difficult compared to processing the other two values. This is due to different patients having different geometries of brains; thus, the origin of the coordinate system will be slightly different comparing with the computational model, i.e., the accurate coordinate of the bottom of oblongata is challenging to determine. In addition, the resolution of the computational brain subregion also leads to some differences. This should be addressed more rigorously in the future.

The voxel-based dice similarity coefficient (DSC), which was proposed by Dice (1945), is commonly used to quantify the area overlap between the algorithm and manually segmented regions for patients with various diseases (Chai et al., 2012; Yamamoto et al., 2012; Edmund et al., 2014; Griffis et al., 2016; Zhou et al., 2020). However, DSC can only be calculated based on two images shown by pixels or voxels. In our study, the computational brain model is mesh-based, whereas the CT images are pixel-based. Thus, the overlap regions of HT from the computational brain model and CT images are difficult to determine and define. In addition, it is challenging to determine the region of interest since the geometries of patients' brains vary from one patient to another.

In this study, the location and the volume of haematoma are the primary focus. However, the shape of the haematoma is not validated with the CT images since the main aim of this study is to optimise the model parameters (for example, p^*) and to investigate the factors that may influence the severity of HT. We suggest, however, that the shape of the haematoma should be determined in the next study to locate the bleeding region more accurately. DSC (Dice, 1945) (to determine the overlap) and symmetric correspondence method (Papademetris et al., 2002) (to obtain the difference in boundaries) are potential ways to quantify the shape difference.

In the comparison of the haematoma volumes between the CT scan and the computational model, no statistically significant difference was found. The results of haematoma volumes from the simulations are close to the clinical data. From the 15 patients, 5 are HI1, 5 are HI2 and 5 are PH1. All haematoma volumes are less than 5 ml. We did not split up results into the different types since we used these imaging data to optimise our model parameters. Different types of HT provide nearly the same results, for example, the optimised p^* was found to be 3.5 mmHg for all types of HT. We did not include the PH2 patients at this stage since this model is not able to investigate HT with large tissue displacement, especially for patients with a significant MLS.

As shown in Fig.4.7, a reduction in perfusion is found following HT, in the range of $5-16\%$. Jain, et al. (2013) compared the CT perfusion parameters for a control group and an HT group: the mean reduction rate of relative cerebral blood flow (rCBF) was found to be $10 \pm 4.3\%$ $(5.7-14.3\%)$, which is in good agreement with the results that we present here (note this experimental result of rCBF is not obtained from MR CLEAN-NO IV). Since rCBF was calculated clinically from data collected on the ipsilateral side compared with the contralateral (healthy) side, we used the same method to determine the reduction of perfusion in these simulations (noting that the comparison is not exact).

Wang et al. (2022a) predicted that the reduction of perfusion in a penetrating network voxel, which is in the size of $1 \times 1 \times 2.5$ mm, is approximately $13-17\%$ after HT onset. Our results are found to be smaller than the perfusion reduction from the penetrating network. We suggest that this is because different sizes of regions of interest are selected.

In this study, our results show that increased blood viscosity has the potential to increase the volumes of haematoma. Çinar, et al. (2001) measured the correlations between blood glucose with blood viscosity: when the mean value of blood glucose increased from $100-400$ mg/dL, viscosity increased by 25% $(r = 0.59, P = 0.002)$. Mushtaq, et al. (2019) also found that hyperglycaemia is associated with blood viscosity. A phenomenon that increased baseline glucose levels were associated with overall symptomatic intracerebral haemorrhage (sICH) occurrence was proposed by van der Steen, et al. (2022). The simulations from our model support the hypothesis that increased blood glucose levels lead to a higher level of severity of HT if the high blood glucose level results in higher blood viscosity.

In addition, high blood glucose and high blood pressure are linked, since high levels of sugar in

blood can lead to atherosclerosis (Brown & Goldstein, 1984; Libby, 2002; Bays et al., 2005). As shown in Fig.4.8(e), higher blood pressure leads to a larger haematoma and a larger reduction in perfusion, as would be expected. Blood pressure acts as a driving force of HT in our model. Our results thus also support the results proposed by van der Steen, et al. (2022): i.e., that increased baseline systolic blood pressures can increase overall sICH occurrence.

It should be noted that in our simulation, the time dynamics were not included since all images were taken at the time of CT scanning. Thus, the dynamic process of haemostasis was not considered. However, one important aspect of a reduction in cerebral blood volume (CBV) caused by haemostasis should be considered in the following stages of model development due to localized vasoconstriction occurring before haemostasis starts (Armstrong & Golan, 2011). Localized vasoconstriction caused by haemostasis could also lead to significant capillary compression but here it was assumed that increased ICP was the primary source of reduced CBV. It also indicates that further studies are needed to determine the dynamic correlations between variations in perfusion reduction and haematoma volume.

To the best of our knowledge, there are very limited available experimental data that propose rigorous definitions of the haematoma boundary using physical parameters after HT onset, especially for HT in the full brain. Wang and Payne (2021) and Wang, et al. (2022a) set the definition of haematoma boundary at $0.1\ \mathrm{mmHg}$ above tissue pressure, which was found to ensure a haematoma radius close to experimental data in mice: Jenkins, et al. (1989) measured the distance between the haematoma boundary and related damaged vessels as $700\ \mu\mathrm{m}$. However, these simulations were based on a single leaky vessel and in relatively small regions of interest, compared to our full brain model.

It can be seen from Fig.4.8(c) that haematoma volume is highly sensitive to the definition of haematoma boundary pressure. Since the haematoma boundary was drawn manually from clinical imaging data, the identification of the haematoma boundary may be different from the haematoma definition based on experimental data from individual vessels in mice (Jenkins et al., 1989; Wang & Payne, 2021). To keep the size of haematoma volume to a reasonable size compared with clinical data (LeCouffe et al., 2021; Treurniet et al., 2021), we optimised the definition of haematoma surface pressure, p^*, and found this to be $3.5\ \mathrm{mmHg}$ above tissue pressure in our simulation.

Regarding the identifiability aspects of the model, nearly all the parameters that we are using here are likely to vary from one patient to another (to a greater or lesser degree). We suspect that the hydraulic permeability L_p is one of the most likely values to vary significantly from one patient to another, although obtaining experimental measurements of this parameter is highly challenging. The sensitivity analysis for the hydraulic permeability L_p is shown in Figs.4.8(g) and 4.8(h). Future work will be required to confirm the hydraulic permeability for different types and locations of HT, which will be required to predicting the severity of HT more accurately.

In addition, we have only one computational brain model with a specific shape, while the geometries of patient brains vary from one patient to another. Although the coordinate points of haematoma centres (described using percentage values) were used in our simulation to eliminate the influence of the different shapes between our brain model and real patients' brains, more adaptive brain models will be needed in the future to fit different brain shapes. One of the potential models has been proposed by Jozsa, et al. (2022): the anatomical (geometrical) fitness of the brain models was evaluated by comparing the simulated grey and white matter volumes to measurements in healthy reference subjects. Thus, various patients can be compared with every

computational brain which is adjusted to geometry. We can use the same method in future to fit our brain model with specific patient brains.

As shown in Fig.4.5, the bleeding region and haematoma are both present in the brain model. However, this model is not able to locate the specific bleeding vessels. Since the vessel geometry varies from one patient to another, it is challenging to determine the bleeding vessels. It is suggested that the bleeding regions will need to be validated in the future as and when the relevant clinical data become available.

The long-term aim of our work is to identify those patients who are most at risk of haemorrhage based on imaging data (and other non-imaging parameters) and to predict the occurrence and severity of HT. However, our model still has many limitations to predict HT. One of the potential methods to develop a prediction model is linking HT with oedema. Oedema and HT were found to be highly associated after stroke and oedema was commonly assumed as a leading factor of HT (Vemmos et al., 2004). In addition, oedema could potentially be examined and identified by a wearable ultrasound device such as that invented by Wang, et al. (2022b). Thus, HT could in future become much more predictable by applying a wearable ultrasound device combined with our model relating oedema and haematoma.

4.5 Conclusion

Through the development of a mathematical model to simulate HT in a computational brain model, validation with real clinical images is possible through the comparison between haematoma geometry, locations, and perfusion change. This study has identified that a reduction in perfusion after HT onset is in the range of $5-16\%$, which is with good agreement with

experimental data. One of the more significant results found here is that increased blood glucose level and high blood pressure lead to more severe HT, as observed clinically:

1. 1% increase in blood viscosity reduces perfusion by 0.0434% and increases haematoma volume by 10.35% from baseline.
2. 1% increase in blood pressure reduces perfusion by 0.80% and increases haematoma volume by 4.73% from baseline.

This model is the first such to be able to simulate the correlation between bleeding regions and haematoma and should be of assistance in future to assess HT for clinicians.

Author Contributions

Xi Chen: Methodology, Writing - Original Draft, Software, Data Curation.

Jiayu Wang: Methodology, Validation, Writing - Original Draft, Visualization, Conceptualization.

Dr. Katinka R. van Kranendonk: Investigation, Writing - Review & Editing.

Dr. Tamas. I. Józsa and Dr. Wahbi El-Bouri: Software, Writing - Review & Editing.

Prof. Charles B. L. M. Majoie: Supervision, Writing - Review & Editing.

Prof. Stephen J Payne: Supervision, Writing - Review & Editing.

Other authors: Investigation, Writing - Review & Editing, Data Curation.

Chapter 5

Modelling Midline Shift and Ventricle Collapse in Cerebral Oedema Following Acute Ischaemic Stroke*

Thus far, we have proposed the models for the simulation of oedema and haemorrhagic transformation. However, the models presented in Chapter 3 & 4 are limited by the fact that they do not consider the deformation of the brain. This was due to the challenge in simulating contact problem that emerges from brain deformation. As the brain deforms, the ventricle is compressed and the ventricle surface can contact and form a self-contact problem. Here, I develop a contact mechanics solver in FEniCS open-source software for the solution of brain deformation. This enables the model to simulate the relationship between ICP and MLS, which is great significance to clinical decision-making.

5.1 Introduction

Reperfusion therapy restores CBF, but it can also cause excessive fluid leakage, leading to increased

* The contents of this chapter are reproduced without change from the published version of paper on PLoS Computational Biology (Chen et al., 2024). This paper is written and conducted by Chen. Chen contributed to the FEniCS mechanics solver, data analysis and discussion of the results.

ICP and brain oedema (Fig.5.1) (Aries et al, 2012). An elevated ICP can cause symptoms such as headache, nausea, vomiting, and loss of consciousness and can be fatal when over 25 mmHg (Leinonen et al., 2018). Therefore, clinical decision-making and treatment strategies heavily depend on accurate knowledge of ICP levels and generally aim to restore the ICP level to a normal range of 5–15 mmHg (Leinonen et al., 2018). The ICP can be measured invasively in intraventricular, intraparenchymal, subdural and epidural spaces (Raboel et al., 2012). The gold standard of ICP measurement is through an intraventricular pressure probe (Nag et al., 2019), but such an invasive technique involves higher risks of brain damage and post-surgery infection (Le Roux, 2016). Therefore, multiple non-invasive ICP measurement techniques have been developed to attempt to overcome the limitations of invasive techniques (Rosenberg et al., 2011; Raboel et al., 2012; Kristiansson et al., 2013). Many studies have attempted to find a correlation between increased ICP and radiologic findings on CT/MRI images, including the appearance of the cisterns, ventricular size, degree of contusion, the magnitude of MLS, and the ventricular index (Robba et al., 2016). However, these criteria are affected by many factors and thus are not able to predict ICP precisely. (Miller et al., 2004, Kristiansson et al., 2013).

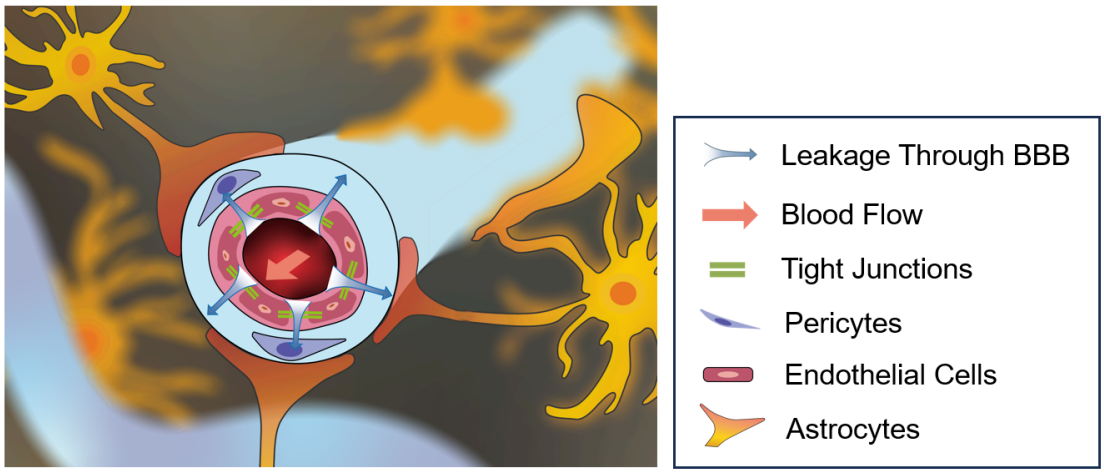

Figure 5.1: Oedema formation is associated with blood leaving the lumen through the damaged blood brain barrier, filling the interstitial space.

In this study, I focus on the MLS of the oedematous brain, which is defined as the shift of the brain past its centre line. It has been widely used to estimate ICP and the severity of brain damage since MLS can be observed directly on brain imaging. Meanwhile, MLS is also an important diagnostic (Liao et al., 2018, Tu et al., 2012) and prognostic (Asil et al., 2003) indicator in various brain diseases because it provides important information about the location and severity of brain injury (Walberer et al., 2007; Jacobs et al., 2011; Ouyang et al., 2013). Usually, a midline shift of less than 5 mm may be considered mild and may not require immediate intervention, while a midline shift of more than 5 mm may be considered moderate to severe and may require urgent surgical intervention to relieve the pressure (Valadka et al., 2000). Although previous studies have shown a linear relationship between ICP and MLS, this relationship still lacks statistical significance (Miller et al., 2004).

Over the past few decades, computational models have been widely applied to study brain oedema caused by various diseases (Drake et al., 1996; Li et al, 2009; Sweetman et al., 2011; Tully & Ventikos, 2011; Yuan et al., 2013; Mokhtarudin & Payne, 2015; Guo et al., 2018; Vardakis et al., 2019; Ju et al., 2020; Józsa et al., 2021a; Miller et al., 2021; Józsa et al., 2022) and only a few studies have focused on the simulation of post-stroke oedema (Mokhtarudin & Payne, 2015; Bing et al., 2020). Most of the previous studies focused on the solid mechanics of the brain tissue and are therefore not able to represent the variation of ICP across the computation domain and reflect the relationship between ICP and MLS (Fletcher et al., 2016; Weickenmeier et al., 2017; Bing et al., 2020). In addition, previous studies have only investigated small deformation and are thus not able to simulate large deformations of the brain and values of MLS of over 5 mm (Bing et al., 2020).

To provide more insights into the ICP-MLS relationship, I thus propose a new computational model to study the relationship between ICP and MLS and explore the factors that could cause deviations

from a linear relation. The model has been utilised for the simulation of brain osmotherapy and haemorrhagic transformation after stroke and validated with clinical data (Chen, et al., 2022; Chen et al., 2023). The present study sets out to extend computational brain models developed in the In Silico Clinical Trials for the Treatment of Acute Ischaemic Stroke (INSIST) project (Mokhtarudin & Pyane, 2015; Konduri et al., 2020; Józsa et al., 2021a; Miller et al., 2021) and to investigate factors such as patient brain geometries, the severity of BBB damage and types of oedemas that can affect the ICP-MLS relation. Once a reliable model is established, it will help to sharpen the focus of resource-intensive clinical studies, and thus lower the associated (often very high) costs. Inspired by recent studies (Mokhtarudin & Payne, 2015; Józsa et al., 2021a; Józsa et al., 2022)) on biofluid transport in the brain, a multi-compartment porous Finite Element model will be utilised to investigate the ICP-MLS relation.

In this study, I thus used poroelastic theory to model brain oedema and ventricle collapse and to investigate the relation between ICP and MLS. The computational model incorporates a contact mechanics solver for the first time to investigate severe brain oedema with large deformations and ventricle collapse. The study consists of the following parts: (1) the governing equations will be presented and the simulated arterial blood pressure (ABP), ICP and MLS will be compared with clinical data to validate the model; (2) the simulation results will be presented to show the distribution of ICP, displacement, stress and stretch in the oedematous brain; (3) oedema in patient-specific brain geometries, oedema with various severity of BBB damage and different types of oedema will be investigated to show their effects on the ICP-MLS relationship; (4) the ICP-MLS relations of different cases will be compared and the important factors will be highlighted to improve the clinical estimation of ICP; (5) stress and tenson/compression that can lead to brain tissue damage will be discussed.

5.2 Methods

The modelling pipeline consists of a perfusion component and an oedema component for the simulation of healthy blood perfusion, stroke blood perfusion, and oedema, respectively. The healthy and stroke blood perfusion simulated in the perfusion model is utilized to obtain the oedema core, which will then be imported into the oedema model for oedema simulation. The models are presented before being coupled together. Similarly, we use the perfusion model in Chapter 3 to generate perfusion data and obtain the oedema geometry.

5.2.1 Oedema model

5.2.1.1 Governing Equations

Because of the relatively slow rate of ISF flow compared to blood flow, the flow exchange between the capillary network and the interstitial space is negligible in a healthy brain. Therefore, only three compartments are used in the perfusion model. In the oedema model, however, the brain is damaged and additional fluid leaks into the interstitial space and leads to brain oedema. Therefore, additional compartments for interstitial fluid and brain deformation are required for the simulation of ICP and MLS in a damaged brain. In the oedema model, the brain is assumed to be a poroelastic medium consisting of five compartments, i.e., tissue, interstitial space, arteriole, capillary, and venule network and can thus be considered as a multi-network fluid dynamic system. A threshold of 70% or greater reduction in blood perfusion (Campbell et al., 2015; Payne, 2016; Jovin et al., 2017) is used to define the location of leaking vessels. The corresponding governing equations are given as:

$$c_w \frac{\partial p_w}{\partial t} = \nabla \cdot (K_w \nabla p_w) + S_{cw}, \tag{5.1}$$

$$c_b \frac{\partial p_a}{\partial t} = \nabla \cdot (\boldsymbol{K_a} \nabla p_a) - \omega_{ac} \cdot (p_a - p_c)\,, \tag{5.2}$$

$$c_b \frac{\partial p_c}{\partial t} = \nabla \cdot (K_c \nabla p_c) + \omega_{ac} \cdot (p_a - p_c) - \omega_{cv} \cdot (p_c - p_v) \; - \; S_{cw} \;\;, \tag{5.3}$$

$$c_b \frac{\partial p_v}{\partial t} = \nabla \cdot (\boldsymbol{K_v} \nabla p_v) + \omega_{cv} \cdot (p_c - p_v) \;\;, \tag{5.4}$$

$$G\nabla^2 \vec{\boldsymbol{u}} \;\; + (G + \; \lambda)\nabla \varepsilon \; = \; \nabla p_w, \tag{5.5}$$

where c_w and c_b are the storage factors of the interstitial fluid and blood in the brain tissue. The parameters p_w and K_w are the pressure and hydraulic conductivity of interstitial fluid in the interstitial space. ε is the dilatational strain and $\vec{\boldsymbol{u}}$ is the displacement. G and λ are the Lamé constants. The term S_{cw} represents the fluid transport from the vasculature into the interstitial space. It should be noted that here we neglected the time derivative of displacement in the poroelastic theory (Equation5.1) (Tully & Ventikos, 2011), and the poroelastic problem can thus be solved in a decoupled manner. This is because brain oedema develops over a long time scale and the process is highly dependent on the breakdown of the BBB. This makes the pressure a slow time scale (days or weeks) (Marmarou et al., 2000; Lang et al., 2017) variant whilst the deformation is at a much faster time scale (seconds or minutes) (Budday et al., 2020). In oedema modelling, time-scale separation can be used and the displacement can always reach equilibrium. Therefore, the time derivative of displacement term becomes negligible.

The value of the S_{cw} term in the normal BBB has been estimated by Fraser et al. (1990) and this value can increase by more than 100 times the normal value (Hakamata et al., 1995). Due to the large difference between the BBB permeability in the damaged region and the healthy region, the flow from capillary blood to the interstitial space and the flow of interstitial fluid in healthy tissue is thus neglected. Meanwhile, the leakage of fluid into the interstitial space S_{cw} can be derived (Mokhtarudin, 2016) from modified Starling's principle and Donnan's Effect (Donnan, 1924; Elkin et al., 2010; Lang et al., 2014):

$$S_{cw} = \begin{cases} 2n_b \frac{L_p}{R_c}[(p_c - p_w) - \sigma \Pi_c]\,, Oedema \\ \square \\ 0\,, Healthy\ tissue \end{cases} \tag{5.6}$$

The term representing fluid transfer between the capillary and the interstitial fluid compartments (S_{cw}) is derived in Appendix A. L_p is the hydraulic permeability of the capillary wall, Π_c is the osmotic pressure for the plasma components in the blood before osmotherapy, σ is the reflection coefficient of the original plasma composition, n_b is the volume fraction of blood vessels in a unit volume of brain tissue, and R_c is the mean vessel radius.

5.2.1.2 Boundary Conditions

In the oedema model, the blood perfusion is restored and thus the arteriole pressure at the pial surface is constant. Therefore, the boundary conditions of the blood compartments are the same as the healthy blood perfusion listed in Table5.1. For the interstitial compartment, the CSF in the ventricle and the subarachnoid space are compliable and the pressure in the CSF space is thus considered constant. Meanwhile, brain tissue at the pial surface is fixed to the skull through interconnecting structures such as the dura mater and subarachnoid space. Thus, the displacement at the pial surface is assumed to be negligible and a fixed boundary condition is thus imposed. As to the ventricle surface, however, the CSF in the ventricle does not resist any displacement and the stress on the ventricle surface is thus balanced by the CSF pressure in the ventricle. Therefore, the total stress $\boldsymbol{\sigma}_{total}$ satisfies $\boldsymbol{\sigma}_{total} \cdot \vec{\boldsymbol{n}} = 0$.

	Cortical Surface	**Ventricle Surface**
Arteriole Blood	$p_a = 90$ mmHg	$K_a \nabla p_a \cdot \vec{\boldsymbol{n}} = 0$
Capillary Blood	$K_c \nabla p_c \cdot \vec{\boldsymbol{n}} = 0$	$K_c \nabla p_c \cdot \vec{\boldsymbol{n}} = 0$
Venule Blood	$p_v = 15$ mmHg	$K_v \nabla p_v \cdot \vec{\boldsymbol{n}} = 0$
Interstitial Space	$p_w = 10$ mmHg	$p_w = 10$ mmHg
Tissue	$\vec{\boldsymbol{u}} = 0$	$\boldsymbol{\sigma}_{total} \cdot \vec{\boldsymbol{n}} = 0$

Table 5.1: Boundary conditions for the oedema model

5.2.2 Parameters

The parameter values used here have been presented in my previous studies and were also thoroughly investigated in previous studies by other authors. The parameter values utilised in the modelling presented here are listed in Table5.2.

Parameter	Value	Reference(s)	Parameter	Value	Reference(s)
c_b	1.59×10^{-3} Pa^{-1}	(Su, 2011)	p_v at cortical surface	2000 Pa = 15 mmHg	(Józsa et al, 2021a)
c_w	3.08×10^{-4} Pa^{-1}	Derived from (Bai, 1993; Zienkiewicz et al., 1990; Zienkiewicz et al., 1984)	R_c	5×10^{-6} m	(Cassot et al., 2006)
G	592.7 Pa	(Budday et al., 2020)	σ	0.35	Estimated from the initial ICP in oedema at the start of treatment
K_a	1.234 $mm^3s\ kg^{-1}$	Estimated by 0-order arteriole diameters and vessel density (Józsa et al, 2021a)	p_a at cortical surface	12000 Pa = 90 mmHg	(Józsa et al, 2021a)
K_c	4.28×10^{-3} $mm^3s\ kg^{-1}$	(1.0×10^{-15} m^2, El-Bouri et al, 2016)(1.0×10^{-10} m^2, Tully & Ventikos, 2011)	Π_c	2445 Pa	(Su, 2011)
K_v	2.468 $mm^3s\ kg^{-1}$	Estimated by pressure and blood perfusion rate (Józsa et al, 2021a)	ω_{ac}	3×10^{-6} $Pa^{-1}s^{-1}$	Derived from perfusion in grey and white matter (Józsa et al, 2021a, b)
K_w	3.6×10^{-3} $mm^3s\ kg^{-1}$	(Su, 2011)	ω_{cv}	6×10^{-6} $Pa^{-1}s^{-1}$	
L_p	3.0×10^{-11} m/s.Pa	(Su, 2011)	λ	1383.0 Pa	Derived. (Mokhtarudin, 2016)
n_b	0.03	(Ito et al., 2001)			

Table 5.2: Values of model parameters used in the perfusion, oedema and osmotherapy models and their sources.

5.2.3 Numerical Method

The governing equations are solved numerically using Python with a high-performance open-source finite element library, FEniCS (Logg & Wells, 2010; Logg et al., 2012). The highly coupled equations in the Finite Element model are solved in a mixed function space describing the multi-compartment dynamic system. The contact problem is solved using FEniCS, with a self-developed Augmented Lagrangian method to solve the self-contact of the brain ventricle during oedema. The method has been widely used for simulation in previous investigations of biomechanical problems (Brinkhues et al., 2013; Guo et al., 2014). The equations implemented to solve the contact mechanics are:

$$G(\boldsymbol{u}, \boldsymbol{v}) + \int_{\Gamma} (\lambda_N^{(k)} + \varepsilon_N g)\boldsymbol{v} \cdot \boldsymbol{n} \cdot d\,\Gamma \tag{5.7}$$

$$\lambda_N^{(k+1)} = \langle \lambda_N^{(k)} + \varepsilon_N g \rangle \tag{5.8}$$

where $\langle \cdot \rangle$ is the Macaulay bracket, g is the penetration depth after brain deformation, $\boldsymbol{n}$ is the contact surface normal vector. $\boldsymbol{u}$ and $\boldsymbol{v}$ denote the displacement and the variation of displacement, respectively. $G(\boldsymbol{u}, \boldsymbol{v})$ is the potential energy of non-contact terms. λ_N is the Lagrange multiplier and ε_N is the penalty coefficient and they are used to impose a contact pressure on the contact boundary to achieve convergence and to avoid large penetration. A large penalty coefficient can lead to divergence, whereas a small penalty makes it time-consuming to achieve convergence. Therefore, different penalty coefficients are chosen for different simulation cases.

The iterations and simulation algorithms are shown in the flowchart depicted in Fig.5.2. The time steps are discretized using a backward Euler scheme throughout the model. The pressure field is first computed and then utilized to compute the displacement. The rise in ICP leads to tissue deformation and thus potential contact between ventricle surfaces. The collision between mesh elements is detected using BoundingBoxTree toolset in FEniCS after each iteration and the penetration depth of each

penetrating mesh nodes is measured to obtain g and to generate the $\lambda_N^{\square}$ function. We use SciPy and PETSc toolkits to assemble and solve stiffness matrices and residual forces generated from FEniCS. As the ventricle collapses, the surface of the ventricle contacts and the Lagrange multiplier is augmented to avoid large penetration of brain tissue. Once the Lagrange multiplier is found to keep penetration within tolerance, the results are saved and used for the simulation in the next time step. Details of the implementation of the contact algorithm and convergence criteria are introduced in Appendix D.

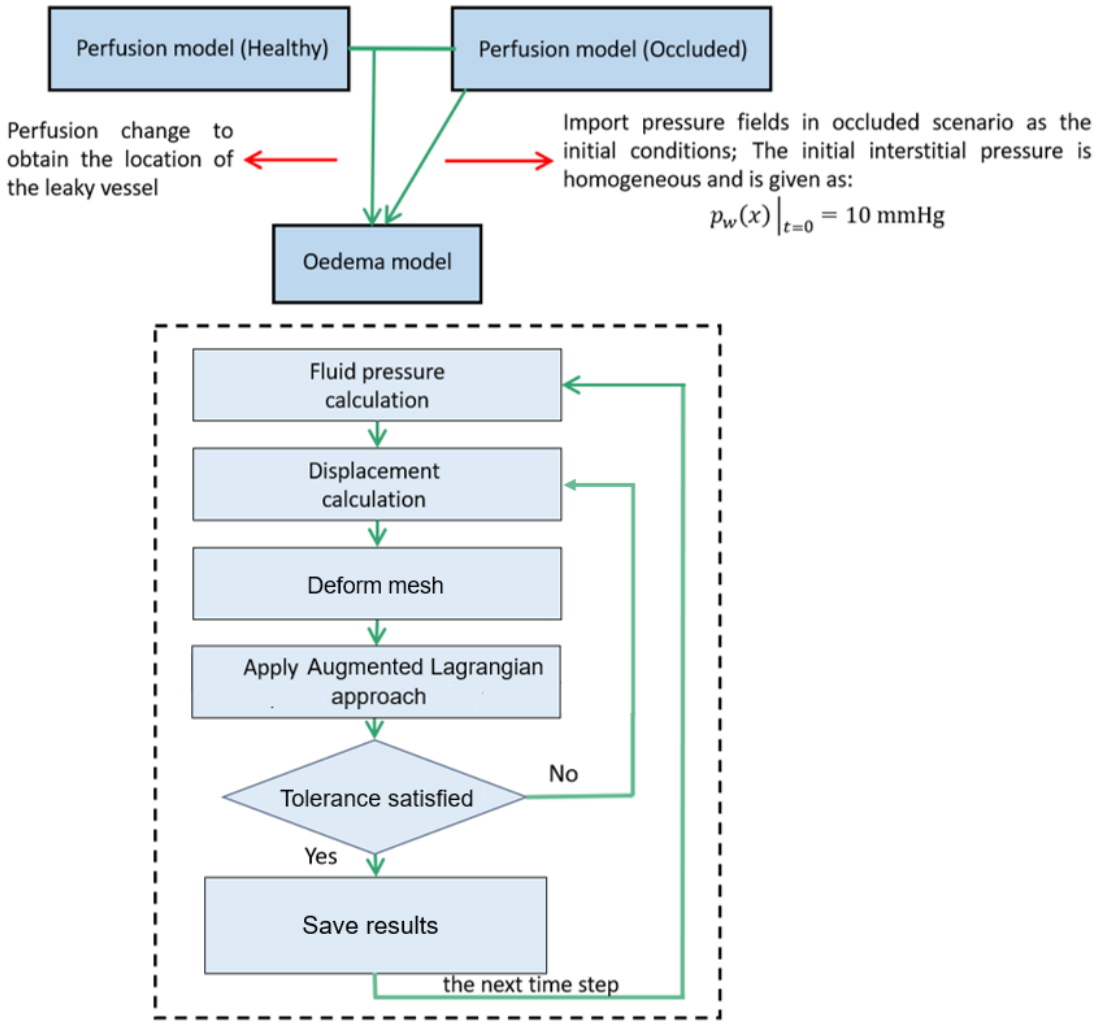

Figure 5.2: Flowchart of the computation algorithm for mesh deformation.

The pressure in each compartment (p_i) is discretised with piecewise linear Lagrange (P1) elements. Meanwhile, the permeabilities (K_i) and the other coefficients (ω_{ij}, L_p, etc) used in the model are represented in piecewise constant (dP0) tensor and scalar function spaces, respectively. The pressure field computed from the previous step is then used for the simulation of the displacement field, where the displacement is discretised with the Continuous Galerkin (CG) Method. The flow fields, the blood perfusion and the displacement are all computed in P1 elements and are solved using the BiCojungate Gradient STABilised method (BiCGSTAB) with an Algebraic MultiGrid (AMG) preconditioner.

5.2.4 Clinical Data

The dataset used here is obtained from a retrospective cohort of 97 oedema patients who had traumatic brain injury (TBI) and were admitted to the Neurosciences Critical Care Unit between 1995-2002 in Addenbrooke's Hospital, University of Cambridge, UK. Data were recorded and re-analysed anonymously under ethical protocol 30 REC 97/291. The median age was 34 years (range 13-76 years; 78% males). ABP was measured directly from the radial artery levelled at the level of the heart (Baxter Health Care Corp.). ICP was monitored continuously using a microtransducer (Direct Pressure Monitor; Camino Laboratories, or MicroSensors ICP Transducer; Codman and Shurtleff, Inc.), inserted intraparenchymally into the right frontal region. Among them, 24 presented unilateral lesions and midline shifts were confirmed by CT imaging (Cardim et al., 2021). The midline shift was measured in millimetres according to the scale on the CT scan. We assigned a positive value to the displacement of the midline from the right to the left side, and a negative value to displacement of the midline from the left to the right side. No midline shift was graded as a zero value. The median number of daily recordings was 3 days (range 1–11 days).

As the post-ischaemic stroke is usually not as severe as the TBI, data on the intraparenchymal

monitoring of ICP is very rare. Therefore, the TBI data are utilised in this in-silico study to obtain proper mechanical properties, including the shear modulus and Poisson ratio of the brain tissue.

5.3 Results

Here I show the simulation results of the population-averaged brain with hemispheric stroke. The oedema volume is simulated in the perfusion model and shown in Fig.5.3a. As the brain swells during the development of oedema, the cerebrospinal fluid (CSF) drains, and the ventricle surface contacts (Fig.5.3b). The temporal variation of blood pressures, ICP and displacement can be observed. As the ICP rises, the brain swells and the capillary blood pressure drops on the swelling side. Meanwhile, there is only an insignificant change in the blood pressures in the arteriole and venule compartments (Fig 5.3c).

5.3.1 Model Validation

The simulation results are first compared with the clinical ICP, ABP and MLS data of oedema patients. In Fig.5.4, the clinical data of ICP and ABP in lesions in the left hemisphere and right hemisphere are shown separately, with the in-silico data fitting the ellipse. In the clinical data, a linear relationship between ICP and ABP shows that the ICP rise is primarily driven by blood pressure and the data points can be fitted using an ellipse and linear fit (as shown in Fig.5.4). Similarly, the governing equations in the model also indicate that the ICP rise is linearly driven by the ABP, as expected, and as shown in Equation 5.1-5.5. By varying the ABP values, ICP also varies during brain oedema and the ICP values can be recorded and compared with the clinical data to fit the ellipse. A good fit of the ABP and ICP data indicates a proper choice of the L_p to K_w ratio in the computational model and thus validates the flow simulation. In the model, ABP corresponds to the boundary blood pressure on the pial surface in the arteriole compartment and ICP corresponds to the maximum interstitial pressure across the

computation domain. MLS is measured as the maximum displacement on the centreline of the brain model. As for different ABP values ABP_i, the boundary conditions for the arteriole blood at the cortical surface are varied and the venule pressure is set to rise as the arteriole pressure rises, with a fixed pressure difference of 75 mmHg.

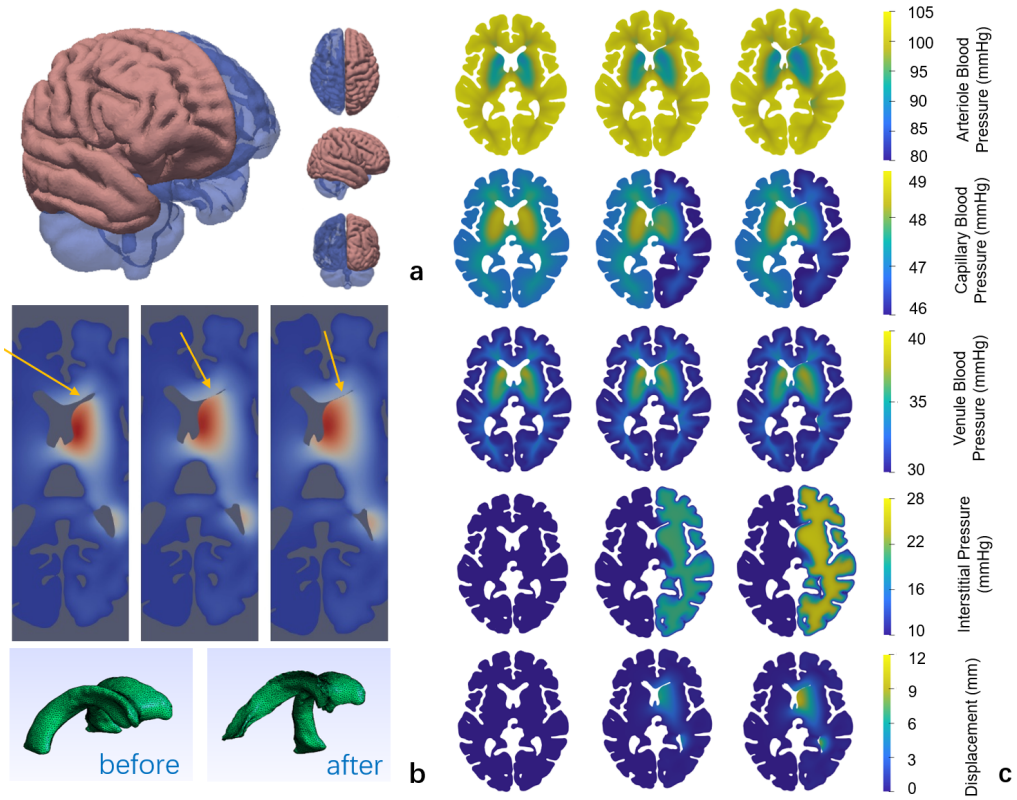

Figure 5.3: simulation results of the hemispheric oedema in the population-averaged human brain when the ABP is 105 mmHg. Here, the simulation results for 105 mmHg ABP are chosen to show the MLS and contact of ventricle surface more clearly. (a) 3D oedema geometry. (b) ventricle collapse and partial contact. (c) slices of blood pressures, ICP and displacement at 500 and 1000 seconds.

Meanwhile, I can also obtain the MLS values in the simulations for the validation of the solid compartment in the model. In the model, the relationship between ICP and MLS is determined by the

shear modulus and Poisson ratio of the solid phase. Therefore, a comparison demonstrates the accuracy of mechanical property parameters chosen in the model. In Fig.5.4b, the MLS values of the data points in Fig.5.4a are plotted against the boxplot of MLS values measured on CT imaging, and an excellent agreement is found.

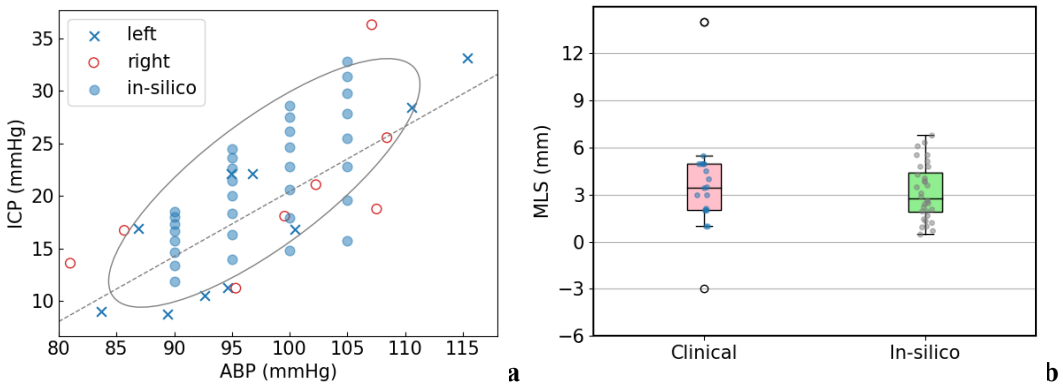

Figure 5.4: Clinical data and validation. (a) The ICP and ABP relationship with best ellipse fit and linear fit (dotted line). Clinical data for lesions on the left and right hemisphere are shown and simulations are run within the range. (b) Clinical and in-silico MLS comparison, with the boxplots showing 5, 25, 50, 75, 95 percentiles.

5.3.2 Intracranial Pressure, Midline Shift, and Stress

In brain oedema, there are multiple different types of damage, including stress damage and axonal damage caused by stretch. Therefore, in this section, I consider the distributions of ICP, displacement and tissue stress. As shown in Fig.5.5, the ABP is 105 mmHg and the maximum ICP across the computational domain is found during the development of oedema. As the intracranial pressure rises, the oedema core swells and compresses the surrounding tissue, leading to a rise in tissue stress. The ICP rises in the entire hemisphere while the deformation occurs in certain regions on the ventricle surface. ICP value can be obtained by calculating the maximum pressure from the interstitial fluid compartment in the computational domain. It can be observed that stress concentrates at the corners

of the ventricle. The periventricular stress concentration is much greater (approximately twice) than the maximum intraparenchymal stress.

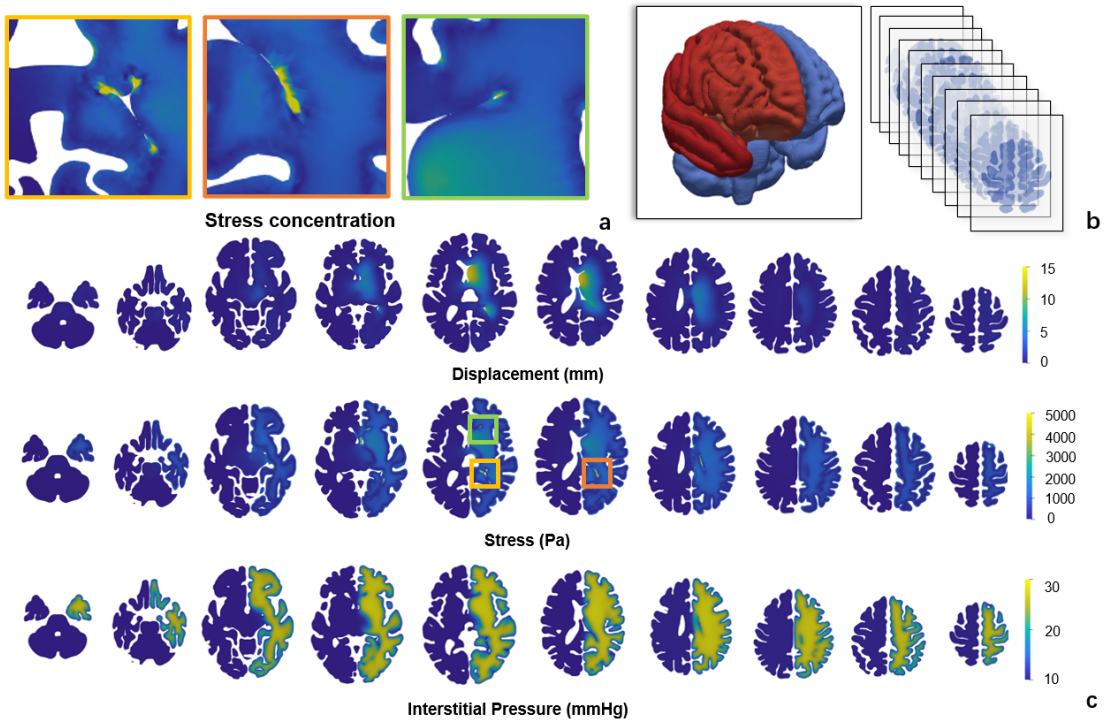

Figure 5.5: ICP, displacement and stress distribution in the brain (a) the stress concentration on the ventricle corners. (b) brain slices of the model. (c) slices showing values of ICP, displacement and stress.

5.3.3 ICP-MLS Relationship

Due to the difficulties in measuring ICP in clinical settings, the MLS has been widely used to determine the severity of oedema. However, the ICP-MLS relationship has been shown to be multi-factorial and it is thus challenging to substitute MLS for accurate ICP estimation. Hence, to study the effects of these factors, i.e., patient-specific brain geometry, BBB damage severity and types of oedemas, are simulated to obtain ICP-MLS curves and to quantify the variability that can arise.

5.3.3.1 Patient-specific Geometry

According to our previous study, the brain mesh is affine transformed according to CT imaging to

obtain brain models that are similar to patient-specific brains (Józsa et al., 2023). Quasi-patient-specific geometries are obtained by first creating a general mesh template in the standard space and then an affine registration of this template to the tissue mask of each specific subject. This approach avoids time-consuming and potentially non-robust patient-specific geometry reconstruction. A mesh template is prepared from the averaged T1-weighted MNI template of the IXI555 cohort (Gaser, 2009). Here I study oedema in patient brains with hemispheric oedema and compare the ICP-MLS curves with the population-averaged brain (Fig.5.6). Linear fits are used to find the ICP-MLS slope and zero intercept is imposed in the linear fitting as the MLS is zero when there is no pressure rise in the healthy brain. In this study, 18 cases are simulated and the four with the most different ICP-MLS curves are shown in Fig.5.6.

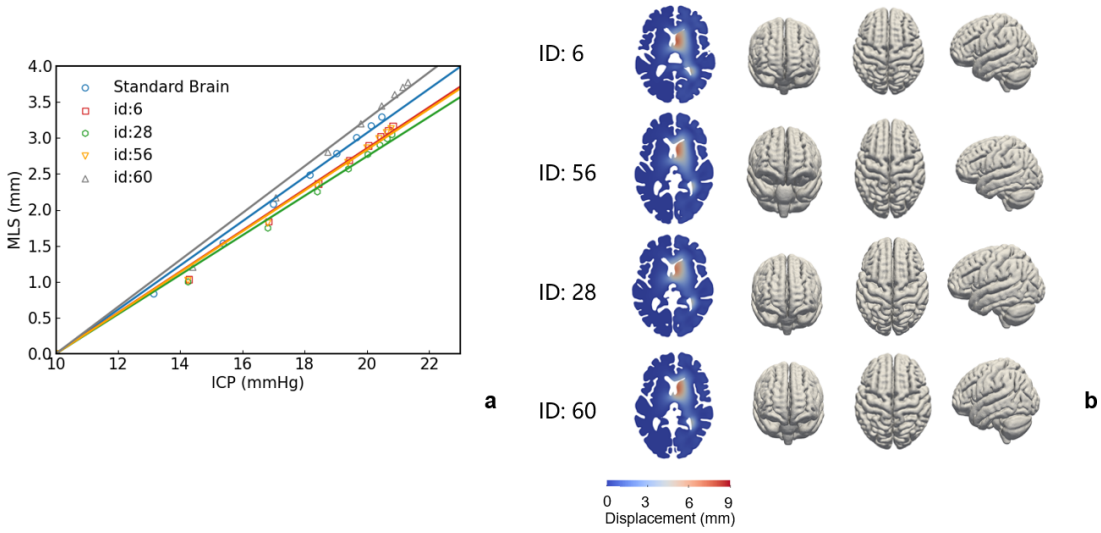

Figure 5.6: (a) MLS-ICP curves; and (b) patient-specific brain geometries obtained from affine transformation.

The oedema volumes, sagittal, coronal, and axial lengths of the patient brains are summarized in Table5.3. To illustrate the correlation between the ICP-MLS slope and geometrical features of the brain. The volume of oedema and 3 dimensions of the 18 patient-specific brains are plotted with the slopes (Fig.5.7). It can be seen that the ICP-MLS relationship is dependent upon the volume of the

oedema, with an R^2 of 0.530. Meanwhile, the plot of 3 dimensions shows the axial and coronal lengths of the patient brain correlate with the ICP-MLS slopes. In brains with larger axial and coronal lengths, the ventricle has a larger cross-section for brain tissue displacement from the right to left hemisphere and this indicates the ICP-MLS curve is affected by the geometry of the ventricle.

Patient	Volume of Oedema (ml)	Sagittal Length (cm)	Coronal Length (cm)	Axial Length (cm)
Standard Brain	55.75	13.8	17.4	15.5
6	42.62	13.0	15.7	14.6
28	45.18	12.6	16.9	14.7
56	42.42	12.7	16.2	14.8
60	59.59	14.1	17.4	17.0

Table 5.3: Oedema volumes and the maximum width and maximum length of brain geometries.

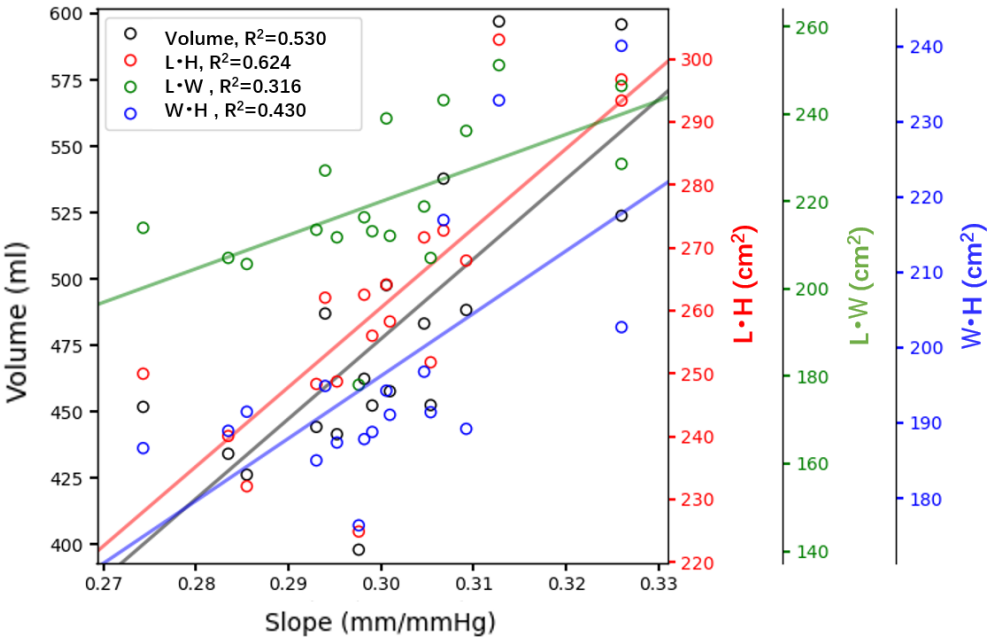

Figure 5.7: The factors that can affect the ICP-MLS relationship, where volume indicates the volume of oedema in different brains, and the L, W and H represent coronal, sagittal and axial lengths, respectively.

5.3.3.2 Severity of BBB Damage

Another factor that varies among patients is the severity of BBB damage. BBB damage depends on the effectiveness of the stroke therapy, age, medical history, collateral score, etc (Kimberly et al., 2018; Wiegers al., 2020). Due to the different extent of BBB damage, some patients present MLS whereas others do not. To investigate the effects of the severity of BBB damage, the L_p value is varied to analyse the ICP-MLS relations. As shown in Fig.5.8, the ICP rise is distributed only in the oedema core when the L_p is small and the ICP becomes more evenly distributed across the hemisphere as L_p rises. Meanwhile, the volume change in the brain tissue can be defined as:

$$\Delta V = \frac{V_c - V_i}{V_i} \times 100\% \tag{5.9}$$

where the V_c is the volume of tissue after oedema occurrence and V_i is the tissue volume before oedema. As the BBB damage becomes more severe, the volume of the brain tissue also increases across a larger region, from the core in the oedema volume to almost the entire right hemisphere (Fig.5.8c). As the tissue swells, the increase in the water content in the oedema core compresses the surrounding tissue and leads to a water content and tissue volume reduction (around 20%) at the periventricular region and at the pial surface. It is found that as L_p rises, the volume of fluid leakage into the interstitial space becomes greater and thus leads to larger MLS under the same maximum ICP rise (Fig.5.8a). However, when the increase of water content in the brain tissue almost spreads across the entire hemisphere (as shown in the $5L_p$ and $8L_p$ cases), the slope of the ICP-MLS curve stops increasing.

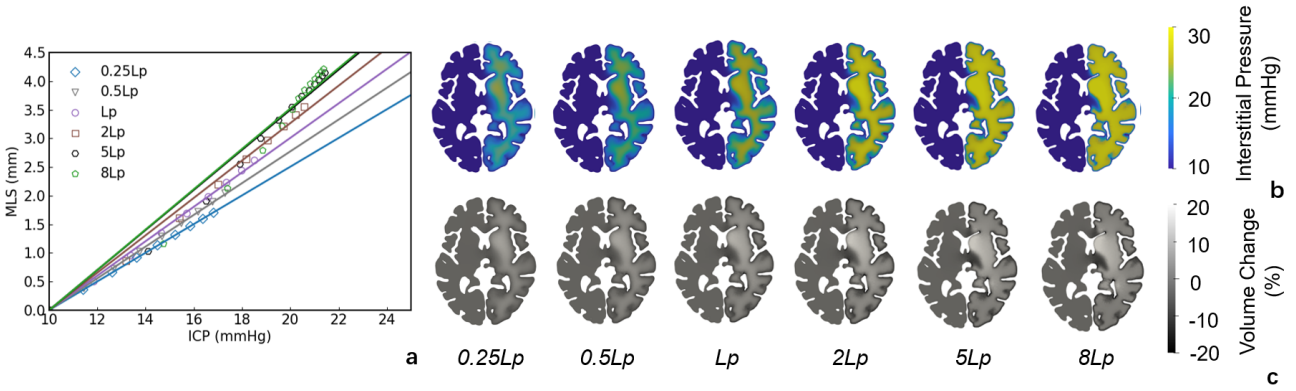

Figure 5.8: Effects of Lp value and the volume changes in the oedema brain. The value of Lp rises from left to right.

5.3.3.3 Types of Oedemas

Different types of stroke lead to different types of post-stroke oedema, including ACA, PCA, MCA, and hemispheric oedema, etc. MCA and hemispheric oedema are common types of oedema, whereas PCA and ACA are rare and are thus hard to investigate in clinical settings. In the model, oedema at different locations leads to differences in anatomical features and thus various ICP-MLS relations. According to a vascular territory atlas (Tatu et al., 1998), each artery feeds one sub-territory at the pial surface, as shown in Fig.5.9a. In this section, different territories on the pial surface are occluded in the perfusion model to obtain damaged tissue volume for a range of oedema simulations.

The volumes of oedema cores are listed in Table5.4. It can be noted that the ICP-MLS slopes of different types of oedemas vary significantly (Fig.5.9c & 5.9d). The pressure rise in the interstitial fluid compartment in different types of brain oedema is similar (Fig.5.9e). Meanwhile, the volume of the MCA oedema is twice the volume of PCA or ACA, while the volumes of PCA and ACA oedema are around the same. Although the PCA and ACA oedema are of similar volume, the MLS in ACA oedema reaches around 1 mm when ICP is 20 mmHg while the PCA oedema leads to almost no MLS. The PCA oedema, the displacement in the brain tissue concentrates at the right back of the ventricle and thus does not contribute to the MLS (Fig.5.9b & 5.9f). Meanwhile, the ACA oedema leads to

much larger MLS as the swelling tissue compresses the tissue on the opposite side even though the deformation is restricted by the falx which is assumed to be rigid. The MLS caused by ACA can be larger if the falx is included as a part of the model. In addition, tissue swelling in MCA oedema pushes the brain from the side and therefore the MLS caused by MCA oedema is the largest of the three types of oedema.

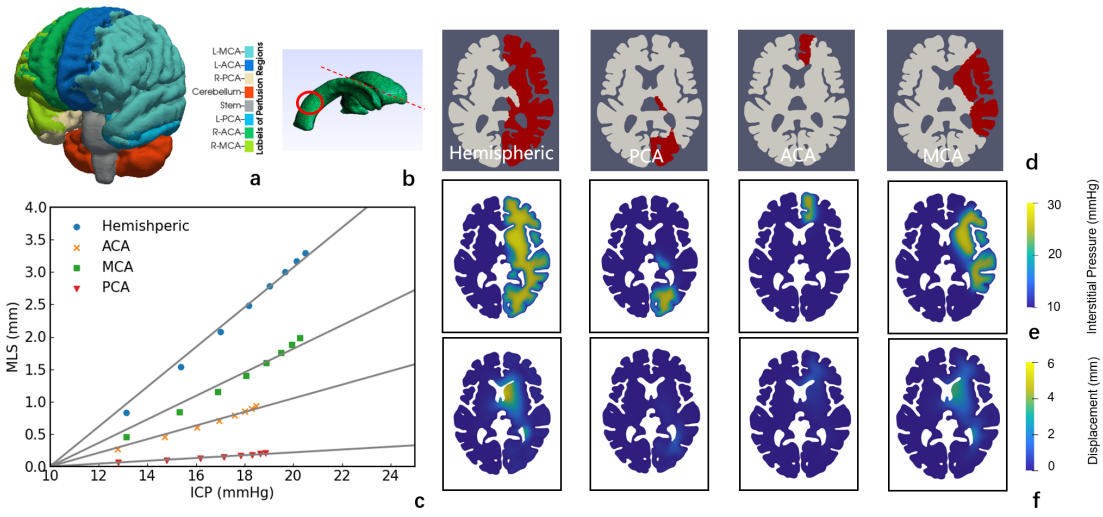

Figure 5.9: Simulations of different types of oedemas. (a) Subregions on brain model. (b) Ventricle geometry and midline of the brain. (c) MLS-ICP relations for different types of oedemas. (d) Hemispheric, PCA, ACA and MCA oedema geometries. (e) ICP rise. (f) Displacement.

Type of Oedema	Oedema Volume (ml)	Slope (mm/mmHg)
Hemispheric	53.78	0.307
PCA	7.00	0.022
ACA	8.52	0.105
MCA	16.98	0.181

Table 5.4: Volumes of different types of brain oedema.

5.4 Discussion

This chapter proposes the first model for the study of post-stroke oedema with MLS under large deformation. Although computational models have been widely used for the study of brain oedema, post-stroke oedema has not been thoroughly investigated. Different from previous studies in which the oedema cores are assumed as growing volumes (Bing et al., 2020) or are assumed to occur in the entire brain (Tully & Ventikos, 2011; Vardakis et al., 2016), a perfusion component is utilised in the model for the simulation of different types of oedemas and to obtain the oedema volume. This provides more accurate population-averaged oedema locations and allows us to investigate the differences between different oedema types in more detail. Meanwhile, the population-averaged brain can be affine transformed to obtain patient-specific brains and to analyse the effects of their anatomical features. Furthermore, as the brain is modelled as a four-compartment poroelastic medium, it can thus provide overall information on blood pressure, interstitial pressure, displacement, stress and strain. This helps improve our understanding of post-stroke brain oedema as a multi-factorial process.

This model also incorporates for the first time the contact mechanics problem into the modelling of brain oedema, Previous studies assume the ventricle as a material with low shear modulus as an approximation of the fluidity of cerebrospinal fluid (Fletcher et al., 2016; Weickenmeier et al., 2017; Bing et al., 2020). However, the compression of ventricle mesh during the tissue swelling makes it challenging to simulate brain oedema with large deformations. In previous studies, most models only focus on marginal brain deformation and the MLS is only around 2 mm, which is smaller than the clinical threshold of severe oedema (5mm). In the model proposed here, the brain ventricle can collapse and therefore allows us to investigate brain oedema with MLS over 7mm and to study severe oedema cases.

The simulation results are compared with the clinical data of 97 oedema patients for validation. The linear relationship between ABP and ICP observed in the patients is replicated in the model by varying arteriole blood pressure boundary conditions. The ICP values are chosen from different time points, ranging from 0 to 1000 s. The time taken to reach the ICP values in the clinical data are around 1000 second and this is much shorter than the time recorded (in days) in clinical settings. This is because the development of oedema is not just a fluid and solid mechanic process, and biochemical factors including oxidative stress, toxic substances and enzymes are involved in the damage of the BBB over a longer time period (Marmarou et al., 2000; Lang et al., 2017). In clinical settings, the ICP can be measured both in the ventricle and in the parenchyma. As the gold standard of ICP measurement, the pressure in the ventricle is measured through an intraventricular catheter. However, the pressure represents the CSF pressure and is thus not able to reflect the pressure in the tissue. In this study, the intraparenchymal pressure is measured using the ICP micro transducer. Two outliers are shown in the boxplot (Fig.5.4) and the clinical data (range from 1 to 5.5 mm, with a mean value of 3.6 mm) are compared to the in-silico results (range from 0.5 to 6.8, with a mean value of 3.2 mm). Although there are limited clinical data available, this analysis provides some comparison between the clinical data and our computational model and helps determine the key parameters when using a poroelastic model for oedema modelling.

The ICP-MLS relationship is the most crucial for the estimation of brain oedema severity. As shown in the results, the types of oedemas affect the linear relationship significantly (Fig.5.9) while the geometry and BBB damage severity can only lead to around 2 (Fig.5.6) and 5 (Fig.5.8) mmHg underestimation of ICP when MLS is 3.5 mm. Therefore, it is crucial to take the types of oedemas into consideration when estimating ICP from MLS. Especially, estimating ICP from MLS in PCA oedema leads to a very significant underestimation of ICP and thus should be considered in clinical studies. Furthermore, stress can restrict blood flow and lead to the rupture of blood vessels, with the

compression/tension causing mechanical damage to axons. The simulation results show that under large deformation, the periventricular and intraparenchymal regions experience reduction and increase in water content and the stress concentrates at the periventricular corners. This suggests that the periventricular regions are prone to vessel closure in oedema and therefore have a higher risk for secondary ischaemia and tissue damage. In the simulation results (as shown in Appendix C), both the ICP and MLS can predict intraparenchymal pressure well but do not predict the periventricular stress accurately. This indicates that the intraparenchymal stress is determined by the forces exerted by excessive ICP in the tissue and the stress at the ventricle corners is affected by the geometry of brain and it is therefore less predictable and more challenging to evaluate its risks.

5.4.1 Limitations

It should be noted that there are several limitations to this study. Firstly, many parameters have been used in the multicompartment model. Some of them are challenging to measure in clinical settings or experiments. For example, the fluid filtration of the capillary wall has been measured in frog models (Fraser et al., 1990) but there is still a lack of data on the L_p values in the human brain (Harper & Bohlen, 1984; Józsa et al., 2021a). Meanwhile, some parameters such as the Poisson ratio and shear modulus of the brain tissue remain controversial. The values of the mechanical property parameters are affected by tissue sampling and experimental techniques and thus vary dramatically in previous literature.

Secondly, due to the danger and high risk of intraparenchymal pressure measurement, the data on ICP are very limited. In this study, I use the data from 97 patients whose oedema was caused by traumatic brain injury (TBI) for the validation of the model. Although both TBI and post-stroke oedema are caused by BBB damage, the TBI oedema takes longer to develop, whereas post-stroke oedema can occur in hours or days and the difference between the mechanisms is still unclear. Thirdly, the deformation of the brain can be more complicated because of the realistic boundary conditions. In the

model, the pial surface of the brain imposes a zero-displacement boundary condition and the falx is not included in the model and is thus considered non-deformable. However, the falx is not rigid and can deform when compressed by surrounding tissue. Furthermore, the gyrus and sulcus between the brain tissue and skull can also allow some deformation and thus affect the displacement field and the MLS values.

Finally, linear elasticity is utilised for the simulation of large deformation the brain tissue can show complex mechanical behaviours under different types of loads (Budday et al., 2020), and it can thus be challenging to describe the mechanical properties of the brain tissue in oedema, especially when the brain tissue experiences compression, tension and shear at the same time. Considering that the Fung hyper-elastic model and linear elastic model did not show significant difference when the dilatational strain is below 25% (Mokhtarudin, 2016). For simplicity, linear elasticity is employed throughout the study. However, as this study majorly focus on the impact of various physiological features, such the oedema type, brain geometry and BBB damage levels, the major conclusion of this study is not expected to be affected by the choice of constitutive law.

In conclusion, this is the first model studying brain swelling and ventricle collapse in brain oedema. The simulation results are found to be in good agreement with the clinical data of 97 patients. Stress, water content, interstitial pressure, blood pressure, compression/tension and MLS of the oedema brain are presented and the stress concentration in the periventricular region is highlighted. Furthermore, various factors (patient brain geometry, BBB damage severity and oedema types) that can affect the estimation of ICP from MLS are investigated to assist clinical decision-making. This model can hopefully be further developed to achieve better accuracy and to provide more detailed guidelines for the clinical treatment of oedema.

Author Contributions

Conceptualization: Xi Chen.

Data curation: Xi Chen, Danilo Cardim, Chiara Robba, Marek Czosnyka.

Formal analysis: Xi Chen.

Funding acquisition: Tama´s I. Jozsa, Stephen J. Payne.

Investigation: Xi Chen.

Methodology: Xi Chen, Tamas I. Jozsa.

Project administration: Stephen J. Payne.

Resources: Stephen J. Payne.

Software: Xi Chen.

Supervision: Stephen J. Payne.

Validation: Xi Chen.

Visualization: Xi Chen.

Writing– original draft: Xi Chen.

Chapter 6

AI-assisted In-silico Trial for the Optimization of Osmotherapy*

In this Chapter, we attempt to address the problem discussed in Chapter 3 with a deep neural network Computational models are usually limited by the fact that the model parameters are not patient specific. As a result, the optimisation of osmotherapy can be challenging due to the variation of physiological parameter in patient groups. In contrast, deep neural network can incorporate biostatistical information and therefore help tackling the challenges in in-silico trials. Here, a deep neural network is trained and tested with in-silico data to optimise the dose of osmotic agent in patient groups of various BBB damage levels and ages. In this Chapter, the contents in the thesis is further enriched by incorporating deep learning techniques.

* The contents of this chapter are reproduced without change from the version currently under review. This Chapter is the collaborative work of Xi Chen and Lei Lu. Chen worked on the brain modelling, data generation and data analysis. The simulations are run for 3000 cases and used for training and testing of neural network. Chen and Lu both contributed to the conceptualisation of the paper and modelling of the deep neural networks. Xi Chen designed Multiple Layer Perceptron and Convolutional Neural Network and Lei Lu improved its performance by designing an architecture with ResNet blocks. Xi Chen finished the paper manuscript with Lei Lu's assistance on the neural network part of the manuscript (section 6.2.1 & 6.3.1).

6.1 Introduction

In the context of an ischemic stroke, blood vessel blockage causes a reduction in cerebral blood flow (CBF) and the blood-brain barrier (BBB) breakdown, resulting in a rise in BBB permeability (Yang & Rosenburg, 2011; Lee et al., 2017). Reperfusion therapy aims at restoring CBF to the affected area and can thus elevate blood pressure and lead to excessive fluid leakage into the interstitial space (see Fig.6.1). Consequently, this fluid accumulation in the interstitial space can result in brain oedema, increasing intracranial pressure (ICP), and excessive brain tissue stress (Donkin et al., 2010). Elevated ICP leads to symptoms like headache, nausea, vomiting, and loss of consciousness. Typically, an ICP exceeding 25 mmHg is deemed life-threatening and necessitates immediate medical intervention (Leinonen et al., 2018). Over the past few decades, osmotherapy has been widely employed to restore ICP to the normal range of 5 to 15 mmHg (Ayata & Ropper, 2004; Leinonen et al., 2018)

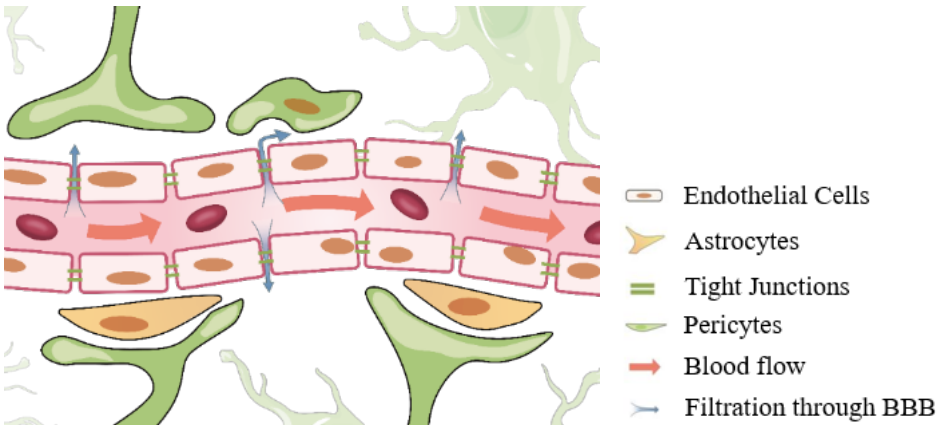

Figure 6.1: Fluid filtration from the lumen to the interstitial space through the blood brain barrier (BBB) of a single capillary vessel.

Currently, four types of osmotic agents (mannitol, hypertonic saline, sorbitol, and glycerol) are available for treatment and hypertonic saline has gained increasing popularity (Larive et al., 2004; Ziai et al., 2007; Hays et al., 2011). Hypertonic saline creates an osmotic pressure gradient that drives

excessive fluid from the brain into the intravascular space, thereby reducing the volume of interstitial fluid and relieving oedema. Despite its various advantages, the use of osmotic agents can result in a variety of issues (Paczynski, 1997; Grände & Romner, 2012). One concern is that the elevation in Cl^- level in hypertonic saline can lead to hyperchloremic acidosis (Kølsen-Petersen, 2020). Additionally, a high concentration of NaCl (exceeding 160 mmol/L) is reported to worsen outcomes and further damage the blood-brain barrier (Himmelseher, 2007; Qureshi & Suarez, 2000). Hence, it is crucial to carefully select the administration protocol. In clinical practice, despite there are previous comparisons of osmotherapy outcomes (Tyagi et al., 2007; Carney et al., 2017; Mangat, 2018; Gu et al., 2019), no optimized administration protocol established for hypertonic saline infusion. The variation in the proposed protocols in previous studies are inferred to be a result of heterogeneity in the patients (Kølsen-Petersen, 2020).

To tackle this issue, the current study aims to expand upon simulation tools developed in the In Silico Clinical Trials for the Treatment of Acute Ischaemic Stroke (INSIST) project (Konduri et al., 2020; Miller et al., 2021). The objective is to incorporate AI-assisted in-silico osmotherapy trial into the existing FEM osmotherapy model and explore treatment protocols that are optimal. The deep learning model can incorporate statistics therefore establish a connection between patient characteristics and low information-noise ratio clinical data with an FEM model based on mathematical and mechanical theories. Once a reliable model is established, it can enhance the precision of resource-intensive clinical studies, consequently reducing the enormous costs. Drawing inspiration from recent studies on biofluid transport in the brain (Li et al., 2009; Sweetman et al., 2011; Tully & Ventikos, 2011; Yuan et al., 2013; Mokhtarudin & Payne, 2015; Guo et al., 2018; Vardakis et al., 2019; Józsa et al., 2021a; Miller et al., 2021; Józsa et al., 2022) and recent AI applications in biomedical studies (Lipkova et al., 2022; Sapoval et al., 2022; Qiu et al., 2022), the first AI-assisted FEM model for investigation of osmotherapy is proposed.

In this model, we will present the prediction of the ICP evolution using DNN model during osmotherapy episodes on a quasi-population level. The study consists of the following parts: (1) the FEM model and the training and testing of the neural network will be presented; (2) the effects of the parameters on the main features of the osmotherapy will be investigated; (3) the efficiency of the osmotherapy will be evaluated using two criteria and the effects of different parameters will be presented; (4) proper doses of osmotic agents will be proposed for different levels of BBB damage and age groups.

6.2 Methods

The model consists of two components, including the FEM model and the artificial neural network. In the FEM model (Chen et al., 2022), the brain is assumed to consist of four compartments, i.e., tissue, arteriole, capillary, and venule network and can thus be considered a multi-network fluid dynamic system. The modelling pipeline consists of three 3D models for the simulation of blood perfusion, oedema, and osmotherapy, respectively. After in-silico trials, the DNN model is trained using the ICP data generated from the FEM model. The perfusion model section is the same to section 3.2.1 and the oedema and osmotherapy models are presented in 3.2.2. Here, we present the neural network and how the DNN is coupled with in-silico model from Chapter 3.

6.2.1 Design of Deep Neural Network Model

To facilitate the simulation process, we developed a deep neural network (DNN) model to explore the relationship between the parameters and the ICP change. The model has an input of five parameters, including the tissue storage factor C, tissue hydraulic conductivity K, blood vessel permeability L_p, arterial blood pressure ABP, and the maximum osmotic pressure Π_{Max}. The

parameters L_p, C and K are varied between 0.5 to 2 times their baseline values, and the blood pressure ABP is varied between 80 mmHg to 100 mmHg. The dose maximum osmotic pressure is varied between 900-3600 Pa. The output is a sequence of 49 data points for the ICP values at different time during an osmotherapy episode. We tried different architectures for the DNN model design, including the models using dense layers, convolutional layers (Conv), long short-term memory (LSMT) layers, residual connection, and batch normalisation layers; and we also investigated the prediction performance in terms of different model hyperparameters, such as different kernel sizes and the number of hidden layers. Using trial-and-error, we searched for an optimal model with the minimal error for the ICP value estimation. As shown in Fig.6.2, the final searched DNN model* has six convolutional layers and two residual neural network (ResNet) blocks.

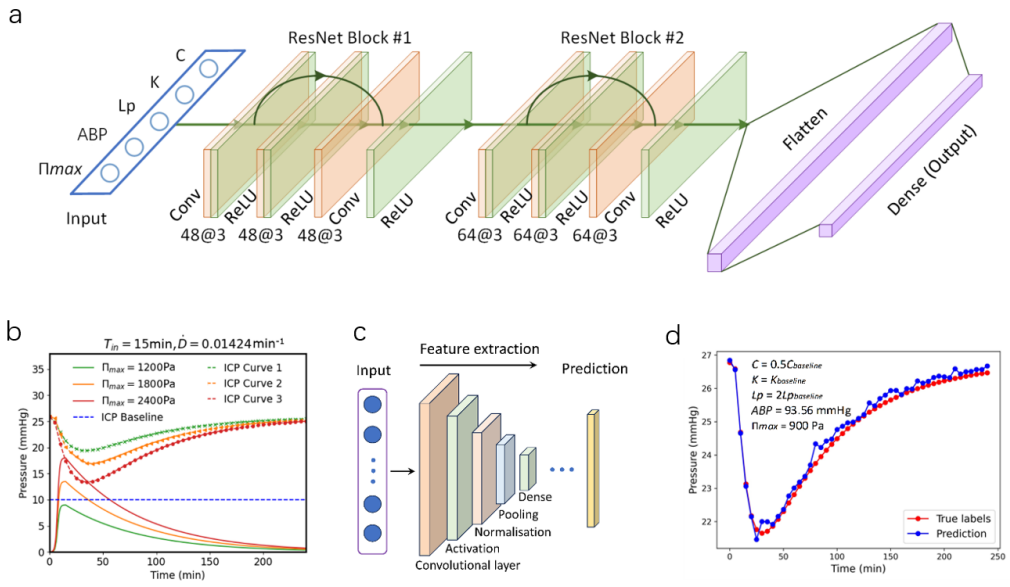

Figure 6.2: (a) The architecture of DNN model for the ICP value prediction. (b) Relationship between different ICP curves and the maximum osmotic pressure values, generated from FEM model to train the DNN (c) Illustration of DNN model design. (d) ICP value prediction using the developed DNN model.

* Le Lu designed this neural network architecture.

In the first ResNet block, the convolutional layers have 48 kernels with the size of 3; and in the second ResNet block, the convolutional layers have 64 kernels with the size of 3. Then, a dense layer is used to produce the output for the ICP value estimation. The mean squared error between the ICP value and the estimation, summed over all time points, is used as the loss function. The model was trained for 100 epochs with a batch size of 16 and a learning rate of 0.001. Generally, the best model was decided based on the minimal loss during training.

6.2.2 Model Coupling

The location of leaking vessels obtained from the perfusion model is then used within the oedema model. The perfusion in brain tissue of the healthy and stroke scenarios can thus be compared. The perfusion (F) and perfusion change (ΔF) are given in Equation3.8 & Equation3.9. A threshold of 70% or greater blood perfusion reduction (Campbell et al., 2015; Payne, 2016; Jovin et al., 2017) is utilised to determine the region of leaking vessels. Thereafter, the pressure field in the oedema is simulated until the ICP (defined to be the same as p_w) reaches equilibrium by using the stroke simulation results as the initial condition. Finally, the osmotherapy is assumed to be performed after the ICP reaches equilibrium and thus the pressures at the final step in the oedema model are used as the initial pressures in the osmotherapy model. A full space searching is performed for {C, ABP, K, L_p, Π_{Max}}, and 2000 in-silico trials are simulated using FEniCS open-source platform. The data is then used to train and test the artificial neural network, as shown in Fig.6.3.

As parameters vary among patients, the baseline parameters in the models and numerical methods are chosen to be the same to Chapter 3.

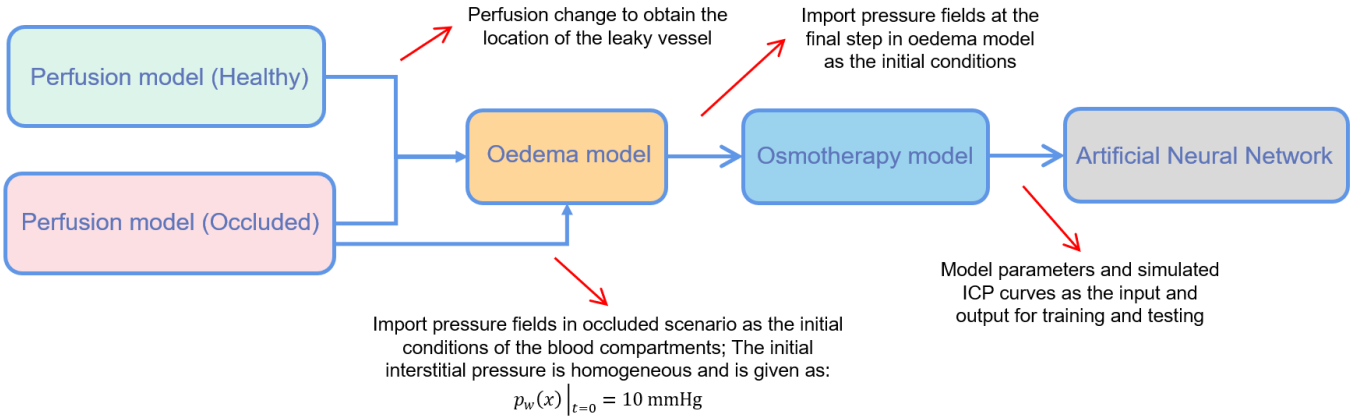

Figure 6.3: Flowchart demonstrating how the Finite Element models are coupled and used to generate data for artificial neural network.

6.3 Results

6.3.1 DNN Model Training and ICP Value Estimation

We used a total of 2,000 in-silico samples for the DNN model development, out of which we randomly selected 1,600 samples for model training, and the remaining 400 samples were held out for model testing. To obtain a reliable model, we used 10-fold cross-validation to train the DNN model. As illustrated in Fig.6.4(a), we divided the whole dataset into training and testing sets, the training data were then randomly split into 10 folds. During each training, 9 of the 10 folds were used for model training and the rest fold was used for validation. For each iteration, the DNN model was trained for 100 epochs, and the model with the minimal estimation error was stored. The searched optimal model was then used to predict the ICP values in the hold-out testing dataset, which had the performance of 0.249 ± 0.009 mmHg for the error of estimating the pressure. As illustrated in Fig.6.4(b)-(d), we show three examples of estimation the ICP values with varied input values. It can be seen from the sub-figures that the developed DNN model efficiently captured the underlying trend and estimated the pressure values. In particular, the DNN model successfully identified data points of the lowest pressure around 30, 50, and 100 mins for the three different inputs.

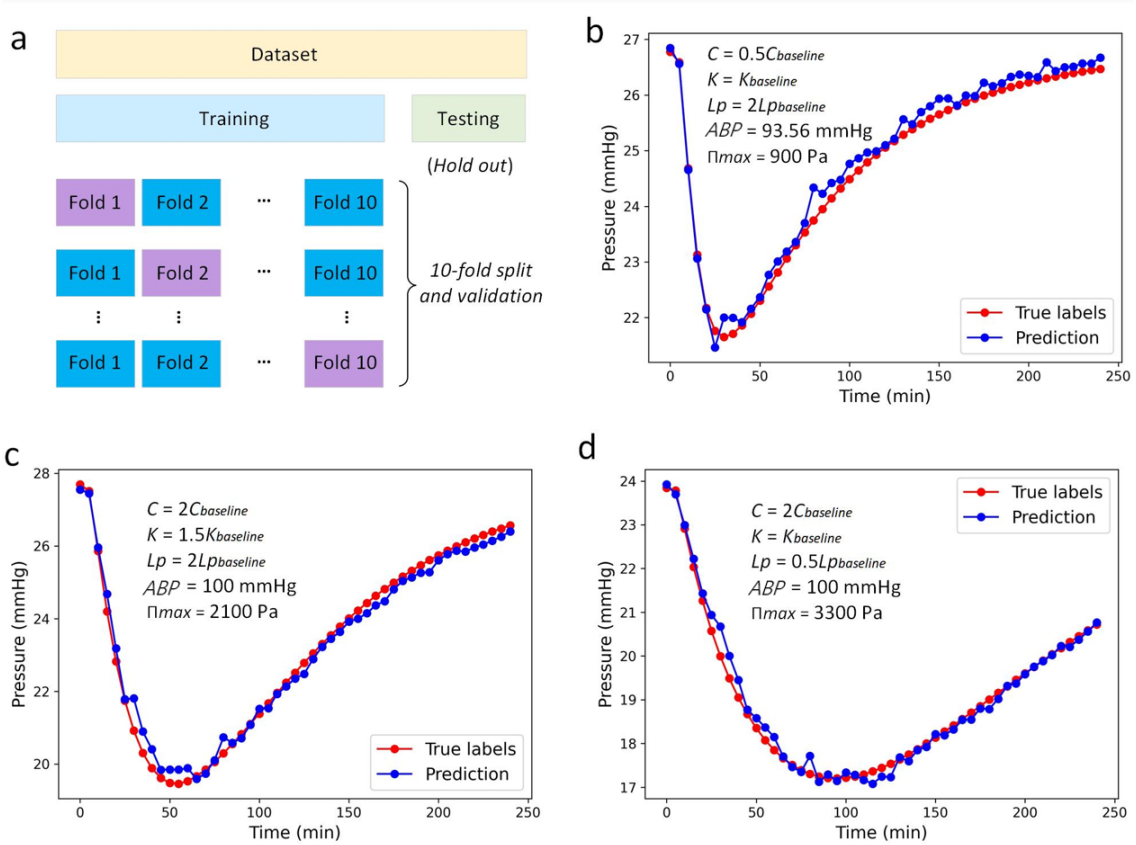

Figure 6.4: Prediction of the ICP value using DNN model. (a) Model training using 10-fold cross-validation, (b) - (d) Testing results for the ICP value estimation with different model input parameters.

6.3.2 Effect of Patient-specific Parameters on ICP Curve Evolution

We first investigate the effects of the physiological parameters on the features of ICP curves over an osmotherapy episode. The parameters vary with patients and are challenging to measure in clinical settings. However, previous studies indicate a variation of the parameters in different patient groups. For example, the CSF clearance rate in smokers was reported to be lower than in non-smokers, indicating a lower tissue hydraulic conductivity (Guo et al., 2020). Meanwhile, the blood vessel leakage was found to be larger in elderly patients, implying a larger L_p (Verheggen et al., 2020). In this study, we investigate the effects of different parameters by fixing one of the four parameter inputs

and fixing the injection dose input while the rest of the parameters are varied randomly around the baseline. The value of the L_p, K, or C range from 0.5 to 2 times the baseline value and the ABP ranges from 80 mmHg to 100 mmHg. 1600 results are generated for each parameter using the artificial neural network and the initial ICP, lowest ICP and the final ICP at the end of the episode are plotted as boxplots to show the difference on a quasi-population level (Fig.6.5).

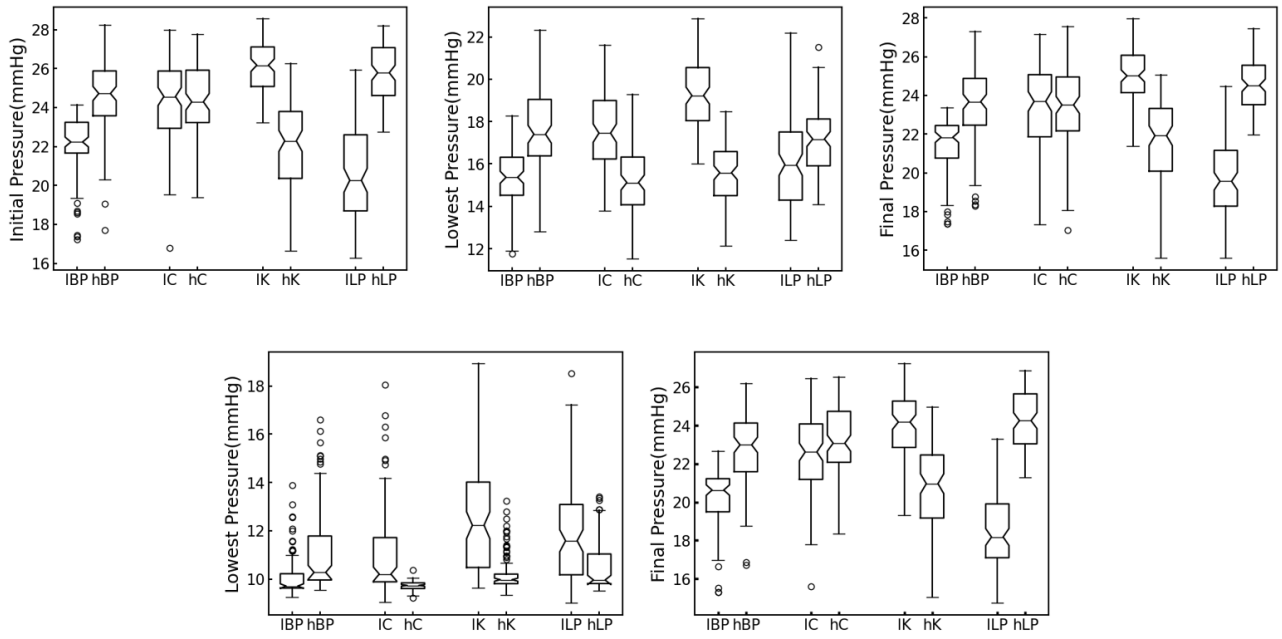

Figure 6.5: The features of the ICP curve as the flow parameters change. The first row shows the case where dose of injection leads to a maximum osmotic pressure of 1800 Pa, whereas the second row represents the case where maximum osmotic pressure is 3600 Pa. The lBP, hBP denote 80 mmHg and 100 mmHg arteriole blood pressure, respectively. Meanwhile, the lC, hC, lK, hK, lLp, hLp represents 0.5 and 2 times the baseline values of the physiological parameters, with "l" for 0.5 and "h" for 2 times.

The plots show that the L_p has the most significant effects on the initial ICP, with a mean of around 20 to 25 mmHg. Meanwhile, the brain tissue hydraulic conductivity also affects the initial pressure, with a mean ICP ranging from 23 to 26 mmHg. Surprisingly, the blood pressure value has only limited

effects on the ICP from around 22 to 25 mmHg. It is also noted that the storage factor does not present any significant effect on the ICP at the start of the therapy. Furthermore, it is obvious that the lowest pressure is strongly dependent on the dose of the osmotic agent. By comparing the 1800 and 3600 Pa cases, the lowest ICP can reach a much lower value with most cases showing the lowest pressure value of around 10 mmHg. In the 1800 Pa maximum osmotic pressure case, the storage factor presents a strong influence on the lowest ICP whilst the effects of the L_p become less significant compared to its impact on initial pressure. The arteriole blood pressure also shows a remarkable influence on the lowest pressure. Finally, no notable difference between the final pressure and the initial pressure is found in the virtual patients, indicating a pressure rebound back to a high level at the end of the episodes.

6.3.3 Evaluation of the Osmotherapy over an Episode Based on Two Criteria

Apart from the effects of the parameters on the ICP curves, the estimation of the effectiveness of osmotherapy is critical in designing a proper treatment plan for different patients. The flow parameters are varied within 0.5 to 2 the baseline values while the blood pressure is varied between 80 mmHg to 100 mmHg. The maximum osmotic pressure here is chosen to be 1800 Pa. Two criteria are utilised to estimate the effectiveness of the episode. As the major goal of osmotherapy is reducing ICP below 20 mmHg, the duration of time of the ICP below 20 mmHg in an episode is divided by the duration of the episode to obtain a time ratio and to indicate how effectively the ICP is reduced. In addition, the overall pressure drop is divided by the overall rise in the osmotic pressure in the blood during an episode of 240 mins (Equation 3.11)

In Fig.6.6, virtual patient groups are generated, and 1600 episodes outcome are predicted in each group. To avoid cases with initial pressure below 20 mmHg, only those virtual patients with initial ICP over

25 mmHg are selected. The L_p show the most significant effect on the time ratio, ranging from around 7% to 22%, whereas the arteriole blood pressure shows a minor effect on the time ratio. Furthermore, the L_p influences the efficiency of osmotherapy by 25% (from an average of 65% to over 90%). The tissue hydraulic conductivity also affects the efficiency significantly, from 78% to 89%. It is also noted that the effects of storage factor and arteriole blood pressure have only a slight influence on the efficiency.

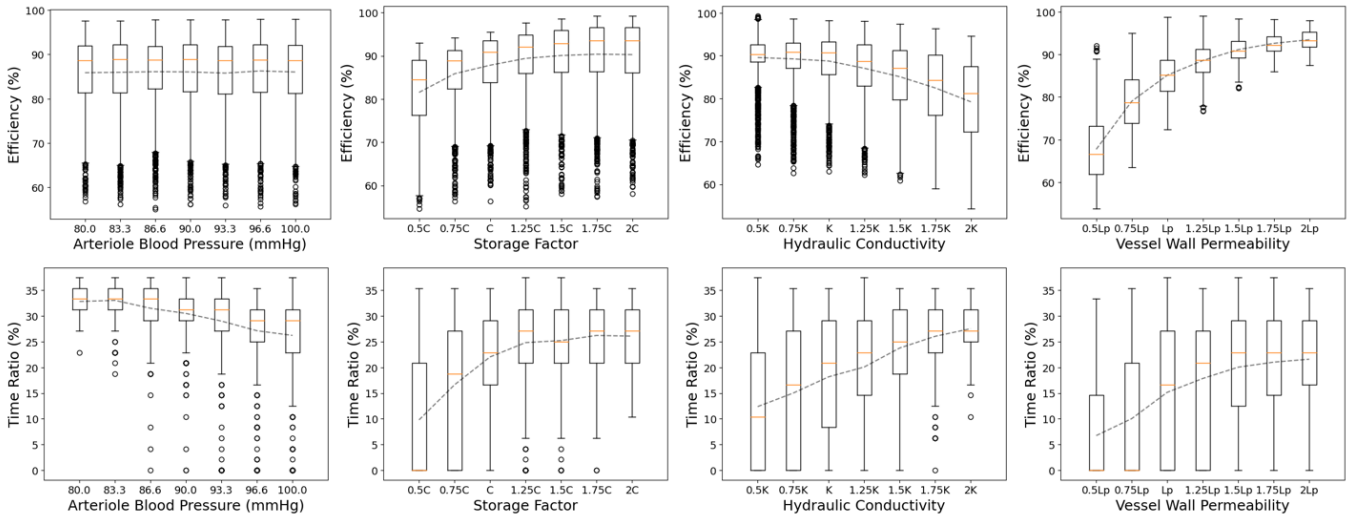

Figure 6.6: the time ratio of ICP below 20 mmHg and the treatment efficiency of an osmotherapy episode, where arteriole blood pressure (ABP) shows the blood pressure increment from baseline value of 80 mmHg, C is the storage factor, K is the tissue hydraulic conductivity and L_p the vessel wall permeability. The ABP's baseline value is 80 mmHg with a uniform increment to the maximum of 100 mmHg. The boxplots show the mean and outliers in the quasi-population level trial and the dotted lines shows the average values for different groups.

6.3.4 The Optimization of Medication Doses for Various Brain Damage Levels

In clinical settings, the physiological parameters vary in different patient groups, especially the vessel

wall permeability, which has been shown in the previous section to affect the therapy significantly. The post-stroke damage to the blood-brain barrier can vary depending on whether the treatment is successful. It is also determined by the timing of clinical treatment and the collateral score of the patients (Kimberly et al., 2018).

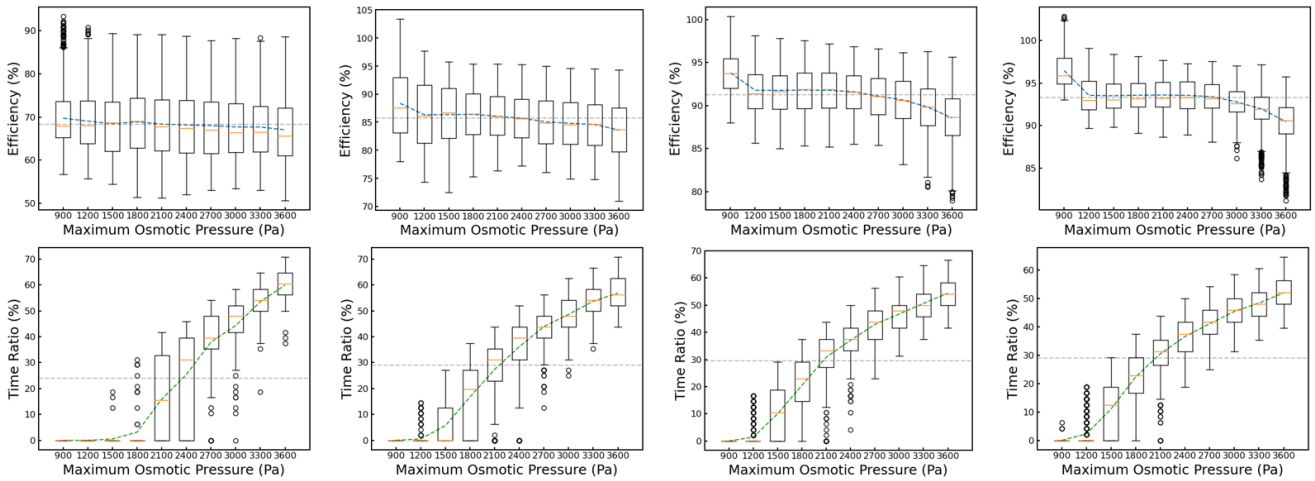

Figure 6.7: First row: the efficiency under different L_p values (0.5, 1, 1.5, 2 times the baseline) and doses of osmotic agent at each injection. The blue and green dotted lines show trend of the average values. Second row: the time ratio under different L_p values (0.5, 1, 1.5, 2 times the baseline) and doses of osmotic agent at each injection. The grey dotted lines represent the overall mean values.

The two criteria to evaluate the effectiveness of the therapy are both utilised. L_p values are varied between 0.5 to 2 times the baseline value, and the maximum osmotic pressure is varied between 900 to 3600 Pa. 1600 virtual patients are generated for each L_p value and dose. Similarly, to exclude patients with initial ICP lower than 20 mmHg, only the cases with initial ICP values over 25 mmHg are included (with a fraction of around 5%, 25%, 50%, 62% for $0.5L_p, L_p, 1.5L_p, 2L_p$, respectively).

In Fig.6.7, the efficiency of treatment is low in cases with low L_p (below 70%) cases but rises to an

average of over 90% in the high L_p cases (Fig.6.7). It can also be seen that changing the dose does not significantly change the efficiency on a quasi-population-averaged level, with only a slight rise when the maximum osmotic pressure is 900 Pa and a slight drop when the maximum osmotic pressure is 3600 Pa.

Furthermore, the maximum time ratio for different L_p values is largely constant, close to 70%. In addition, when the L_p value is low, there is a larger resistance to the flow of fluid from interstitial space back to blood vessels. Therefore, the time ratio is zero on average when the dose of the medication is small for the low L_p cases. The grey lines show the overall mean values of the time ratios. Osmotic agents with a maximum osmotic pressure of around 2400 Pa generally achieve the goal of sufficiently reducing the ICP to 20 mmHg in most cases (Fig.6.7).

6.3.5 The Optimization of Drug Doses for Various Age Groups

Here, we attempt to relate the model parameters with certain patient groups. In clinical settings, the age of patients is an important factor to consider as ageing changes not just the biomedical conditions of the patient but also the mechanical properties of the human brain. According to previous studies, ageing is related to a softening of brain tissue (Fallenstein et al., 1969; Jin et al., 2013; Budday et al., 2017; Budday et al., 2020), increased blood vessel leakage (Farrall & Wardlaw, 2009; Verheggen et al., 2020), a decrease in water content in the brain (Gottschalk et al., 2021; Rasmussen et al., 2022; Gracien et al, 2017) and a decrease in the CSF production rate (around half CSF production rate in the 70s compared to the 30s) (May et al., 1990). These indicate a lower interstitial fluid clearance rate, a higher vessel leakage rate, larger storage factor in the elder patients. Meanwhile, the mean arterial pressure (MAP) is not found to be statistically different between young and elderly patients (Yetim et al., 2023). The previous studies on these parameters are summarised in Appendix E.

Although there is a decrease in water content in the brain tissue and a decrease in the CSF production rate, quantitative studies on brain tissue hydraulic conductivity are rare. It is therefore assumed that in subject in their 90s has half the hydraulic conductivity as a result of the CSF production rate decrease in the elderly's brains. Meanwhile, the compression test of the brain tissue shows a doubled compression modulus in the 50s subjects compared to the 90s subjects (Budday et al., 2020) which indicates a smaller storage factor in the 50s. Additionally, twice the blood vessel wall permeability is implemented to reflect the two times difference in vessel wall leakage between the 50s and 90s populations, whereas the arteriole blood pressure at the pial surface is considered an approximation to mean arterial pressure (MAP).

To investigate the effects of ageing, patients between 50 to 90 years old are studied and 1600 virtual patients are generated for each group. The vessel wall permeability and storage factor are given a random number between 0.5-1 the baseline value for the 50 years group, and these randomly generated values are doubled to represent the 90 years group. Tissue hydraulic conductivity is given a random number between 1-2 the baseline value and halved in the 90s age group. In the meantime, the arteriole blood pressure values are generated randomly between 80 to 100 mmHg for both age groups. The efficiency and time ratio for the evaluation of osmotherapy episodes are shown in Fig.6.8.

In the results, it can be seen that the efficiency of the 90s age group is higher than for the 50s population, with an average efficiency of 95% compared to around 84% in the 50s age group. As to the time ratio, the 50s shows a significantly more homogeneous time ratio distribution when compared with a large variation in the 90s. Furthermore, it can be seen that most patients in 50s have over 30% of the time achieving 20 mmHg and below when the maximum osmotic pressure is 2400 Pa. In contrast, the 90s only achieve 20 mmHg and below effectively when the maximum osmotic pressure is 2700 Pa.

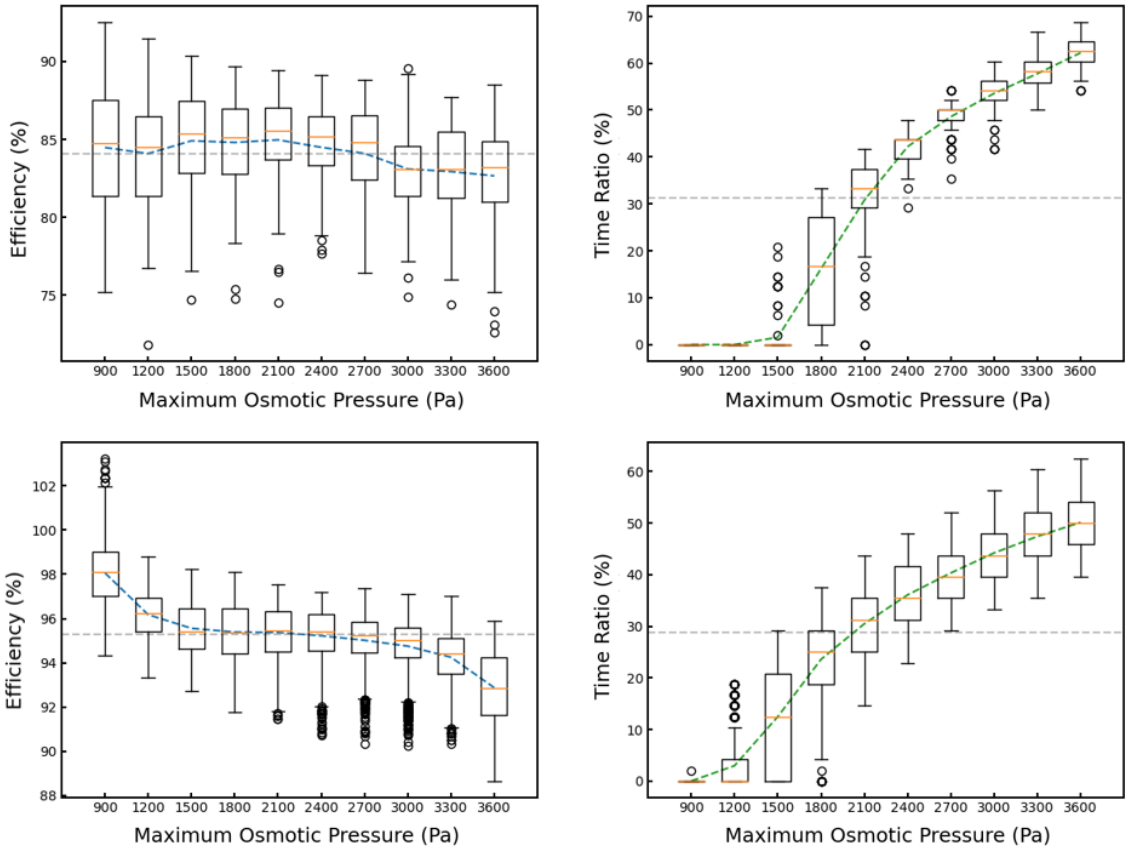

Figure 6.8: The comparison between the 50s and the 90s age groups. The first row shows the efficiency and time ratio of the 50s age group, and the second row shows the efficiency and time ratio of the 90s age group. The blue dotted line represents the average values and the grey dotted line represents the overall mean values. In the time ratio plots, the green line represents the average and the grey dotted line represents the overall mean of time ratio.

6.4 Discussion

This study presents the first in-silico trial assisted by a DNN. The DNN has also shown potential in processing patient data for diagnosis, treatment, biomedical signal processing etc. In clinical settings, the treatment of brain oedema is usually based on the medical history and other characteristics of the patients, for example, the ages, sex, etc. These patient data have been widely used to predict the outcome of oedema treatment, especially the ICP. However, how these characteristics are correlated

with the ICP and with other flow parameters remains unclear. In this study, flow parameters are varied, and DNN is utilised to generate virtual patients to present the influence of various parameters. Meanwhile, the patient brain's mechanical properties are related to patient groups of various levels of BBB damage and various ages. To the best of our knowledge, this is the first attempt to correlate the clinical statistics to a FEM mathematical model. This can help to bridge the gap between various methods in biomedical studies and provide a tool for the study of brain oedema supported by both well-founded mathematical and mechanical theories and real patient data and information.

In the DNN predicted results, the initial ICP mainly depends on the L_p and the hydraulic conductivity. In contrast, the effect of arteriole blood pressure is not as significant as a variation of ABP from 80 to 100 mmHg only leads to an around 2 mmHg difference in the initial ICP in the virtual patients. This indicates that fluid accumulation is highly dependent on the restriction of the blood-brain barrier on the fluid flow through the vessel wall. Meanwhile, the lowest ICP is strongly affected by the choice of storage factor. As the brain tissue with a small storage factor can respond to the osmotic pressure rise in the blood vessel in a shorter period of time, brains with a small storage factor also experience a faster pressure rebound after the osmotic pressure drops and the drug concentration reaches the peak. Therefore, the storage factor of the brain tissue has multiple effects on the ICP curve. Interestingly, the virtual patient data show that a large storage factor (which means the tissue is softer) can lead to a lower minimum ICP during an episode in the virtual patients. This demonstrates that a large storage factor (softened brain) is favourable to achieving a lower ICP.

Finally, the AI-assisted in-silico trial is evaluated based on two criteria, the time ratio, and the efficiency. The model is used to study different patient groups, including patients with various levels of BBB damage and patients at different ages, namely the 50s and the 90s. In the patient groups with different L_p values, the efficiency is only slightly affected by the dose of the osmotic agent on an

average level. Differing from my previous study on osmotherapy (Chen et al., 2022), where the dose of the medication shows a strong influence on specific cases, the improvement in efficiency diminishes because of the randomness of other physiological parameters. However, it is challenging to obtain the exact value of the parameters and it is therefore reasonable to consider an optimization on a population-averaged level. Meanwhile, the virtual patients show a notable difference in the required dose to achieve 20 mmHg ICP and below, which indicates the dose can be optimised for different levels of BBB damage on a population level. Furthermore, the simulation results show a high treatment efficiency in the 90s, which is because of higher vessel wall permeability and the higher storage factor. Meanwhile, the virtual patient groups show that less dose is needed for the elderly (90s) to achieve proper ICP reduction and therefore, considering the various side-effects of osmotic agents, less dose is suggested to be used for the elderly patients with oedema onset.

6.4.1 Limitations

It should be noted that there are several limitations to this study. Firstly, many parameters have been used in the multi-compartment models and it is challenging to determine some of the parameters from the existing experimental data. Due to the various experimental methods adopted in the previous studies, the parameters shown in experimental studies vary significantly, even though the real physiological values usually do not vary beyond the 50%-200% range (see for example, Sack et al., 2009; Montagne et al., 2015; Budday et al., 2020). Additionally, some of the parameters are not yet available in the human brain and data from animals were thus used as necessary (Harper & Bohlen, 1984; Józsa et al., 2021a). Furthermore, the multi-compartment porous model hinges on the principles of multi-scale separation and the homogenization of cerebral tissue. Notably, this approach involves homogenizing the mechanical properties of the entire brain, thereby overlooking the spatial variations in tissue properties across different brain regions. The model addresses discrepancies between white and grey matter while leaving the properties of other brain regions unexplored due to limited experimental data supporting a model elaborated with anatomical features.

In conclusion, this is the first study combining the conventional FEM model with machine learning methods to investigate osmotherapy on a quasi-population level. Once more accurate mechanical properties and physiological parameters of the brain become available, the model will be able to provide a more accurate prediction of clinical outcomes and thus improve the clinical treatment of brain oedema.

Author Contribution

Conceptualization: Xi Chen, Lei Lu

Data curation: Xi Chen.

Formal analysis: Xi Chen.

Funding acquisition: David A. Clifton, Stephen J. Payne.

Investigation: Xi Chen.

Methodology: Xi Chen, Lei Lu.

Project administration: Stephen J. Payne.

Resources: Xi Chen.

Software: Xi Chen and Lei Lu.

Supervision: Stephen J. Payne.

Validation: Xi Chen.

Visualization: Xi Chen.

Writing– original draft: Xi Chen, Lei Lu.

Chapter 7

Conclusions and future work

7.1 Conclusions

Thus far, I have proposed a novel tool for the simulation of post-stroke oedema and haemorrhage based on previous simulation models developed in INSIST project. The models further developed the blood perfusion and oedema models (Józsa et al, 2021a; Mokhtarudin 2016) to simulate large deformation and osmotherapy. The model includes four components for the simulation of healthy blood perfusion, occluded blood perfusion, oedema/haemorrhage, and osmotherapy. Compared to our previous models, the models presented in the thesis can simulate brain oedema with large deformation and can also be used to study brain injury prediction (Chapter 4), clinical decision-making (Chapter 5) and treatment optimisation (Chapter 3&6). This provides the first computational tool for a thorough investigation of post-stroke brain injuries. The nature of this multi-physical model allows us to simulate both the pressure and deformation of the brain and therefore provides us with comprehensive information about the blood perfusion, blood flow rate, ICP, MLS, stress and stretch in the brain tissue. These parameters can be challenging to obtain in clinical settings and thus the conclusions from the models can potentially provide guidance for clinicians and improve the prevention, treatment and diagnosis of brain injuries in the future.

The model is first applied for the simulation of osmotherapy. Although it has been widely used in clinical settings for the release of ICP in brain oedema, the effects of the therapy have remained controversial. The physiological parameters and the administration parameters were thus investigated to illustrate their effects on the osmotherapy. Also, the model is utilized to study two common scenarios when osmotherapy can fail and corresponding strategies to improve the effectiveness are suggested. In the slow-changing ICP curve scenario, additional dose of medication is suggested, whereas alternative osmotic agent is suggested for the fast-changing ICP curve scenario.

Furthermore, the model was developed for the simulation of the haemorrhagic transformation, which commonly occurs alongside oedema and causes severe damage to the brain. To include the blood flow in the interstitial space, the blood flow was modelled, and the haematoma volumes generated from simulations were compared with clinical imaging data. The impact of haematoma on the local blood perfusion is compared. To further understand the effects of high blood pressure, blood glucose, etc., a parameter sensitivity analysis was conducted. The study indicates that high blood pressure and high blood glucose can lead to severer brain haemorrhage. The model provides the first in-silico investigation of brain haemorrhagic transformation in the full brain and therefore provides insights into its damage after stroke treatment.

In the investigation of the ICP-MLS relationship, the model is first compared with clinical MLS and ICP data provided by collaborators. The ABP and intraparenchymal ICP are measured in 97 patients. The linear relationship between the ABP and ICP shown in the clinical data (Cardim et al, 2021) is generated from the computational model for the validation of pressure field computation. Meanwhile, the in-silico and clinical MLS values are compared to tune the parameters of the mechanical properties of the brain tissue. Based on the simulation results, the stress, stretch, pressure, water content and

displacement in the brain are presented. During the development of oedema, the periventricular region exhibits a reduction in the water content whereas the intraparenchymal regions presents an increase in the water content. Furthermore, the stress concentrates at the corners of the ventricle surface and can cause damage to the periventricular regions of the brain.

In the study, the various MLS-ICP relationships have been quantified and the MLS-ICP relationship for different patient geometries, BBB damage severity levels and oedema types. The simulation results show that the MLS-ICP relation is multi-factorial and is most strongly affected by the geometry and location of the oedema volume. This study provides the first computational tool for the investigation of brain deformation and ventricle collapse in oedema. Furthermore, clinical advice was given to predict ICP more accurately. For the PCA type oedema, MLS is small and should be noted as PCA oedema patients can experience high ICP whilst MLS is not observable on clinical images.

Finally, an AI-assisted FEM model was proposed for further investigation of the optimization of administration protocols. The deep neural network (DNN) used five FEM model parameters as model input and the output of the ICP pressure change over an osmotherapy episode. The ICP curve learned by the DNN model showed an excellent agreement with the in-silico results. By using the model, the effects of the parameters and the choice of dose of osmotic agents were investigated and discussed. In addition, clinical stratifications of patients were related to a brain model for the first time for the optimization of treatment for different patient groups. 90s age group can experience severer oedema and thus require a higher dose to achieve effective treatments.

7.2 Research Implications

In the thesis, the osmotherapy models propose a novel method for the simulation of brain oedema therapy with the assistance of DNN. Considering the difficulties in measuring intracranial pressure,

in-silico models can provide valuable information for the optimisation of the therapy by producing massive virtual patient data supported by physical laws. This approach can inspire not just the study of other types of brain oedema, such as oedema after traumatic injury and oedema in brain tumours, but also the broader field of the in-silico trials of other diseases, where some critical physiological parameters can be hard to measure in clinical settings. For example, in the field of cardiovascular diseases, high blood pressure can lead to vessel rupture and bleeding (Fuchs & Whelton, 2020). In the study of skeleton mechanics, stress and load can lead to bone fracture in bones because of ageing vitamin D deficiency and osteoporosis (Zimmermann et al., 2015; Hoenig et al., 2022). Furthermore, the combination of DNN and in-silico model provides a novel approach for the investigation of biomedical problems supported by both physical laws and biostatistics and therefore inspires the in-silico modelling of various diseases that is governed by both patient characteristics and biomechanics (Shakoor & Moisio, 2004; Lee & Lim, 2007).

The thesis also proposes a model for haematoma simulation. In clinical settings, haematoma has been hard to investigate from clinical imaging data, as the measurement of blood flow and the segmentation of haematoma volume can be challenging (Kidwell & Wintermark, 2008). By using the model at an organ scale, we are able to validate the model with clinical imaging data and investigate brain haematoma development under different physiological parameters. The clinical studies of brain haematoma will benefit from this as the study provides the fact that high blood viscosity caused by high blood glucose will lead to severer haematoma. The modelling of haematoma is challenging, and this study is the first modelling of haematoma in a whole brain model. The model highlights the importance of high blood pressure and high blood glucose in predicting HT severity and can potentially help understanding the mechanisms of HT. Thus, this study demonstrates the role of mathematical modelling in supporting clinical trials and facilitating further development of computational methods for haematoma.

Furthermore, the impact of three physiological features on the development of oedema provides clinical guidance for the treatment of oedema and clinical decision-making. This will contribute to the understanding of the factors that can lead to high-noise clinical data (Miller et al., 2004). Once these impacts can be considered in the clinical estimation of ICP from MLS, the noise is expected to be reduced and thus other factors that might affect the ICP-MLS relationship will be highlighted. The model also incorporates large deformation and simulates ventricle collapse for the first time. The simulation results show that the measurement of MLS can be dependent on the locations of MLS measurements, because of the additional obstruction and displacement caused by the contact between structures in the brain. These findings propose that mechanical problems can be important in the clinical investigation of brain oedema. As MLS is a critical criterion in clinical settings, this also implies that the clinical measurement of MLS should be revised and different measurement protocols (Liao et al., 2018) should be compared for a more accurate oedema severity estimation in the future.

7.3 Future Work

7.3.1 Incorporation of Autoregulation

Autoregulation plays a key role in regulating the blood flow when the perfusion blood pressure changes (Paulson et al., 1990). Over the past three decades, significant progress has been made in the development of cerebral autoregulation models (Zagzoule & Marc-Vergnes, 1986; Mitsis et al., 2002; Payne, 2006; Golubev et al., 2022). These models have offered valuable insights into the mechanisms governing autoregulation. Due to the considerable range of length scales in the brain, the scales of interest in cerebral blood flow (CBF) models exhibit a substantial variation. These models can range from relatively large-scale lumped compartment models (Olufsen et al., 2002) to small-scale single-vessel models (Alastruey et al., 2008). Until now, autoregulation has not been incorporated into the length scale of a full brain model in previous studies.

Autoregulation is neglected as in the model used in the thesis, the perfusion is modelled as a static flow. In fact, a model considering autoregulation can help understand the mechanisms of brain stroke and brain damage therefore facilitating our understanding of the brain damage caused by blood perfusion reduction. The incorporation of autoregulation involves the coupling of mathematical models to represent autoregulation (for example, Olufsen et al., 2002) and the whole brain model to simulate the blood flow rate and blood perfusion volume. A model incorporating autoregulation can also generate a stroke brain where blood perfusion can vary during the stroke and damage to the blood-brain barrier. Consequently, the model is expected to generate different infarct regions and thus different damaged tissue volumes and oedema cores. Meanwhile, blood perfusion can also be affected by autoregulation and autoregulation is also impaired after stroke, making them strongly coupled and thus can influence both the blood flow field and haemorrhage development.

7.3.2 Patient-specific Vessel Geometries

The oedema and haemorrhage can both be affected by the patient-specific geometries of blood vessels, as the large vessels might lead to a larger blood flow volume in the region of penetration. Homogenised whole-brain models have been developed in this DPhil study for the investigation of brain oedema and its treatment. However, there is still a lack of patient-specific models (Otani et al., 2023) that incorporate patient-specific vessel geometries that can significantly affect cerebral blood flow dynamics. In previous studies, arterioles and arteries can be modelled based on existing MRI/CT image segmentation techniques using deep neural networks and this latest advancement (Lin et al., 2023) in computational imaging techniques provides a possibility of coupling large vessels with the existing whole-brain models.

The blood vessels can have various diameters and the small vessels (diameter below 100 μm) can be

difficult to extract from brain imaging, as the vessel geometries extraction is limited by the resolution of brain imaging. Therefore, only large vessels (diameter over $100\mu m$) can be incorporated and the coupling of the large blood vessels and whole brain model will require a fluid transfer term between the CFD model, which simulates the blood flow and the FEM model, which simulates the brain as a porous medium. Blood flow dynamics can be investigated and consequential effects on oedema core geometry, tissue stress and strain can be discussed. To validate the model, various brain imaging data, including perfusion- and diffusion-weighted MRI can be compared with the simulation results. Furthermore, the model can generate an automatic image processing technique to assist patient-specific modelling by incorporating the blood vessel geometries. Finally, the difference in blood flow and intracranial pressure can be discussed and compared to the homogenised model to understand the importance of patient-specific modelling.

7.3.3 Patient-specific Spatial Distributions of Physiological Parameters

According to previous studies (Budday et al., 2020), the brain tissue has been demonstrated to be highly anisotropic and heterogeneous. However, the limited experimental data has restricted the application of a brain model with more anatomical details of the brain. In the study presented by Jamal et al. (2020) and Vidotto et al. (2021) the brain tissue shows an around halved permeability in the white matter where the interstitial flow is perpendicular to the direction of neurons. Meanwhile, the brain tissue is heterogeneous. The stiffness of the brain tissue varies in different regions of the brain (Budday et al., 2020). This indicates that it is necessary to consider the spatial variation of brain mechanical properties for a more accurate simulation of oedema and haemorrhage. As the mechanical properties of the brain regions are not significantly different in the brain regions, the major conclusion of the thesis is not expected to be affected and the focus of the novel model will be providing a more precise prediction of brain oedema.

The incorporation of tissue heterogeneity will require further subdivision of the computational domain in order to impose different mechanical properties in different brain regions. Meanwhile, a permeability tensor will be needed to implement the anisotropy of brain white matter. As we have already had a brain model with grey and white matter subregions and anisotropic blood permeability in the arteriole and venule compartments, the imposition of heterogeneity and anisotropy will be straightforward. The variation in these properties is expected to lead to a difference in the distribution of tissue stress, interstitial pressure, and displacement. The impact will depend on the variation in the mechanical properties, especially the local impacts on the brain deformation and stress in the brain regions.

In recent studies, these properties vary in different brain regions and the experimental results vary due to the different experimental techniques in previous studies. Therefore, it is challenging to determine the accurate physiological parameter distributions across the human brain. Once more accurate experimental data become available, the model will be able to incorporate these anatomical features and provide more accurate simulation results. A factor to investigate here is the stress distribution. In my work, I find that the stress can concentrate on the ventricle corner, which indicates that brain geometry can affect the distribution of brain tissue stress in oedema. It is interesting to see how the geometry combined with heterogenous shear modulus can lead to high stress and hence high damage to certain brain regions in oedema.

7.3.4 Refinement of Boundary Conditions

The brain model is bounded to ideal boundary conditions that consider the ventricle surface as a free boundary and the pial surface as a fixed boundary. The pial surface is assumed to be a fixed boundary as the pial surface is fixed to the sub-arachnoid space and then connected to the skull, which is almost

rigid in this context. However, in some cases, the pial surface can deform and compress the subarachnoid space which is a structure supported by delicate connective tissue trabeculae and filled with cerebrospinal fluid (Miller et al., 2004). Hence it is possible to undergo deformation in severe brain oedema. As a result, the boundary can vary among patients and a refinement in boundary conditions can improve the accuracy of ICP-MLS relationship prediction, especially to refine the ICP-MLS curve predicted in the investigation of ICP-MLS curves in the thesis.

To improve the accuracy of brain modelling, the mechanics of subarachnoid space and the CSF can be incorporated into the model, as this helps to impose a more flexible boundary condition. However, the major challenge lies in the uncertainty of the mechanical properties of the subarachnoid space, as it comprises microstructures that can behave differently under compression. Once a better understanding of the mechanical properties of the subarachnoid space is achieved, the modelling of severe brain oedema will become more comparable to the realistic deformation of oedema brains.

7.3.5 Investigation of How Contact Affect the Midline Shift

In this DPhil, a mechanical solver for contact mechanics is developed for the simulation of brain ventricular wall contact in large deformation. The contact is not found to affect the midline shift measurement due to the simple measurement algorithm used in the study. However, in the clinical measurement of midline shift, the MLS is not measured on the entire mid-plane on the brain, but rather measured using imaging processing tools and the midline shift is usually measured on certain locations on the brain where any displacement is more visible. This can lead to over/underestimation of the midline shift in the model, as contact can lead to additional deformation or obstruction. Therefore, it is valuable to incorporate realistic clinical measurement of midline shift to mimic the clinical measurements. This will help in understanding how the contact and different measurement algorithms can introduce errors in midline shift and oedema severity estimation.

7.3.6 Acceleration of In-silico Trials with Neural Networks and Neural Operators

The brain model can provide details of the stress, interstitial pressure, and deformation in the oedema tissue. As demonstrated in the models, the simulation results vary with patient-specific geometries and physiological parameters. It is therefore necessary to conduct an in-silico trial for each patient to obtain more accurate results. However, such simulation is restricted by the computing power as a simulation in the model uses around a million mesh elements and can take hours or even days to run on a desktop. This can delay clinical decision for patient who are in urgent need of treatments. Meanwhile, the acceleration of in-silico model can require more advanced computing units and therefore become expensive. Recently, various neural networks and neural operators have been applied to solve PDEs within a shorter time. Once the neural network or neural operators are trained, the solutions of PDEs can be inferred in a shorter time than solving the PDEs. In the work of Li et al (2020), a Fourier neural operator (FNO) is proposed to solve fluid mechanics problems and a comparison with the PDE solution shows a good agreement while the computing time is reduced by orders of magnitudes.

In brain modelling, I used the CNN and ResNet architecture to predict the behaviour of different virtual patient groups to osmotherapy. The ICP curves for different patients are learned by a DNN in the AI-assisted model to avoid the time-consuming in-silico trial and to generate massive virtual patient groups. However, the study does not include the complicated geometrical features and only studies the variation of ICP over osmotherapy episodes. In the work of Wu et al. (2022), CNN and transformer are employed to predict brain displacement and stress during traumatic brain injuries. The trained neural networks can predict displacement and stress of brain tissue during impact within a shorter time and thus save time for faster clinical decision-making. Therefore, it will be interesting to further apply neural networks to the training of oedema in 3D

brain geometries for a faster oedema severity prediction.

7.3.7 Patient-specific Modelling Using Neural Networks

Due to the complex mechanical properties of the human brain, it can be challenging to model the mechanical behaviour of the brain with a FEM model, especially considering that the mechanical parameters in brain regions, exact boundary conditions on pial surface and the constitutive law (Budday et la., 2020) of the brain tissue can be unclear and challenging to describe. Therefore, neural networks and neural operators can take the advantage that they do not require explicit boundary conditions and mathematical descriptions of brain mechanical properties that are hard to obtain, and therefore provide a novel approach to investigate the response of brain tissue to intracranial pressure rise. For example, a physics-informed neural network (PINN) consists of a neural network for the approximation of the solution and loss functions comprising the losses of both PDEs and data (Karniadakis et al., 2021), therefore incorporating patient-specific considerations.

In previous studies, PINN has been utilised to infer the unknown parameters in the blood flow through a thrombus (Yin et al., 2021). The permeability of the thrombus significantly affects the flow fields and a data loss was introduced to the model to infer the input thrombus permeability. Meanwhile, DeepONet consists of branch nets and trunk nets and can infer flow parameters at any location in a flow field given the training dataset. The model was implemented for the inference of damage area on an aneurysm (Goswami et al., 2021). It will be an interesting project to utilise these neural networks and neural operators in the field of brain oedema and to simulate the displacement and blood flow in the brain. It can open up the possibility of simulating brain deformation and investigating brain oedema in a more patient-specific manner, especially by combining more uncertain mechanical properties, boundary conditions or even age and other demographic information.

7.4 Closing Remarks

Overall, the brain is a highly complicated fluid dynamic system that can experience post-stroke damages and injuries. This thesis presents computational models for the in-silico trials of brain oedema and haemorrhagic transformation to sharpen our understanding of these diseases from biomechanical perspective. Brain models for the simulation of ischaemic stroke, brain oedema, haemorrhagic transformation and osmotherapy are proposed for the first time. This provides a novel tool for the investigation and prediction of post-stroke brain injury. This thesis investigates (1) the treatment strategies for patients with different types of failure in osmotherapy (2) osmothereapy in different age groups (3) haemorrhagic transformation under various blood pressure and viscosity (4) MLS-ICP relationship and multiple brain mechanical features. Considering the complex nature of the human brain, it is proposed that the model can be further developed by incorporating heterogeneity, autoregulation etc. Furthermore, the model can be incorporated with neural network techniques, including neural networks and neural operators that incorporate patient-specific biological information and patient-specific brain disease investigation.

.

Appendices

Appendix A: Derivation of Fluid Filtration through Capillary Wall

Here, I employ the filtration theory and the Donnan effect, which has been used to model brain tissue in previous studies (Donnan, 1924; Elkin et al., 2010; Lang et al., 2014), to derive S_{cw}, i.e., fluid filtration through the damaged BBB. The filtration flux, J_{VA}, can be described by the following filtration equation as shown below.

$$J_{VA} = L_p[(p_c - p_w) - \sum_{m=1}^{M} \sigma^m(\Pi_c^m - \Pi_w^m)] \ , \tag{A1}$$

where L_p is the hydraulic permeability of the capillary wall, m is the different solutes, p_i is the hydrostatic pressure with subscripts that represent capillary blood pressure and interstitial fluid pressure. Meanwhile, Π_c and Π_w are the osmotic pressure for each water-soluble solute present in the blood plasma and interstitial fluid. σ is the reflection coefficient that varies from 0 to 1, where a value of 1 means that no solute can flow through the BBB. Meanwhile, the difference in osmotic pressure can be described by the equation:

$$\Pi_c - \Pi_w = \sigma\Pi_c \frac{1-\exp(\mathrm{Pe})}{1-\sigma\cdot\exp(\mathrm{Pe})}, \tag{A2}$$

where Pe is the Péclet number. Here the Péclet number is much smaller than one (Zhang et al., 2006; Mokhtarudin, 2016) and for a fixed composition of the filtration model, we thus have

$$J_{VA} = L_p[(P_c - P_w) - \sigma\Pi_c], \tag{A3}$$

Meanwhile, the fluid transfer between capillary network and interstitial space S_{cw} can be given as

$$S_{cw} = J_{VA} \frac{n_b}{\pi {R_c}^2} \int_0^\infty p(c)dc \,, \tag{A4}$$

where n_b is the volume fraction of blood vessel in a unit volume of brain tissue, R_c is vessel radius and $p(c)$, at each point in space over the distribution of vessel circumferences. By assuming that the perimeter of blood vessels remains constant, we have

$$\int_0^\infty p(c)dc = 2\pi R_c, \tag{A5}$$

Substituting Equations A3 and A5 into Equation A4, S_{cw} can therefore be written as:

$$S_{cw} = 2n_b \frac{L_p}{R_c} \left[(P_c - P_w) - \sigma \Pi_c \right], \tag{A6}$$

Note that, for osmotherapy, we introduce an additional term to include the effects of saline:

$$S_{cw} = 2n_b \frac{L_p}{R_c} \left[(P_c - P_w) - \sigma \Pi_c - \sigma_{NaCl} \Pi_{NaCl} \right], \tag{A7}$$

L_p in the normal BBB has been estimated by Fraser et al. (1990) and this value can increase by more than 100 times the normal value (Hakamata et al., 1995). Due to the large difference between the BBB permeability in the damaged region and the healthy region, the flow from capillary blood to the interstitial space and the flow of interstitial fluid in healthy tissue is thus neglected.

Appendix B: Parameter Value Ranges

The ranges of the parameter values are listed in TableB1:

Physiological parameters					
ICP_{baseline}	5-15 mmHg	(Leinonen et al., 2018)	c_w	1.54×10^{-4} - 6.16×10^{-4} Pa^{-1}	Varied from 50% to 200% of baseline value (Mokhtarudin, 2016; Guo et al., 2020)
Oedema size	L-MCA and hemispheric	Most common stroke type is studied (Liew et al., 2018)	K_w	1.8×10^{-3} - 7.2×10^{-3} $mm^3 s\ kg^{-1}$	Varied from 50% to 200% of baseline value
σ	0.35-0.65	Estimated from the initial ICP value between 20 - 25 mmHg	L_p	6.0×10^{-12} - 6.0×10^{-11} m/s.Pa	Estimated from the initial ICP value between 20 - 25 mmHg
Administration protocol parameters					
Π_{Max}	1200 - 4800 Pa	Derived from the doses of saline (Kølsen-Petersen, 2020) and estimated from the maximum ICP drop	D	0.01 - 0.03 min^{-1}	Derived from elimination half-life 30 - 60 minutes (Paczynski, 1997)
T_{in}	10 - 30 minutes	(Kølsen-Petersen, 2020)			

Table B1: Sources of parameter values in the sensitivity analysis tests.

The values of σ and L_p are challenging to measure and are related to the severity of oedema. Therefore, these values are varied to obtain initial ICP values between 20 and 25 mmHg. Meanwhile, other parameters are not related to the severity of oedema and the parameter value ranges are summarized and given in TableB1. Note that where experimental data on human brain are not available, we assume that the physiological parameters varies from 50% to 200% of the baseline value, since this is the parameter range shown in most previous studies on brain properties (see for example, Sack et al., 2009; Montagne et al., 2015; Budday et al., 2020).

Appendix C: Intraparenchymal and Periventricular Stress in Oedema Brains in Quasi-patient-specific Brains

The stress in the parenchyma and at the ventricle corners can be plotted against the ICP and MLS, respectively for 18 patients' brains. As shown in the figure, the intraparenchymal stress is more related to the deformation of the brain and ICP values, whereas the periventricular stress is not as predictable as intraparenchymal stress. This indicates that the intraparenchymal stress is determined by the forces exerted by excessive ICP in the tissue and the periventricular stress is determined by the local tissue

deformation and quasi patient-specific geometries of the brains.

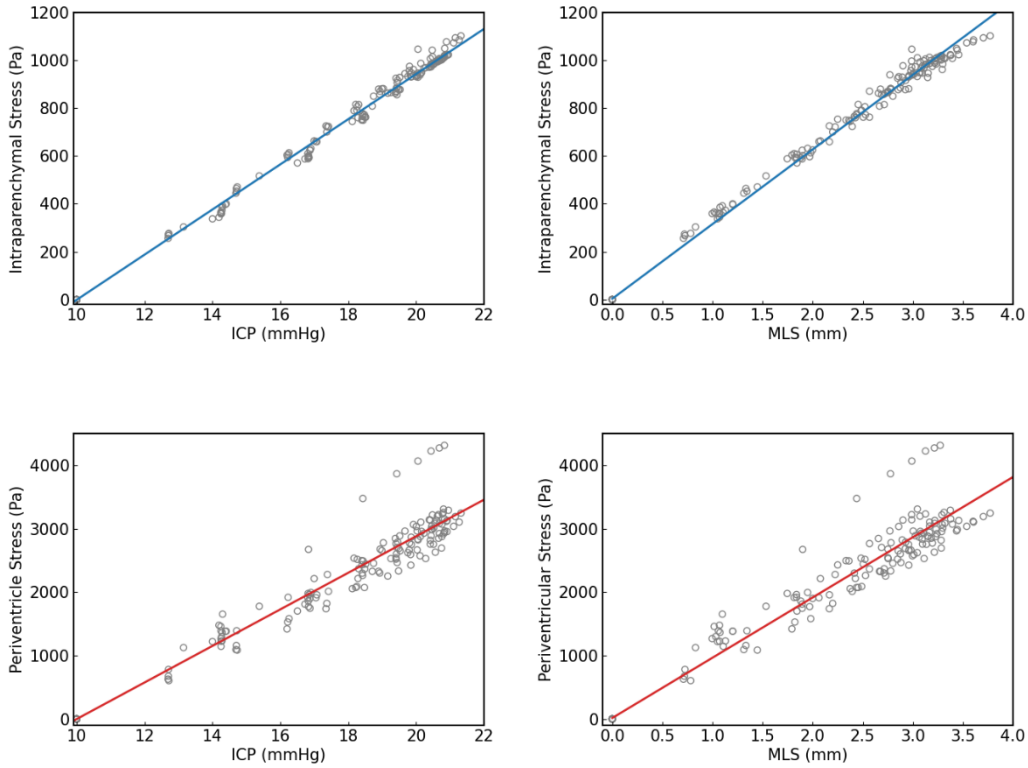

Figure C1: The intraparenchymal stress and periventricular stress vs ICP and MLS, where the blue and red lines are the best linear fit of the stress curves.

Appendix D: Mechanical Solver for Contact Mechanics

In the implementation of contact mechanics algorithm, we use Laursen's contact formulation (Laursen & Marker, 1995), where the displacement and the Lagrange multiplier are solved until convergence in both the inner and outer loop. For simplicity, we do not use the BFGS solver in the original method (Laursen & Marker, 1995) and we replace the line search with simpler relaxation coefficients. The algorithm can be written as:

Contact Mechanics Solver
1. Initialise the iteration process
a. Set initial values of displacement $\boldsymbol{u_0}$ and $\lambda^{(0)}$
b. Compute initial search direction $\Delta \boldsymbol{u_0}$ and compute initial energy $G_I = \Delta \boldsymbol{u_0} * R(\boldsymbol{u_0};\ \lambda^{(0)})$, where $R(\boldsymbol{u_0};\ \lambda^{(0)})$ is the residual force
c. Set iteration counters, $i = 0, k = 0$
2. Loop on displacement until equilibrium
a. Relaxation of displacement and move mesh
b. $i \mathrel{+}= 1$
c. Solve $\Delta \boldsymbol{u_i}$ and compute the energy of current step G_c
d. If ($G_c <$ ETOL$* G_I$), Then GOTO step 3
3. Augment
a. Compute new Lagrange multiplier λ^{tr}
b. Check convergence: IF $\left\|\lambda^{tr} - \lambda^{(k)}\right\| < KTOL * \left\|\lambda^{(k)}\right\|$ EXIT
c. $\lambda^{(k+1)} = \lambda^{tr}, k \mathrel{+}= 1$
d. Compute energy G_c and GOTO step 2

Table D1: Algorithm of contact mechanics solver.

As shown in the algorithm, our method uses two convergences criteria, ETOL and KTOL. The values are given 0.01 to ensure that the simulation reaches equilibrium and the penetration at the final step is sufficiently small, and thus guarantees the accuracy of the simulation. Meanwhile, the discretisation and linearisation are done according to (Wriggers, 2006).

Appendix E: Parameter Value Ranges

The ranges of the parameter values from the literature are listed in TableC1:

Physiological Parameters		
Arteriole blood pressure (Yetim et al., 2023)	95±11 mmHg in the 50s	98±11 mmHg in the 90s
Tension shear modulus (Budday et al., 2020)	Around 500 Pa in the 50s	Around 250 Pa in the 90s
CSF production rate (May et al., 1990)	0.41±0.24 in the 30s	0.19±0.07 in the 80s
Vessel wall leakage rate (Verheggen et al., 2020)	7.5 min^{-1} in the 50s	12 min^{-1} in the 90s

Table E1: Sources of parameter values in the 50s and the 90s age groups.

An around two times difference are shown in Lp and compression modulus between the 50s and 90s groups. Although the vessel leakage rate is measure in healthy brains, the value is simply taken to be around twice in oedema patients as there is not yet any relevant dataset.

References

Aarabi, B., et al. (2006). Outcome following decompressive craniectomy for malignant swelling due to severe head injury. J. Neurosurg., 104, 469-479.

Abbott, N. J., Patabendige, A. A., Dolman, D. E., Yusof, S. R., & Begley, D. J. (2010). Structure and function of the blood–brain barrier. Neurobiology of disease, 37(1), 13-25.

Adams, H. P., et al. (1994). Guidelines for the management of patients with acute ischemic stroke: A statement for healthcare professionals from a special writing group of the Stroke Council,

Alastruey, J., Moore, S. M., Parker, K. H., David, T., Peiró, J., & Sherwin, S. J. (2008). Reduced modelling of blood flow in the cerebral circulation: coupling 1-D, 0-D and cerebral auto-regulation models. International journal for numerical methods in fluids, 56(8), 1061-1067.

Alamowitch, S., Eliasziw, M., Algra, A., Meldrum, H., Barnett, H. J., & North American Symptomatic Carotid Endarterectomy Trial (NASCET) Group. (2001). Risk, causes, and prevention of ischaemic stroke in elderly patients with symptomatic internal-carotid-artery stenosis. The Lancet, 357(9263), 1154-1160.American Heart Association. Stroke, 25(9), 1901-1914.

Álvarez-Sabín, J., Maisterra, O., Santamarina, E., & Kase, C. S. (2013). Factors influencing haemorrhagic transformation in ischaemic stroke. The Lancet Neurology, 12(7), 689-705.

Ames 3rd, A., Wright, R. L., Kowada, M., Thurston, J. M., & Majno, G. (1968). Cerebral ischemia. II. The no-reflow phenomenon. The American journal of pathology, 52.

Amorim, R. L., et al. (2014). Improved hemodynamics parameters in middle cerebral artery infarction after decompressive craniectomy. Stroke, 45, 1375-1380.

Araujo, R. P., et al. (2004). A history of the study of solid tumour growth: The contribution of mathematical modelling. B. Math. Biol., 66, 1039-1091.

Aries, M. J., Czosnyka, M., Budohoski, K. P., Steiner, L. A., Lavinio, A., Kolias, A. G., ... & Smielewski, P. (2012). Continuous determination of optimal cerebral perfusion pressure in traumatic brain injury. Critical care medicine, 40(8), 2456-2463.

Armstrong, A. W., & Golan, D. E. (2011). Pharmacology of hemostasis and thrombosis. Principles of Pharmacology: The Pathophysiologic Basis of Drug Therapy. 3rd ed. Philadelphia: Lippincott Williams & Wilkins, 372-400.

Armulik, A., Genové, G., Mäe, M., Nisancioglu, M. H., Wallgard, E., Niaudet, C., et al. (2010).

Pericytes regulate the blood-brain barrier. Nature 468, 557–561.

Asil, T., Uzunca, I., Utku, U., & Berberoglu, U. (2003). Monitoring of increased intracranial pressure resulting from cerebral edema with transcranial Doppler sonography in patients with middle cerebral artery infarction. Journal of ultrasound in medicine, 22(10), 1049-1053.

Ayata, C., & Ropper, A. H. (2002). Ischaemic brain oedema. Journal of Clinical Neuroscience, 9(2), 113-124.

Bai, M. (1993). Multiporosity/multipermeability approach to the simulation of naturally fractured reservoirs. Water Resources Research, 29(6), 1621-1633.

Barker, S. J. (1998). Blood volume measurement: the next intraoperative monitor?. The Journal of the American Society of Anesthesiologists, 89(6), 1310-1312.

Bays, H., Abate, N., & Chandalia, M. (2005). Adiposopathy: sick fat causes high blood sugar, high blood pressure and dyslipidemia.

Bell, A. H., Miller, S. L., Castillo-Melendez, M., & Malhotra, A. (2020). The neurovascular unit: Effects of brain insults during the perinatal period. Frontiers in neuroscience, 13, 1452.

Bereczki, D., et al. (2000). Cochrane report: A systematic review of mannitol therapy for acute ischemic stroke and cerebral parenchymal hemorrhage. Stroke, 31, 2719-2722.

Biestro, A., Alberti, R., Galli, R., Cancela, M., Soca, A., Panzardo, H., & Borovich, B. (1997). Osmotherapy for increased intracranial pressure: comparison between mannitol and glycerol. Acta Neurochirurgica, 139(8), 725-733.

Bing, Y., Garcia-Gonzalez, D., Voets, N., & Jérusalem, A. (2020). Medical imaging based in silico head model for ischaemic stroke simulation. Journal of the mechanical behavior of biomedical materials, 101, 103442.

Biot, M. A. (1956). Theory of propagation of elastic waves in a fluid-saturated porous solid. II. Higher frequency range. The Journal of the acoustical Society of america, 28(2), 179-191.

Biot, M. A. (1962). Generalized theory of acoustic propagation in porous dissipative media. The Journal of the Acoustical Society of America, 34(9A), 1254-1264.

Biot, M. A. (1962). Mechanics of deformation and acoustic propagation in porous media. Journal of applied physics, 33(4), 1482-1498.

Bishop, C. C., Powell, S., Rutt, D., & Browse, N. L. (1986). Transcranial Doppler measurement of

middle cerebral artery blood flow velocity: a validation study. Stroke, 17(5), 913-915.

Boot, E., Ekker, M. S., Putaala, J., Kittner, S., De Leeuw, F. E., & Tuladhar, A. M. (2020). Ischaemic stroke in young adults: a global perspective. Journal of Neurology, Neurosurgery & Psychiatry, 91(4), 411-417.

Bozzao, L., Angeloni, U., Bastianello, S., Fantozzi, L. M., Pierallini, A., & Fieschi, C. (1991). Early angiographic and CT findings in patients with hemorrhagic infarction in the distribution of the middle cerebral artery. American journal of neuroradiology, 12(6), 1115-1121.

Brinkhues, S., Klawonn, A., Rheinbach, O., & Schröder, J. (2013). Augmented Lagrange methods for quasi-incompressible materials—Applications to soft biological tissue. International journal for numerical methods in biomedical engineering, 29(3), 332-350.

Brown, L. S., Foster, C. G., Courtney, J. M., King, N. E., Howells, D. W., & Sutherland, B. A. (2019). Pericytes and neurovascular function in the healthy and diseased brain. Frontiers in cellular neuroscience, 13, 282.

Brown, M. S., & Goldstein, J. L. (1984). How LDL receptors influence cholesterol and atherosclerosis. Scientific American, 251(5), 58-69.

Budday, S., Ovaert, T. C., Holzapfel, G. A., Steinmann, P., & Kuhl, E. (2020). Fifty shades of brain: a review on the mechanical testing and modeling of brain tissue. Archives of Computational Methods in Engineering, 27(4), 1187-1230.

Budday, S., Sommer, G., Birkl, C., Langkammer, C., Haybaeck, J., Kohnert, J., ... & Holzapfel, G. A. (2017). Mechanical characterization of human brain tissue. Acta biomaterialia, 48, 319-340.

Campbell, P. J. Mitchell, T. J. Kleinig, H. M. Dewey, L. Churilov, N. Yassi, B. Yan, R. J.Dowling, M. W. Parsons, T. J. Oxley, T. Y Wu, et al. Endovascular therapy for ischemic stroke withperfusion-imaging selection. New England Journal of Medicine, 372(11):1009–1018, 2015.

Cardim, D., Robba, C., Schmidt, B., Donnelly, J., Schmidt, E. A., Bohdanowicz, M., ... & Czosnyka, M. (2021). Midline shift in patients with closed traumatic brain injury may be driven by cerebral perfusion pressure not intracranial pressure.

Carney, N., Totten, A. M., O'Reilly, C., Ullman, J. S., Hawryluk, G. W., Bell, M. J., ... & Ghajar, J. (2017). Guidelines for the management of severe traumatic brain injury. Neurosurgery, 80(1), 6-15.

Cassot, F., Lauwers, F., Fouard, C., Prohaska, S., & Lauwers-Cances, V. (2006). A novel three-

dimensional computer-assisted method for a quantitative study of microvascular networks of the human cerebral cortex. Microcirculation, 13(1), 1-18.

Chai, X., van Herk, M., Hulshof, M. C., & Bel, A. (2012). A voxel-based finite element model for the prediction of bladder deformation. Medical physics, 39(1), 55-65.

Chen, X., Józsa, T. I., & Payne, S. J. (2022). Computational modelling of cerebral oedema and osmotherapy following ischaemic stroke. Computers in Biology and Medicine, 151, 106226.

Chen, X., Wang, J., van Kranendonk, K. R., Józsa, T. I., El-Bouri, W. K., Kappelhof, M., ... & Payne, S. J. (2023). Mathematical modelling of haemorrhagic transformation in the human brain. Applied Mathematical Modelling, 121, 96-110.

Chen, X., Józsa, T. I., Cardim, D., Robba, C., Czosnyka, M., & Payne, S. J. (2024). Modelling midline shift and ventricle collapse in cerebral oedema following acute ischaemic stroke. PLOS Computational Biology, 20(5), e1012145.

Chen-Mei, Shaw, Alvord, E. C., & Berry, R. G. (1959). Swelling of the brain following ischemic infarction with arterial occlusion. AMA Archives of Neurology, 1(2), 161-177.

Chueh, J. Y., Kang, D. H., Kim, B. M., & Gounis, M. J. (2020). Role of balloon guide catheter in modern endovascular thrombectomy. Journal of Korean Neurosurgical Society, 63(1), 14.

Çinar, Y., Şenyol, A. M., & Duman, K. (2001). Blood viscosity and blood pressure: role of temperature and hyperglycemia. American journal of hypertension, 14(5), 433-438.

Cushing, H. (1905). The establishment of cerebral hernia as a decompressive measure for inaccessible brain tumors: with the description of intermuscular methods of making the bone defect in temporal and occipital regions. Surg. Gynecol. Obstet., 1, 297-314.

Czosnyka, M., Balestreri, M., Steiner, L., Smielewski, P., Hutchinson, P. J., Matta, B., & Pickard, J. D. (2005). Age, intracranial pressure, autoregulation, and outcome after brain trauma. Journal of neurosurgery, 102(3), 450-454.

del Zoppo, G. J., et al. (2003). Cerebral microvessel responses to focal ischemia. J. Cereb. Blood Flow Metab., 23, 879-894.

Dice, L. R. (1945). Measures of the amount of ecologic association between species. Ecology, 26(3), 297-302.

Donkin, J. J., & Vink, R. (2010). Mechanisms of cerebral edema in traumatic brain injury: therapeutic developments. Current Opinion in Neurology, 23(3), 293-299.

Donnan, F. G. (1924). The theory of membrane equilibria. Chemical reviews, 1(1), 73-90.

Donnan, G. A., Davis, S. M., Chambers, B. R., Gates, P. C., Hankey, G. J., McNeil, J. J., ... & Tuck, R. R. (1996). Streptokinase for acute ischemic stroke with relationship to time of administration. Jama, 276(12), 961-966.

Drake, J. M., Mostachfi, O., Tenti, G., & Sivaloganathan, S. (1996). Realistic simple mathematical model of brain biomechanics for computer simulation of hydrocephalus and other brain abnormalities. Can. J. Neurol. Sci, 23, S5.

Drzewiecki, G., Field, S., Moubarak, I., & Li, J. K. J. (1997). Vessel growth and collapsible pressure-area relationship. American Journal of Physiology-Heart and Circulatory Physiology, 273(4), H2030-H2043.

Duvernoy, H. M., Delon, S. L. V. J., & Vannson, J. L. (1981). Cortical blood vessels of the human brain. Brain research bulletin, 7(5), 519-579.

Edmund, J. M., Kjer, H. M., Van Leemput, K., Hansen, R. H., Andersen, J. A., & Andreasen, D. (2014). A voxel-based investigation for MRI-only radiotherapy of the brain using ultra short echo times. Physics in Medicine & Biology, 59(23), 7501.

El-Bouri, W. K., & Payne, S. J. (2015). Multi-scale homogenization of blood flow in 3-dimensional human cerebral microvascular networks. Journal of Theoretical Biology, 380, 40-47.

El-Bouri, W. K., & Payne, S. J. (2016). A statistical model of the penetrating arterioles and venules in the human cerebral cortex. Microcirculation, 23(7), 580-590.

El-Bouri, W. K., & Payne, S. J. (2018). Investigating the effects of a penetrating vessel occlusion with a multi-scale microvasculature model of the human cerebral cortex. NeuroImage, 172, 94-106.

Elkin, B. S., Ilankovan, A., & Morrison III, B. (2010). Age-dependent regional mechanical properties of the rat hippocampus and cortex.

Engl, E., & Attwell, D. (2015). Non-signalling energy use in the brain. The Journal of physiology, 593(16), 3417-3429.

Fallenstein, G. T., Hulce, V. D., & Melvin, J. W. (1969). Dynamic mechanical properties of human brain tissue. Journal of biomechanics, 2(3), 217-226.

Farrall, A. J., & Wardlaw, J. M. (2009). Blood–brain barrier: ageing and microvascular disease–systematic review and meta-analysis. Neurobiology of aging, 30(3), 337-352.

Fiorelli, M., Bastianello, S., von Kummer, R., del Zoppo, G. J., Larrue, V., Lesaffre, E., ... & Bozzao, L. (1999). Hemorrhagic transformation within 36 hours of a cerebral infarct: relationships with early clinical deterioration and 3-month outcome in the European Cooperative Acute Stroke Study I (ECASS I) cohort. Stroke, 30(11), 2280-2284.

Fletcher, T. L., Wirthl, B., Kolias, A. G., Adams, H., Hutchinson, P. J., & Sutcliffe, M. P. (2016). Modelling of brain deformation after decompressive craniectomy. Annals of biomedical engineering, 44(12), 3495-3509.

Fodstad, H., et al. (1984). Effect of cranioplasty on cerebrospinal fluid hydrodynamics in patients with the syndrome of the trephined. Acta Neurochir., 70, 21-30.

Fotheringham, A. P., Davies, C. A., & Davies, I. (2000). Oedema and glial cell involvement in the aged mouse brain after permanent focal ischaemia. Neuropathology and applied neurobiology, 26(5), 412-423.

Fraser, P. A., Dallas, A. D., & Davies, S. (1990). Measurement of filtration coefficient in single cerebral microvessels of the frog. The Journal of physiology, 423(1), 343-361.

Fuchs, F. D., & Whelton, P. K. (2020). High blood pressure and cardiovascular disease. Hypertension, 75(2), 285-292.

Gaser, C. (2009). Partial volume segmentation with adaptive maximum a posteriori (MAP) approach. NeuroImage, (47), S121.

Gliem, M., Mausberg, A. K., Lee, J. I., Simiantonakis, I., van Rooijen, N., Hartung, H. P., & Jander, S. (2012). Macrophages prevent hemorrhagic infarct transformation in murine stroke models. Annals of neurology, 71(6), 743-752.

Golubev, A., Kovtanyuk, A., & Lampe, R. (2022). Modeling of cerebral blood flow autoregulation using mathematical control theory. Mathematics, 10(12), 2060.

Goswami, S., Li, D. S., Rego, B. V., Latorre, M., Humphrey, J. D., & Karniadakis, G. E. (2022). Neural operator learning of heterogeneous mechanobiological insults contributing to aortic aneurysms. Journal of the Royal Society Interface, 19(193), 20220410.

Gottschalk, A., Scafidi, S., & Toung, T. J. (2021). Brain water as a function of age and weight in normal rats. PloS one, 16(9), e0249384.

Gracien, R. M., Nürnberger, L., Hok, P., Hof, S. M., Reitz, S. C., Rüb, U., ... & Baudrexel, S. (2017). Evaluation of brain ageing: a quantitative longitudinal MRI study over 7 years. European

radiology, 27, 1568-1576.

Grände, P. O., & Romner, B. (2012). Osmotherapy in brain edema: a questionable therapy. Journal of Neurosurgical Anesthesiology, 24(4), 407-412.

Greenwood, J. (1991). Mechanisms of blood-brain barrier breakdown. Neuroradiology, 33, 95-100.

Griffis, J. C., Allendorfer, J. B., & Szaflarski, J. P. (2016). Voxel-based Gaussian naïve Bayes classification of ischemic stroke lesions in individual T1-weighted MRI scans. Journal of neuroscience methods, 257, 97-108.

Gu, J., Huang, H., Huang, Y., Sun, H., & Xu, H. (2019). Hypertonic saline or mannitol for treating elevated intracranial pressure in traumatic brain injury: a meta-analysis of randomized controlled trials. Neurosurgical Review, 42(2), 499-509.

Gu, Y., Zhou, C., Piao, Z., Yuan, H., Jiang, H., Wei, H., ... & Ji, X. (2022). Cerebral edema after ischemic stroke: Pathophysiology and underlying mechanisms. Frontiers in neuroscience, 16, 988283.

Guo, L., Vardakis, J. C., Lassila, T., Mitolo, M., Ravikumar, N., Chou, D., ... & Ventikos, Y. (2018). Subject-specific multi-poroelastic model for exploring the risk factors associated with the early stages of Alzheimer's disease. Interface focus, 8(1), 20170019.

Guo, H., & Spilker, R. L. (2014). An augmented Lagrangian finite element formulation for 3D contact of biphasic tissues. Computer methods in biomechanics and biomedical engineering, 17(11), 1206-1216.

Guo, L., Li, Z., Lyu, J., Mei, Y., Vardakis, J. C., Chen, D., ... & Ventikos, Y. (2019). On the validation of a multiple-network poroelastic model using arterial spin labeling MRI data. Frontiers in computational neuroscience, 13, 60.

Guo, L., Vardakis, J. C., Chou, D., & Ventikos, Y. (2020). A multiple-network poroelastic model for biological systems and application to subject-specific modelling of cerebral fluid transport. International Journal of Engineering Science, 147, 103204.

Hacke, W., et al. (2000). European Stroke Initiative (EUSI) recommendations for stroke management: The European Stroke Initiative Writing Committee. Eur J Neurol, 7, 607-623.

Hakamata, Y., et al. (1995). Long-term high-colloid oncotic therapy for ischemic brain edema in gerbils. Stroke, 26, 2149-2158.

Haley Jr, E. C., Brott, T. G., Sheppard, G. L., Barsan, W., Broderick, J., Marler, J. R., & Hansen, C. A.

(1993). Pilot randomized trial of tissue plasminogen activator in acute ischemic stroke. The TPABridging Study Group. Stroke, 24(7), 1000-1004.

Hamann, G. F., Liebetrau, M., Martens, H., Burggraf, D., Kloss, C. U., Bültemeier, G., ... & Pfefferkorn, T. (2002). Microvascular basal lamina injury after experimental focal cerebral ischemia and reperfusion in the rat. Journal of Cerebral Blood Flow & Metabolism, 22(5), 526-533.

Harper, S. L., & Bohlen, H. G. (1984). Microvascular adaptation in the cerebral cortex of adult spontaneously hypertensive rats. Hypertension, 6(3), 408-419.

Haruna, M., Kumon, K., Yahagi, N., Watanabe, Y., Ishida, Y., Kobayashi, N., & Aoyagi, T. (1998). Blood Volume Measurement at the Bedside Using ICG Pulse Spectrophometry. The Journal of the American Society of Anesthesiologists, 89(6), 1322-1328.

Hays, A. N., Lazaridis, C., Neyens, R., Nicholas, J., Gay, S., & Chalela, J. A. (2011). Osmotherapy: use among neurointensivists. Neurocritical Care, 14(2), 222-228.

Haywood, J. R., Shaffer, R. A., Fastenow, C., Fink, G. D., & Brody, M. J. (1981). Regional blood flow measurement with pulsed Doppler flowmeter in conscious rat. American Journal of Physiology-Heart and Circulatory Physiology, 241(2), H273-H278.

Himmelseher, S. (2007). Hypertonic saline solutions for treatment of intracranial hypertension. Current Opinion in Anesthesiology, 20(5), 414-426.

Hoenig, T., Ackerman, K. E., Beck, B. R., Bouxsein, M. L., Burr, D. B., Hollander, K., ... & Warden, S. J. (2022). Bone stress injuries. Nature Reviews Disease Primers, 8(1), 26.

Hoff, R. G., van Dijk, G. W., Algra, A., Kalkman, C. J., & Rinkel, G. J. (2008). Fluid balance and blood volume measurement after aneurysmal subarachnoid hemorrhage. Neurocritical Care, 8, 391-397.

Horie, N., Morofuji, Y., Iki, Y., Sadakata, E., Kanamoto, T., Tateishi, Y., ... & Matsuo, T. (2019). Impact of basal ganglia damage after successful endovascular recanalization for acute ischemic stroke involving lenticulostriate arteries. Journal of Neurosurgery, 132(6), 1880-1888.

Hornig, C. R., Dorndorf, W., & Agnoli, A. L. (1986). Hemorrhagic cerebral infarction--a prospective study. Stroke, 17(2), 179-185.

Iijima, T., Aoyagi, T., Iwao, Y., Masuda, J., Fuse, M., Kobayashi, N., & Sankawa, H. (1997). Cardiac output and circulating blood volume analysis by pulse dye-densitometry. Journal of clinical

monitoring, 13, 81-89.

Ito, H., Kanno, I., Iida, H., Hatazawa, J., Shimosegawa, E., Tamura, H., & Okudera, T. (2001). Arterial fraction of cerebral blood volume in humans measured by positron emission tomography. Annals of nuclear medicine, 15(2), 111-116.

Jacobs, B., Beems, T., van der Vliet, T. M., Diaz-Arrastia, R. R., Borm, G. F., & Vos, P. E. (2011). Computed tomography and outcome in moderate and severe traumatic brain injury: hematoma volume and midline shift revisited. Journal of neurotrauma, 28(2), 203-215.

Jain, A. R., Jain, M., Kanthala, A. R., Damania, D., Stead, L. G., Wang, H. Z., & Jahromi, B. S. (2013). Association of CT perfusion parameters with hemorrhagic transformation in acute ischemic stroke. American Journal of Neuroradiology, 34(10), 1895-1900.

Jamal, A., Mongelli, M. T., Vidotto, M., Madekurozwa, M., Bernardini, A., Overby, D. R., ... & Dini, D. (2020). Infusion Mechanisms in Brain White Matter and Their Dependence on Microstructure: An Experimental Study of Hydraulic Permeability. IEEE Transactions on Biomedical Engineering, 68(4), 1229-1237.

Jenkins, A., Maxwell, W. L., & Graham, D. I. (1989). Experimental intracerebral haematoma in the rat: sequential light microscopical changes. Neuropathology and applied neurobiology, 15(5), 477-486.

Jin, X., Zhu, F., Mao, H., Shen, M., & Yang, K. H. (2013). A comprehensive experimental study on material properties of human brain tissue. Journal of biomechanics, 46(16), 2795-2801.

Joseph, V., et al. (2009). Syndrome of the trephined. J. Neurosurg., 111, 650-652.

Jovin, T. G., Saver, J. L., Ribo, M., Pereira, V., Furlan, A., Bonafe, A., ... & Nogueira, R. G. (2017). Diffusion-weighted imaging or computerized tomography perfusion assessment with clinical mismatch in the triage of wake up and late presenting strokes undergoing neurointervention with Trevo (DAWN) trial methods. International Journal of Stroke, 12(6), 641-652.

Józsa, T. I., Padmos, R. M., Samuels, N., El-Bouri, W. K., Hoekstra, A. G., & Payne, S. J. (2021a). A porous circulation model of the human brain for in silico clinical trials in ischaemic stroke. Interface Focus, 11(1), 20190127.

Józsa, T. I., Padmos, R. M., El-Bouri, W. K., Hoekstra, A. G., & Payne, S. J. (2021b). On the sensitivity analysis of porous finite element models for cerebral perfusion estimation. Annals of Biomedical Engineering, 49(12), 3647-3665.

Józsa, T. I., Petr, J., Barkhof, F., Payne, S. J., & Mutsaerts, H. J. (2022). MRI-based computational model generation for cerebral perfusion simulations in health and ischaemic stroke. bioRxiv.

Józsa, T. I., Petr, J., Payne, S. J., & Mutsaerts, H. J. M. M. (2023). MRI-based parameter inference for cerebral perfusion modelling in health and ischaemic stroke. Computers in Biology and Medicine, 107543.

Ju, G., Cai, M., Li, J., & Tian, J. (2020). Parameter-robust multiphysics algorithms for Biot model with application in brain edema simulation. Mathematics and computers in simulation, 177, 385-403.

Karniadakis, G. E., Kevrekidis, I. G., Lu, L., Perdikaris, P., Wang, S., & Yang, L. (2021). Physics-informed machine learning. Nature Reviews Physics, 3(6), 422-440.

Katan, M., & Luft, A. (2018, April). Global burden of stroke. In Seminars in neurology (Vol. 38, No. 02, pp. 208-211). Thieme Medical Publishers.

Kidwell, C. S., & Wintermark, M. (2008). Imaging of intracranial haemorrhage. The Lancet Neurology, 7(3), 256-267.

Kimberly, W. T., Dutra, B. G., Boers, A. M., Alves, H. C., Berkhemer, O. A., Van Den Berg, L., ... & MR CLEAN Investigators. (2018). Association of reperfusion with brain edema in patients with acute ischemic stroke: a secondary analysis of the MR CLEAN trial. JAMA neurology, 75(4), 453-461.

Kimelberg, H. K. (2004). The role of hypotheses in current research, illustrated by hypotheses on the possible role of astrocytes in energy metabolism and cerebral blood flow: from Newton to now. Journal of Cerebral Blood Flow & Metabolism, 24(11), 1235-1239.

Kølsen-Petersen, J. A. (2020). Osmotherapy. In Management of Severe Traumatic Brain Injury (pp. 437-447). Springer, Cham.

Konduri, P. R., Marquering, H. A., Van Bavel, E. E., Hoekstra, A., Majoie, C. B., & Insist Investigators. (2020). In-silico trials for treatment of acute ischemic stroke. Frontiers in Neurology, 11, 1062.

Kristiansson, H., Nissborg, E., Bartek Jr, J., Andresen, M., Reinstrup, P., & Romner, B. (2013). Measuring elevated intracranial pressure through noninvasive methods: a review of the literature. Journal of neurosurgical anesthesiology, 25(4), 372-385.

Krueger, M., et al. (2010). CNS Pericytes: Concepts, misconceptions, and a way out. Glia, 58, 1-10. Kurland, D. B., Khaladj-Ghom, A., Stokum, J. A., Carusillo, B., Karimy, J. K., Gerzanich, V., ... &

Lambride, C., Christodoulou, N., Michail, A., Vavourakis, V., & Stylianopoulos, T. (2020). Decompressive craniectomy of post-traumatic brain injury: An in-silico modelling approach for intracranial hypertension management. Scientific reports, 10(1), 1-11.

Lang, G. E. (2014). Mechanics of swelling and damage in brain tissue: a theoretical approach (Doctoral dissertation, University of Oxford).

Lang, G. E., Vella, D., Waters, S. L., & Goriely, A. (2017). Mathematical modelling of blood–brain barrier failure and oedema. Mathematical medicine and biology: a journal of the IMA, 34(3), 391-414.

Larive, L. L., Rhoney, D. H., Parker, D., Coplin, W. M., & Carhuapoma, R. (2004). Introducing hypertonic saline for cerebral edema. Neurocritical Care, 1(4), 435-440.

Laursen, T. A., & Maker, B. N. (1995). An augmented Lagrangian quasi-Newton solver for constrained nonlinear finite element applications. International journal for numerical methods in engineering, 38(21), 3571-3590.

Lauwers, F., Cassot, F., Lauwers-Cances, V., Puwanarajah, P., & Duvernoy, H. (2008). Morphometry of the human cerebral cortex microcirculation: general characteristics and space-related profiles. Neuroimage, 39(3), 936-948.

Le Roux, P. (2016). Intracranial pressure monitoring and management. Translational research in traumatic brain injury.

LeCouffe, N. E., Kappelhof, M., Treurniet, K. M., Rinkel, L. A., Bruggeman, A. E., Berkhemer, O. A., ... & Roos, Y. B. (2021). A randomized trial of intravenous alteplase before endovascular treatment for stroke. New England journal of medicine, 385(20), 1833-1844.

Lee, G. Y., & Lim, C. T. (2007). Biomechanics approaches to studying human diseases. Trends in biotechnology, 25(3), 111-118.

Lee, M. J., Cha, J., Choi, H. A., Woo, S. Y., Kim, S., Wang, S. J., & Chung, C. S. (2017). Blood–brain barrier breakdown in reversible cerebral vasoconstriction syndrome: implications for pathophysiology and diagnosis. Annals of Neurology, 81(3), 454-466.

Leinonen, V., Vanninen, R., & Rauramaa, T. (2018). Raised intracranial pressure and brain edema. Handbook of Clinical Neurology, 145, 25-37.Osmotherapy for Elevated Intracranial Pressure

Levick, J. R., et al. (2010). Microvascular fluid exchange and the revised Starling principle. Cardiovasc.

Li, G., et al. (2010). A model for the blood-brain barrier permeability to water and small solutes. J.

Biomech., 43, 2133-2140

Li, X. G., von Holst, H., Ho, J., & Kleiven, S. (2009). 3-D finite element modeling of brain edema: Initial studies on intracranial pressure using comsol multiphysics. In Excerpt from the Proceedings of the COMSOL Conference.

Li, X., von Holst, H., & Kleiven, S. (2011). Influence of gravity for optimal head positions in the treatment of head injury patients. Acta neurochirurgica, 153(10), 2057-2064.

Li, X., von Holst, H., & Kleiven, S. (2013). Influences of brain tissue poroelastic constants on intracranial pressure (ICP) during constant-rate infusion. Computer methods in biomechanics and biomedical engineering, 16(12), 1330-1343.

Li, Z., Kovachki, N., Azizzadenesheli, K., Liu, B., Bhattacharya, K., Stuart, A., & Anandkumar, A. (2020). Fourier neural operator for parametric partial differential equations. arXiv preprint arXiv:2010.08895.

Liang, D., Bhatta, S., Gerzanich, V., and Simard, J. M. (2007). Cytotoxic edema: mechanisms of pathological cell swelling. Neurosurg. Focus 22:E2. doi: 10.3171/foc.2007.22.5.3

Liao, C. C., Chen, Y. F., & Xiao, F. (2018). Brain midline shift measurement and its automation: a review of techniques and algorithms. International journal of biomedical imaging, 2018.

Libby, P. (2002). Atherosclerosis: the new view. Scientific American, 286(5), 46-55.

Liew, S. L., Anglin, J. M., Banks, N. W., Sondag, M., Ito, K. L., Kim, H., ... & Stroud, A. (2018). A large, open source dataset of stroke anatomical brain images and manual lesion segmentations. Scientific Data, 5(1), 1-11.

Lin, F., Xia, Y., Song, S., Ravikumar, N., & Frangi, A. F. (2023). High-throughput 3dra segmentation of brain vasculature and aneurysms using deep learning. Computer Methods and Programs in Biomedicine, 230, 107355.

Lindley, R. I., Wardlaw, J. M., Sandercock, P. A., Rimdusid, P., Lewis, S. C., Signorini, D. F., & Ricci, S. (2004). Frequency and risk factors for spontaneous hemorrhagic transformation of cerebral infarction. Journal of Stroke and Cerebrovascular Diseases, 13(6), 235-246.

Lipkova, J., Chen, T. Y., Lu, M. Y., Chen, R. J., Shady, M., Williams, M., ... & Mahmood, F. (2022). Deep learning-enabled assessment of cardiac allograft rejection from endomyocardial biopsies. Nature medicine, 28(3), 575-582.

Logg, A., & Wells, G. N. (2010). DOLFIN: Automated finite element computing. ACM Transactions

on Mathematical Software (TOMS), 37(2), 1-28.

Logg, A., Mardal, K. A., & Wells, G. (Eds.). (2012). Automated solution of differential equations by the finite element method: The FEniCS book (Vol. 84). Springer Science & Business Media.

Lucas, C. (2013). An anatomical model of the cerebral vasculature and blood flow. (D. Phil.), Oxford Univ., Oxford.

Lüders, E., Steinmetz, H., & Jäncke, L. (2002). Brain size and grey matter volume in the healthy human brain. Neuroreport, 13(17), 2371-2374.

Mangat, H. S. (2018). Hypertonic saline infusion for treating intracranial hypertension after severe traumatic brain injury. Critical Care, 22(1), 1-3.

Mann, J. D., Butler, A. B., Rosenthal, J. E., Maffeo, C. J., Johnson, R. N., & Bass, N. H. (1978). Regulation of intracranial pressure in rat, dog, and man. Annals of Neurology: Official Journal of the American Neurological Association and the Child Neurology Society, 3(2), 156-165.

Marmarou, A., Fatouros, P. P., Barzó, P., Portella, G., Yoshihara, M., Tsuji, O., ... & Young, H. F. (2000). Contribution of edema and cerebral blood volume to traumatic brain swelling in head-injured patients. Journal of neurosurgery, 93(2), 183-193.

Marsh, E. B., Llinas, R. H., Hillis, A. E., & Gottesman, R. F. (2013). Hemorrhagic transformation in patients with acute ischaemic stroke and an indication for anticoagulation. European Journal of Neurology, 20(6), 962-967.

Martin, W. W., Powers, W. J., & Raichle, M. E. (1987). Cerebral blood volume measured with inhaled C15O and positron emission tomography. Journal of Cerebral Blood Flow & Metabolism, 7(4), 421-426.

May, C., Kaye, J. A., Atack, J. R., Schapiro, M. B., Friedland, R. P., & Rapoport, S. I. (1990). Cerebrospinal fluid production is reduced in healthy aging. Neurology, 40(3_part_1), 500-500.

Miller, M. T., Pasquale, M., Kurek, S., White, J., Martin, P., Bannon, K., ... & Li, M. (2004). Initial head computed tomographic scan characteristics have a linear relationship with initial intracranial pressure after trauma. Journal of Trauma and Acute Care Surgery, 56(5), 967-973.

Miller, C., Padmos, R. M., van der Kolk, M., Józsa, T. I., Samuels, N., Xue, Y., ... & Hoekstra, A. G. (2021). In silico trials for treatment of acute ischemic stroke: Design and implementation. Computers in Biology and Medicine, 137, 104802.

Mitsis, G. D., Zhang, R., Levine, B. D., & Marmarelis, V. Z. (2002). Modeling of nonlinear

physiological systems with fast and slow dynamics. II. Application to cerebral autoregulation. Annals of biomedical engineering, 30, 555-565.

Mokhtarudin, M. M., & Payne, S. J. (2015). Mathematical model of the effect of ischemia–reperfusion on brain capillary collapse and tissue swelling. Mathematical Biosciences, 263, 111-120.

Mokhtarudin, M. J. M. (2016). Mathematical modelling of cerebral ischaemia-reperfusion injury (Doctoral dissertation, University of Oxford).

Mokhtarudin, M. J. M., & Payne, S. J. (2017). The study of the function of AQP4 in cerebral ischaemia–reperfusion injury using poroelastic theory. International journal for numerical methods in biomedical engineering, 33(1), e02784.

Mokri, B. (2001). The Monro–Kellie hypothesis: applications in CSF volume depletion. Neurology, 56(12), 1746-1748.

Montagne, A., Barnes, S. R., Sweeney, M. D., Halliday, M. R., Sagare, A. P., Zhao, Z., ... & Zlokovic, B. V. (2015). Blood-brain barrier breakdown in the aging human hippocampus. Neuron, 85(2), 296-302.

Motuel, J., Biette, I., Srairi, M., Mrozek, S., Kurrek, M. M., Chaynes, P., ... & Geeraerts, T. (2014). Assessment of brain midline shift using sonography in neurosurgical ICU patients. Critical Care, 18, 1-8.

Mushtaq, M., Abdul Mateen, M., & Kim, U. H. (2019). Hyperglycemia associated blood viscosity can be a nexus stimuli. Clinical hemorheology and microcirculation, 71(1), 103-112.

Mutsaerts, H. J. M. M., Van Dalen, J. W., Heijtel, D. F. R., Groot, P. F. C., Majoie, C. B. L. M., Petersen, E. T., ... & Nederveen, A. J. (2015). Cerebral perfusion measurements in elderly with hypertension using arterial spin labeling. PloS one, 10(8), e0133717.

Nag, D. S., Sahu, S., Swain, A., & Kant, S. (2019). Intracranial pressure monitoring: Gold standard and recent innovations. World journal of clinical cases, 7(13), 1535.

Nag, S. (2003). Pathophysiology of blood-brain barrier breakdown. The Blood-Brain Barrier, 97-119.

Nagashima, T. A., Tada, Y., Hamano, S., Skakakura, M., Masaoka, K., Tamaki, N., & Matsumoto, S. (1990). The finite element analysis of brain oedema associated with intracranial meningiomas. In Brain Edema VIII: Proceedings of the Eighth International Symposium, Bern, June 17–20, 1990 (pp. 155-157). Springer Vienna.

Nah, H. W., Kwon, S. U., Kang, D. W., Ahn, J. S., Kwun, B. D., & Kim, J. S. (2012). Moyamoya

disease-related versus primary intracerebral hemorrhage: location and outcomes are different. Stroke, 43(7), 1947-1950.

Nau, R. (2000). Osmotherapy for elevated intracranial pressure. Clinical Pharmacokinetics, 38(1), 23-40.

Neugebauer, H., & Jüttler, E. (2014). Hemicraniectomy for malignant middle cerebral artery infarction: current status and future directions. International Journal of Stroke, 9(4), 460-467.

Okell, T. W., Chappell, M. A., Kelly, M. E., & Jezzard, P. (2013). Cerebral blood flow quantification using vessel-encoded arterial spin labeling. Journal of Cerebral Blood Flow & Metabolism, 33(11), 1716-1724.

Olufsen, M. S., Nadim, A., & Lipsitz, L. A. (2002). Dynamics of cerebral blood flow regulation explained using a lumped parameter model. American Journal of Physiology-Regulatory, Integrative and Comparative Physiology, 282(2), R611-R622.

Otani, T., Nishimura, N., Yamashita, H., Ii, S., Yamada, S., Watanabe, Y., ... & Wada, S. (2023). Computational modeling of multiscale collateral blood supply in a whole-brain-scale arterial network. PLOS Computational Biology, 19(9), e1011452.

Ouyang, M. W., McDonagh, D. L., Phillips-Bute, B., James, M. L., Friedman, A. H., & Gan, T. J. (2013). Does midline shift predict postoperative nausea in brain tumor patients undergoing awake craniotomy? A retrospective analysis. Current medical research and opinion, 29(9), 1033-1038.

Paczynski, R. P. (1997). Osmotherapy: basic concepts and controversies. Critical Care Clinics, 13(1), 105-129.

Padmos, R. M., Józsa, T. I., El-Bouri, W. K., Konduri, P. R., Payne, S. J., & Hoekstra, A. G. (2021). Coupling one-dimensional arterial blood flow to three-dimensional tissue perfusion models for in silico trials of acute ischaemic stroke. Interface focus, 11(1), 20190125.

Pallesen, L. P., Barlinn, K., & Puetz, V. (2019). Role of decompressive craniectomy in ischemic stroke. Frontiers in neurology, 9, 1119.

Papademetris, X., Sinusas, A. J., Dione, D. P., Constable, R. T., & Duncan, J. S. (2002). Estimation of 3-D left ventricular deformation from medical images using biomechanical models. IEEE transactions on medical imaging, 21(7), 786-800.

Papadopoulos, M. C., & Verkman, A. S. (2007). Aquaporin-4 and brain edema. Pediatric nephrology, 22(6), 778-784.

Paulson, O. B., Strandgaard, S., & Edvinsson, L. (1990). Cerebral autoregulation. Cerebrovascular and brain metabolism reviews, 2(2), 161-192.

Payne, S. J. (2006). A model of the interaction between autoregulation and neural activation in the brain.

Payne, S. (2016). Cerebral autoregulation: control of blood flow in the brain (pp. 1-125). Berlin: Springer.

Payne, S. J. (2018). Cerebral blood flow and metabolism: A quantitative approach.

Payne, S. (2023). Interstitial fluid transport in a multi-compartment model of cerebral blood flow. Journal of Mechanics, in press.

Payne, S. J., & Lucas, C. (2018). Oxygen delivery from the cerebral microvasculature to tissue is governed by a single time constant of approximately 6 seconds. Microcirculation, 25(2), e12428.

Perlmutter, L. S., & Chui, H. C. (1990). Microangiopathy, the vascular basement membrane and Alzheimer's disease: a review. Brain research bulletin, 24(5), 677-686.

Peyrounette, M., Davit, Y., Quintard, M., & Lorthois, S. (2018). Multiscale modelling of blood flow in cerebral microcirculation: Details at capillary scale control accuracy at the level of the cortex. PloS One, 13(1), e0189474.

Post, M. W. M., Visser-Meily, J. M. A., Boomkamp-Koppen, H. G. M., & Prevo, A. J. H. (2003). Assessment of oedema in stroke patients: comparison of visual inspection by therapists and volumetric assessment. Disability and Rehabilitation, 25(22), 1265-1270.

Qiu, S., Miller, M. I., Joshi, P. S., Lee, J. C., Xue, C., Ni, Y., ... & Kolachalama, V. B. (2022). Multimodal deep learning for Alzheimer's disease dementia assessment. Nature communications, 13(1), 3404.

Qureshi, A. I., & Suarez, J. I. (2000). Use of hypertonic saline solutions in treatment of cerebral edema and intracranial hypertension. Critical Care Medicine, 28(9), 3301-3313.

Raboel, P. H., Bartek, J., Andresen, M., Bellander, B. M., & Romner, B. (2012). Intracranial pressure monitoring: invasive versus non-invasive methods—a review. Critical Care Research and Practice, 2012.

Ragauskas, A., Matijosaitis, V., Zakelis, R., Petrikonis, K., Rastenyte, D., Piper, I., & Daubaris, G. (2012). Clinical assessment of noninvasive intracranial pressure absolute value measurement method. Neurology, 78(21), 1684-1691.

Rangel-Castillo, L., Gopinath, S., & Robertson, C. S. (2008). Management of intracranial hypertension. Neurologic clinics, 26(2), 521-541.

Rasmussen, M. K., Mestre, H., & Nedergaard, M. (2022). Fluid transport in the brain. Physiological reviews, 102(2), 1025-1151.

Reulen, H. J., Tsuyumu, M., Tack, A., Fenske, A. R., & Prioleau, G. R. (1978). Clearance of edema fluid into cerebrospinal fluid: A mechanism for resolution of vasogenic brain edema. Journal of neurosurgery, 48(5), 754-764.

Rippe, B., & Haraldsson, B. (1994). Transport of macromolecules across microvascular walls: the two-pore theory. Physiological reviews, 74(1), 163-219.

Robba, C., Bacigaluppi, S., Cardim, D., Donnelly, J., Bertuccio, A., & Czosnyka, M. (2016). Non-invasive assessment of intracranial pressure. Acta Neurologica Scandinavica, 134(1), 4-21.

Rosenberg JB, Shiloh AL, Savel RH, Eisen LA. Non-invasive methods of estimating intracranial pressure. Neurocritical care. 2011 Dec;15:599-608.

Sack, I., Beierbach, B., Wuerfel, J., Klatt, D., Hamhaber, U., Papazoglou, S., ... & Braun, J. (2009). The impact of aging and gender on brain viscoelasticity. Neuroimage, 46(3), 652-657.

Sapoval, N., Aghazadeh, A., Nute, M. G., Antunes, D. A., Balaji, A., Baraniuk, R., ... & Treangen, T. J. (2022). Current progress and open challenges for applying deep learning across the biosciences. Nature Communications, 13(1), 1728.

Schmidt B, Czosnyka M, Schwarze JJ, Sander D, Gerstner W, Lumenta CB, Pickard JD, Klingelhöfer J. Cerebral vasodilatation causing acute intracranial hypertension: a method for noninvasive assessment. J Cereb Blood Flow Metab. 1999 Sep;19(9):990-6.

Schwarz, S., Georgiadis, D., Aschoff, A., & Schwab, S. (2002). Effects of hypertonic (10%) saline in patients with raised intracranial pressure after stroke. Stroke, 33(1), 136-140.

Severinghaus, J. W., & Honda, Y. (1987). History of blood gas analysis. VII. Pulse oximetry. Journal of clinical monitoring, 3, 135-138.

Shakoor, N., & Moisio, K. (2004). A biomechanical approach to musculoskeletal disease. Best Practice & Research Clinical Rheumatology, 18(2), 173-186.

Siemkowicz, E. (1980). Cerebrovascular resistance in ischemia. Pflugers Arch., 388, 243-247.

Simard, J. M. (2015). Complications associated with decompressive craniectomy: a systematic review.

Neurocritical care, 23(2), 292-304.

Smith, W. S., Sung, G., Saver, J., Budzik, R., Duckwiler, G., Liebeskind, D. S., & Gobin, Y. P. (2008). Mechanical thrombectomy for acute ischemic stroke: final results of the Multi MERCI trial. Stroke, 39(4), 1205-1212.

Smith, W. S., Sung, G., Starkman, S., Saver, J. L., Kidwell, C. S., Gobin, Y. P., & Marks, M. P. (2005). Safety and efficacy of mechanical embolectomy in acute ischemic stroke: results of the MERCI trial. Stroke, 36(7), 1432-1438.

Soinne, L., et al. (2014). Malignant hemispheric infarction: Diagnosis and management by hemicraniectomy. Stroke, 45, e185-e187.

Stamatovic, S. M., Keep, R. F., & Andjelkovic, A. V. (2008). Brain endothelial cell-cell junctions: how to "open" the blood brain barrier. Current neuropharmacology, 6(3), 179-192.

Starling, E. H. (1896). On the absorption of fluids from the connective tissue spaces.

Steiner, L. A., & Andrews, P. J. D. (2006). Monitoring the injured brain: ICP and CBF. BJA: British Journal of Anaesthesia, 97(1), 26-38.

Stromberg, D. D., & Fox, J. R. (1972). Pressures in the pial arterial microcirculation of the cat during changes in systemic arterial blood pressure. Circulation Research, 31(2), 229-239.

Su, S. W. (2011). Modelling blood flow and oxygen transport in the human cerebral cortex. (D. Phil.), Oxford Univ., Oxford.

Sweetman, B., Xenos, M., Zitella, L., & Linninger, A. A. (2011). Three-dimensional computational prediction of cerebrospinal fluid flow in the human brain. Computers in Biology and Medicine, 41(2), 67-75.

Tada, Y., & Nagashima, T. (1994). Modeling and simulation of brain lesions by the finite-element method. IEEE Engineering in Medicine and Biology Magazine, 13(4), 497-503.

Tamaki, K. I. N. Y. A., & Heistad, D. D. (1986). Response of cerebral arteries to sympathetic stimulation during acute hypertension. Hypertension, 8(10), 911-917.

Tan, S., Wang, D., Liu, M., Zhang, S., Wu, B., & Liu, B. (2014). Frequency and predictors of spontaneous hemorrhagic transformation in ischemic stroke and its association with prognosis. Journal of neurology, 261, 905-912.

Tatu, L., Moulin, T., Bogousslavsky, J., & Duvernoy, H. (1998). Arterial territories of the human brain:

cerebral hemispheres. Neurology, 50(6), 1699-1708.

Treurniet, K. M., LeCouffe, N. E., Kappelhof, M., Emmer, B. J., van Es, A. C., Boiten, J., ... & MR CLEAN-NO IV Investigators. (2021). MR CLEAN-NO IV: intravenous treatment followed by endovascular treatment versus direct endovascular treatment for acute ischemic stroke caused by a proximal intracranial occlusion—study protocol for a randomized clinical trial. Trials, 22, 1-15.

Tu, P. H., Liu, Z. H., Chuang, C. C., Yang, T. C., Wu, C. T., & Lee, S. T. (2012). Postoperative midline shift as secondary screening for the long-term outcomes of surgical decompression of malignant middle cerebral artery infarcts. Journal of Clinical Neuroscience, 19(5), 661-664.

Tully, B., & Ventikos, Y. (2011). Cerebral water transport using multiple-network poroelastic theory: application to normal pressure hydrocephalus. Journal of Fluid Mechanics, 667, 188-215.

Tyagi, R., Donaldson, K., Loftus, C. M., & Jallo, J. (2007). Hypertonic saline: a clinical review. Neurosurgical Review, 30(4), 277-290.

Unterberg, A. W., Stover, J., Kress, B., & Kiening, K. L (2004). Edema and brain trauma. Neuroscience, 129(4), 1019-1027.

Valadka, A. B., Gopinath, S. P., & Robertson, C. S. (2000). Midline shift after severe head injury: pathophysiologic implications. Journal of Trauma and Acute Care Surgery, 49(1), 1-10.

van der Steen, W., van der Ende, N. A., van Kranendonk, K. R., Chalos, V., van Oostenbrugge, R. J., van Zwam, W. H., ... & Roozenbeek, B. (2022). Determinants of symptomatic intracranial hemorrhage after endovascular stroke treatment: a retrospective cohort study. Stroke, 53(9), 2818-2827.

Van Kranendonk, K. R., Treurniet, K. M., van Zwam, W. H., van Oostenbrugge, R. J., Dippel, D. W., Roos, Y. B., ... & Majoie, C. B. (2020). Added prognostic value of hemorrhagic transformation quantification in patients with acute ischemic stroke. Frontiers in Neurology, 11, 582767.

Vardakis, J. C., Chou, D., Tully, B. J., Hung, C. C., Lee, T. H., Tsui, P. H., & Ventikos, Y. (2016). Investigating cerebral oedema using poroelasticity. Medical engineering & physics, 38(1), 48-57.

Vardakis, J. C., Guo, L., Peach, T. W., Lassila, T., Mitolo, M., Chou, D., ... & Ventikos, Y. (2019). Fluid–structure interaction for highly complex, statistically defined, biological media: Homogenisation and a 3D multi-compartmental poroelastic model for brain biomechanics. Journal of Fluids and Structures, 91, 102641.

Vemmos, K. N., Spengos, K., Tsivgoulis, G., Zakopoulos, N., Manios, E., Kotsis, V., ... &

Vassilopoulos, D. (2004). Factors influencing acute blood pressure values in stroke subtypes. Journal of human hypertension, 18(4), 253-259.

Verheggen, I. C., de Jong, J. J., van Boxtel, M. P., Gronenschild, E. H., Palm, W. M., Postma, A. A., ... & Backes, W. H. (2020). Increase in blood–brain barrier leakage in healthy, older adults. Geroscience, 42, 1183-1193.

Vidotto, M., Bernardini, A., Trovatelli, M., De Momi, E., & Dini, D. (2021). On the microstructural origin of brain white matter hydraulic permeability. Proceedings of the National Academy of Sciences, 118(36), e2105328118.

von Holst, H., & Li, X. (2014). Decompressive craniectomy (DC) at the non-injured side of the brain has

von Kummer, R., Broderick, J. P., Campbell, B. C., Demchuk, A., Goyal, M., Hill, M. D., ... & Hacke, W. (2015). The Heidelberg bleeding classification: classification of bleeding events after ischemic stroke and reperfusion therapy. Stroke, 46(10), 2981-2986.

Vorbrodt, A. W., Lossinsky, A. S., Wisniewski, H. M., Suzuki, R., Yamaguchi, T., Masaoka, H., & Klatzo, I. (1985). Ultrastructural observations on the transvascular route of protein removal in vasogenic brain edema. Acta neuropathologica, 66, 265-273.

Walberer, M., Blaes, F., Stolz, E., Müller, C., Schoenburg, M., Tschernatsch, M., ... & Gerriets, T. (2007). Midline-shift corresponds to the amount of brain edema early after hemispheric stroke—an MRI study in rats. Journal of neurosurgical anesthesiology, 19(2), 105-110.

Wang, X., Tsuji, K., Lee, S. R., Ning, M., Furie, K. L., Buchan, A. M., & Lo, E. H. (2004). Mechanisms of hemorrhagic transformation after tissue plasminogen activator reperfusion therapy for ischemic stroke. Stroke.

Wang, J., & Payne, S. J. (2021). Mathematical modelling of haemorrhagic transformation after ischaemic stroke. Journal of Theoretical Biology, 531, 110920.

Wang, J., Van Kranendonk, K. R., El-Bouri, W. K., Majoie, C. B., & Payne, S. J. (2022). Mathematical modelling of haemorrhagic transformation within a multiscale microvasculature network. Physiological measurement, 43(5), 055006.

Wang, C., Chen, X., Wang, L., Makihata, M., Liu, H. C., Zhou, T., & Zhao, X. (2022). Bioadhesive ultrasound for long-term continuous imaging of diverse organs. Science, 377(6605), 517-523.

Weickenmeier, J., Butler, C. A. M., Young, P. G., Goriely, A., & Kuhl, E. (2017). The mechanics of

decompressive craniectomy: Personalized simulations. Computer Methods in Applied Mechanics and Engineering, 314, 180-195.

Wells, C. E. (1978). Chronic brain disease: an overview. The American journal of psychiatry.

White, H., & Venkatesh, B. (2008). Cerebral perfusion pressure in neurotrauma: a review. Anesthesia & Analgesia, 107(3), 979-988.

Wiegers, E. J., Mulder, M. J., Jansen, I. G., Venema, E., Compagne, K. C., Berkhemer, O. A., ... & van der Lugt, A. (2020). Clinical and imaging determinants of collateral status in patients with acute ischemic stroke in MR CLEAN trial and registry. Stroke, 51(5), 1493-1502.

Wise BL & Chater N. The value of hypertonic mannitol solutionin decreasing brain mass and lowering cerebrospinal fluid pressure. Journal of Neurosurgery 1962; 19: 1038-

Wolman, M., Klatzo, I., Chui, E., Wilmes, F., Nishimoto, K., Fujiwara, K., & Spatz, M. (1981). Evaluation of the dye-protein tracers in pathophysiology of the blood-brain barrier. Acta neuropathologica, 54(1), 55-61.

Wriggers, P. (2006). Computational contact mechanics (Vol. 2, p. 25). T. A. Laursen (Ed.). Berlin: Springer.

Wu, S., Yuan, R., Wang, Y., Wei, C., Zhang, S., Yang, X., & Liu, M. (2018). Early prediction of malignant brain edema after ischemic stroke: a systematic review and meta-analysis. Stroke, 49(12), 2918-2927.

Wu, S., Zhao, W., & Ji, S. (2022). Real-time dynamic simulation for highly accurate spatiotemporal brain deformation from impact. Computer methods in applied mechanics and engineering, 394, 114913.

Yamamoto, T., Kabus, S., Von Berg, J., Lorenz, C., Chung, M. P., Hong, J. C., ... & Keall, P. J. (2012). Reproducibility of four-dimensional computed tomography-based lung ventilation imaging. Academic radiology, 19(12), 1554-1565.

Yang, Y., & Rosenberg, G. A. (2011). Blood–brain barrier breakdown in acute and chronic cerebrovascular disease. Stroke, 42(11), 3323-3328.

Yetim, E., Jacoby, J., Damestani, N. L., Lovely, A. E., Salat, D. H., & Juttukonda, M. R. (2023). Mean Arterial Pressure and Cerebral Hemodynamics Across The Lifespan: A Cross-Sectional Study From Human Connectome Project-Aging. Journal of Magnetic Resonance Imaging.

Yin, M., Zheng, X., Humphrey, J. D., & Karniadakis, G. E. (2021). Non-invasive inference of thrombus

material properties with physics-informed neural networks. Computer Methods in Applied Mechanics and Engineering, 375, 113603.

Yuan, J., Liu, L., & Hu, Q. (2013). Mathematical modeling of brain glioma growth using modified reaction–diffusion equation on brain MR images. Computers in Biology and Medicine, 43(12), 2007-2013.

Zagzoule, M., & Marc-Vergnes, J. P. (1986). A global mathematical model of the cerebral circulation in man. Journal of biomechanics, 19(12), 1015-1022.

Zhang, X., Adamson, R. H., Curry, F. R. E., & Weinbaum, S. (2006). A 1-D model to explore the effects of tissue loading and tissue concentration gradients in the revised Starling principle. American Journal of Physiology-Heart and Circulatory Physiology, 291(6), H2950-H2964.

Zhang, X., Huang, P., & Zhang, R. (2022). Evaluation and prediction of post-stroke cerebral edema based on neuroimaging. Frontiers in Neurology, 12, 763018.

Zhou, R., Guo, F., Azarpazhooh, M. R., Spence, J. D., Ukwatta, E., Ding, M., & Fenster, A. (2020). A voxel-based fully convolution network and continuous max-flow for carotid vessel-wall-volume segmentation from 3D ultrasound images. IEEE Transactions on Medical Imaging, 39(9), 2844-2855.

Ziai, W. C., Toung, T. J., & Bhardwaj, A. (2007). Hypertonic saline: first-line therapy for cerebral edema. Journal of the Neurological Sciences, 261(1-2), 157-166.

Zienkiewicz, O. C., & Shiomi, T. (1984). Dynamic behaviour of saturated porous media; the generalized Biot formulation and its numerical solution. International Journal for Numerical and Analytical Methods in Geomechanics, 8(1), 71-96.

Zienkiewicz, O. C., Chan, A. H. C., Pastor, M., Paul, D. K., & Shiomi, T. (1990). Static and dynamic behaviour of soils: a rational approach to quantitative solutions. I. Fully saturated problems. Proceedings of the Royal Society of London. A. Mathematical and Physical Sciences, 429(1877), 285-309.

Zimmerman, B. J., & Granger, D. N. (1992). Reperfusion injury. Surgical Clinics of North America, 72(1), 65-83.

Zimmermann, E. A., Busse, B., & Ritchie, R. O. (2015). The fracture mechanics of human bone: influence of disease and treatment. BoneKEy reports, 4.

Zipfel, J., Engel, J., Hockel, K., Heimberg, E., Schuhmann, M. U., & Neunhoeffer, F. (2021). Effects

of hypertonic saline on intracranial pressure and cerebral autoregulation in pediatric traumatic brain injury. Journal of Neurosurgery: Pediatrics, 28(6), 631-637.

Zornow, M. H. (1996). Hypertonic saline as a safe and efficacious treatment of intracranial hypertension.